Study on near range high resolution 3D radar imaging

PhD Dissertation

Study on Near Range High Resolution 3D Radar Imaging

（高精度3次元近距離レーダに関する研究）

Submitted to

Graduate School of Environmental Studies
Tohoku University

by

Andrey Lyulyakin

Sendai, Japan, January 20, 2018

Supervised by

Prof. Dr. Motoyuki Sato

Dissertation Committee

Prof. Motoyuki Sato
Prof. Takatoshi Ito
Prof. Qiang Chen
Prof. Naoki Honma
(Iwate University)

Abstract

Three-dimensional imaging techniques have been developed for a wide area of applications, including the applications in near field such as ground penetrating radar imaging, hidden object imaging and security control. Different types of active radar systems have been by many research institutions, developing new technologies of imaging every day. This work is motivated by investigation of 3D imaging with two types of continuous wave radars and its specificities, mainly focused on optimization technic of the antenna arrays and tracking of the radar.

In order to improve an imaging performance of a sparse array radar system, an optimization method to find a new antenna array layout was proposed. The method searches the minimum of a cost function based on a 3D point spread function of the array. A few different relations of the L-norm of the reconstructed image were compared. A $L_{0.5}$-norm maximization for the targets and a L_2-norm minimization for the artifacts showed better results compare to others. Relation of these two norms is one of the key features of the method.

Another feature is related to making the optimized solution warranted for the different positions of the targets. It is using a random target distribution for an each iteration of the optimization algorithm. Also the accumulating of the cost function, using several combination of the targets at each step of the optimization, was used. It making the optimization process keep away from been stuck in local minimum pushing it to further minimization of the cost function.

The two-dimensional sparse array system has been used for a 3D imaging of the inner structure of building walls, and in order to find the antenna array layout with higher focusing of the targets, the optimization algorithm was applied to this system. We found a solution for the simulated problem in a form of new layout with sparser middle-point distribution comparing with initial one. The new antenna array was tested at object recognition in laboratory conditions.

A second system studied in this work is the millimeter wave radar that have been used in 3D imaging due to its specificity of multichannel signal receiving. Different types of migration with this frequency modulated signal radar provide a high resolution imaging of a target, and linear and rotating scanning have been used to achieve it.

3D back projection algorithm was applied to reconstruct an image of a target and succeed in getting a precise position of it. Taking into account that the very high azimuth resolution could be achieved by synthetic aperture radar, the vertical resolution is still could be a problem. 3-channels system however performed quite good results in obtaining the high of the target position, allowed us to propose a way of tracking the radar system using rotating table. The experiment with tracking of the radar was done outside in two dimensions and in three dimensions in laboratory conditions.

The optimization algorithm was applied to the problem of antenna positioning for the MMW radar. The simulation with $L_{0.5}L_2$-norm cost function and random target distribution for 5 and 10 elements linear antenna arrays was done, however this optimization method may not be always sufficient as it have been seen from results.

Keywords: Near range, synthetic aperture radar (SAR), continuous wave radar (CW radar), 3D imaging, millimeter wave radar (MMW radar), sparse array optimization, optimization algorithm, cost function, radar tracking, rotating radar, environmental monitoring.

Table of Contents

List of Figures

Chapter 1 Introduction

1.1 Research background

1.1.1 Near range radar applications

In order to get information about objects inner structure, to detect and recognize shapes of the objects a high resolution radar imaging have been used. However, the technology, based on ultra-wideband (UWB), is limited by microwave propagation effects, wave scattering, and power loss. Operating of the radar in the near-field could overpass the problem of the received signals been weak and noisy. Such UWB imaging systems are used for various applications such as imaging through obstacles, security and medical area [1]–[5]. Active radar systems have been used for it, covering a large area of operating frequency ranges, from less than 100 MHz up to the 350 GHz, with the frequency range customized for each application.

In these systems, down-range and cross-range resolutions are determined by the frequency bandwidth and size of the antenna arrays. In the classical two-dimensional designs, element spacing is chosen as at most half of the center wavelength to eliminate undesired grating lobes. As a result, in applications demanding high-resolution, classical (non-sparse) planar arrays require high hardware complexity and cost. To reduce this complexity, a sparse array systems have been used due to it.

Depending on the field of application, the spatial sampling can be realized with mechanical scanning techniques or electronic sampling by switching between spatially distributed transmit and receive antennas. Using a synthetic aperture radar (SAR) processing or migration is an essential basis in the near range radar imaging, which can be used in ground penetrating radar (GPR) and ground-based synthetic aperture radar (GB-SAR).

In my study I came across several problems on the way to get the high resolution image with Continues Wave (CW) radar. Results of the solving of these problems are introduced in the dissertation.

1.1.2 SAR data processing

A Synthetic Aperture Radar works similar of a phased array, but contrary of a large number of the parallel antenna elements of a phased array, SAR uses one antenna in time-multiplex. The

different geometric positions of the antenna elements are result of the moving platform.

As a target (like a plane) first enters the radar beam, the reflected signal from each transmitted pulse begin to be recorded. As the platform continues to move forward, all signals from the target for each pulse are recorded during the entire time that the target is within the beam. The point at which the target leaves the view of the radar beam some time later, determines the length of the simulated or synthesized antenna.

Most of the SAR image reconstruction use Fourier transformation based imaging approach. The radiation pattern of an array antenna is well understood that the wider array size and denser array spacing gives the narrower beam width, thus we can obtain better azimuth resolution in real aperture radar imaging. In SAR, using radar signal acquired moving along a survey line, and the narrow beam, or high resolution image is equivalently given by a simple image reconstruction algorithm

1.2 Sparse array optimization problem

To reduce radar cost and complexity, sparse linear or 2D arrays can be used. These antenna arrays have an inter spacing between radiating elements larger than in the dense array. For all the advantages, sparse arrays suffer from high sidelobes compared to dense arrays. The sidelobe distribution and level depend on the element placement and possibly element weighting.

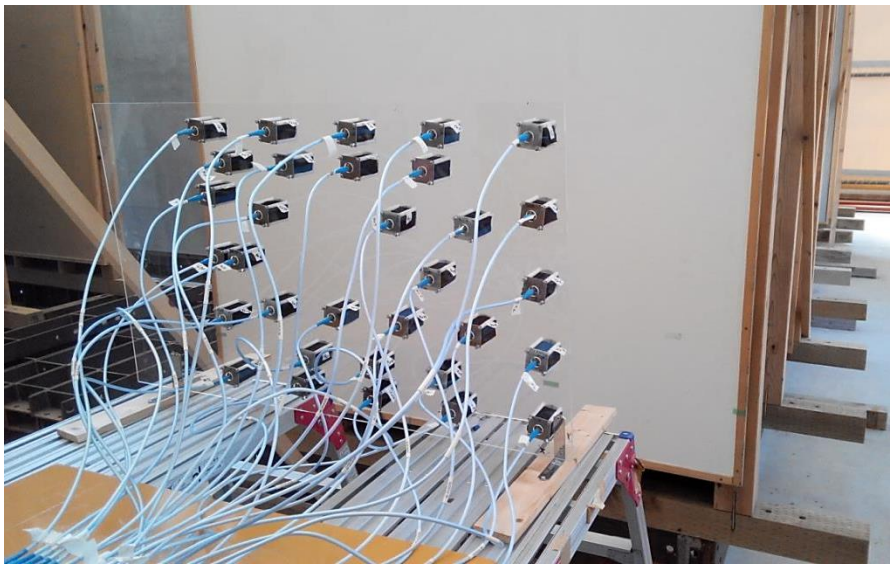

Figure 1 The sparse array at the near range survey of the inner structure of the wall.

The problem of optimization is a well discussed topic that has been presented in papers by methods that applying different optimization algorithms on the weight function to find a solution with better performance [8] - [12]. The most common optimization criterion is a minimization of

the peak sidelobe or the integrated sidelobe energy overall. In this thesis we use the cost function built in a form of relation of the *L*-norms of reconstructed image in a way to uniformly image the targets in all imaging area. By minimizing it we equalize the level of the imaged targets and decrease the artifacts level.

1.3 Objects imaging with millimeter waves radar

For both active and passive radar the high resolution imaging strongly depends on broadband imaging sensors. The range resolution is proportional to bandwidth and does not depend on the actual frequency domain. The millimeter wave (MMW) region, from 30GHz to 300GHz provides a fairly well condition for short range, high resolution and ultrawideband imaging applications.

Considering the available technology, the selection of the frequency domain can be done according to the desired propagation characteristics of the electromagnetic waves. For example, the spectroscopic properties of the THz region (from 300GHz up to 10THz) could have a major advantage in security applications dealing with the imaging of concealed objects, such as explosives and metallic or ceramic materials. However, using the THz sensors yet is not suitable for environments outside the laboratory. On the other hand, using the MMW sensors is not a problem, what makes the MMW region a good candidate for developing the technologies in many applications of environmental studies.

1.4 Contents of thesis

This research work aims to develop technologies for the near field 3D imaging in different applications. Two types of monitoring systems are discussed. One system is the Step Frequency Continuous Wave Radar (SFCW Radar) with a 2D sparse array antenna used in inspection of the inner wall structure. And second one is the FMCW radar used as a position tracker on the moving objects.

Chapter 2 is dedicated to the problem of optimization of the antenna array. Starting from the benefits of using a sparse array over the dense array, it describes the way of antenna array optimization. In order to improve an imaging performance of a sparse array radar system, an optimization method to find a new antenna array layout was proposed. A few different relations of the *L*-norm of the reconstructed image were compared. It has been described how choice of the norm influence on the optimization results. The random target distribution for an each iteration of the optimization algorithm has also been used. The accumulating of the cost function,

using several combination of the targets at each step of the optimization, making the optimization process keep away from been stuck in local minimum. We found a solution for the simulated problem in a form of new layout for the actual system with sparser middle-point distribution comparing with initial one.

In chapter 3 investigate principles of the 3D imaging by mm wave radar. It has been described how different types of migration using the frequency modulated signal radar provide a high resolution imaging of a target, and linear and rotating scanning have been used to achieve it.3D back projection algorithm was applied to reconstruct an image of a target and succeed in getting a precise position of it. Taking into account that the very high azimuth resolution could be achieved by synthetic aperture radar, the vertical resolution is still could be a problem. 3-channels system however performed quite good results in obtaining the high of the target position, allowed us to propose a way of tracking the radar system using rotating table. The experiment with tracking of the radar was done outside in two dimensions and in three dimensions in laboratory conditions.

Chapter 4 united ideas of previous chapters and present a simulations for the antenna arrays for the mm wave radar. The optimization algorithm was applied to the problem of antenna positioning for the MMW radar. The simulation with $L_{0.5}L_2$-norm cost function and random target distribution for 5 and 10 elements linear antenna arrays was done.

The last chapter 5 describing my final thoughts about the work that have been done. Each chapter represent the some ideas that could be developed in the future

Chapter 2 Optimization of a Sparse Array in Near Range

Sparse arrays are antenna arrays that originally were adequately placed, but where several elements have been removed. This is called “thinning”, and it results in the array being undersampled. Such undersampling, in traditional sampling theory, creates aliasing. In the context of spatial sampling, and if the aliasing is discrete, it is usually referred as grating lobes. In any case, this is unwanted energy in the sidelobe region. The Nyquist-Shannon sampling theorem [7] states that any signal of finite bandwidth B may be reconstructed from samples at uniform interval 1/2B. In a view of sampling rate, it is meant that sampling takes place indefinitely, or at least over a window that includes sufficiently many samples that edge effects may be ignored. This is not a good assumption in all applications. Most notably, sampling and spectral estimation are integral to the array processing problems of imaging and source localization. In fact, for a fixed system operating wavelength and under a far-field assumption, the array plane and measurement azimuth are equivalent to the time and frequency domains, respectively. A scene in which no signal is arriving from most directions is equivalent to a spectrally-sparse signal, and array element placement may be seen as sampling (where the “Nyquist” spacing is half the wavelength). When designing an array, one is restricted both by the number of elements and by the aperture size.

The number of samples is translated to the number of array elements that need to be placed, and the observation window translates to the required aperture. To make this concrete, let us assume some linear one-dimensional array with elements placed at a subset of the locations

$$t = n \cdot \frac{\lambda}{2} \text{ , } |n| \leq \frac{W}{2} \tag{2.1}$$

where λ is the length of wave and W is some observation window. Also assume that targets are in the far field and the scene is only described by a single angle (azimuth) θ; over these angles are some targets that transmit (or reflect) a fixed (over time) signal, which after the attenuation between the target and the array has complex amplitude X(θ). A sparse scene would be one where all of the incoming waves arrive from angles θ such that f = sin(θ)/2 satisfies the sparsity condition.

2.1 Sparse Array

2.1.1 Synthesis and optimization

Finding the positions giving the best results for a given criterion is an important issue for such systems. Recent work discussing sparse 1D and 2D arrays and optimal element placement have suggested different strategies based on minimizing the antennas number from the full array by minimizing the peak sidelobes or minimizing the integrated sidelobe ratio.

The lack of antennas that covers the same area as the dense array, however, could lead to the disadvantages of producing the artifacts in image reconstruction. The way of improving the resolution with the least aliasing lies in improving the imaging algorithms and configuration of the radiating part of the system. The latter could be achieved by optimizing the antenna pattern, due to different antenna layouts could have the radiation pattern with the lower sidelobes and the narrower main beam.

The performance of the developed approach is illustrated for a microwave imaging application. Design optimization is performed using two different initial array configurations, namely a uniform and a random configuration.

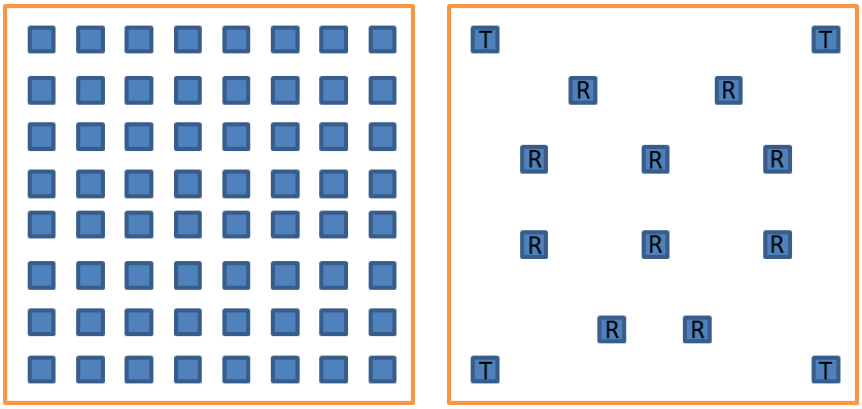

Figure 2 The dense and the sparse array.

The development of 2-D arrays could greatly improve the detection of small or low contrast structures. Many researchers have investigated the design of sparse 2-D arrays. Much of this work has centered on methods for reducing grating lobes. Turnbull and Foster [..] investigated the beam forming properties of sparse random 2-D arrays for ultrasound imaging and more recently investigated the design of sparse 2-D arrays with Gaussian distributed random elements.

To decrease the high number of elements required for some applications, but also the cost and power consumption, a thinning process is commonly applied. The thinning method reduces the element number by removing a part of the elements, depending on a thinning factor, following a suitable procedure. After the removal of antennas, the position of radiating elements will depend

on the applied thinning method. With thinning, the width of the main lobe remains almost unchanged but the antenna gain will suffer a reduction [10]. Outside the main beam, the control over the radiation pattern will decrease. Having this in mind, thinning is successfully applied when control outside the main beam is not very important and the main beam is narrow.

For large arrays, designing a narrow beam and low side lobes with amplitude tapering takes a high degree of computational workload. Skolnik presents in [11] a thinning method using density tapering, where the spacing between the elements is varied, not the amplitude. The density of elements of the thinned array is calculated using the amplitude taper of the filled array. The probability density function used for placing the elements is calculated with the amplitude taper and all the elements radiate with the same power. Therefore, amplitude tapering is not necessary.

For the other method the optimization by the antenna elements positions is applied. For the initial parameters of the optimization, the antena array with a high sparsity is chosen. The optimization criterion is usually a minimization of the maximum sidelobe. This is a criterion which is related to imaging of a strong reflecting point target in a non-reflecting background containing other point targets. An alternative criterion is to minimize the integrated sidelobe energy. In a medical imaging system, this is related to imaging of a non-reflecting area. Some results on weight optimization for 1D arrays using this criterion and quadratic optimization have been reported in [12].

2.1.2 Radar Used in the Study

The subject of the imaging performance improvement in my study is the two-dimensional sparse array system using Step-Frequency Continuous Wave (SFCW) radar for object recognition. The antenna array consists of 32 identical antennas: 16 transmitters and 16 receivers are able to acquire in total 256 channels signal at once. The frequency range of the system is 270MHz to 8GHz. Such wide band allows us to reach a high range resolution. We use spiral patch antennas with circular polarization in order to make the image recognition independent from the target attitude – right-hand circular polarization for transmitting and left-hand for receiving. The antenna consists of two-arm archimedean spirals and a balancing unit to feed them. It has the central frequency around 5 GHz and wide beamlobe with 11, 3 dBi gain.

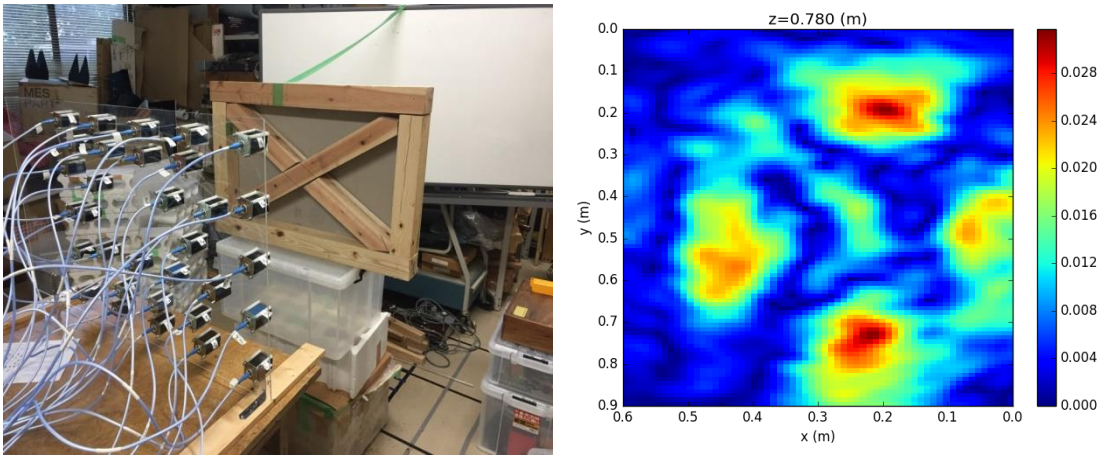

Figure 3 Sparse array at wall inner structure investigation.

All antennas in the array are placed in the way to have a large aperture for a close distant wall survey. The advantage of the sparse array in comparison with dense equally spaced antenna array is that it gives a solution to the problem of grating lobes. Due to the spatial aliasing effect, these sidelobes occur when we put antennas more than half wavelength distance apart. That is why we have to increase an antenna number when we try to make a larger array aperture. The sparse array is able to increase the aperture keeping not so much amount of the radiating elements in comparison to the dense array, which could also give a time-boost in cases of complicated time-consuming algorithms of processing and object imaging. However, the better layout optimization should be introduced.

2.1.3 Antenna for the sparse array

It is found that the archimedean spiral antenna is more suitable for SAR compared to the equiangular spiral antenna [13]. The appearance and design of the antenna are shown in Fig.4 The patch antenna has the balancing unit – a 50 to 110 Ω taper balun - in order to feed the balanced spirals from the unbalanced coaxial line. The central part of the antenna is covered by absorbing material discarding the back propagation of the spiral element.

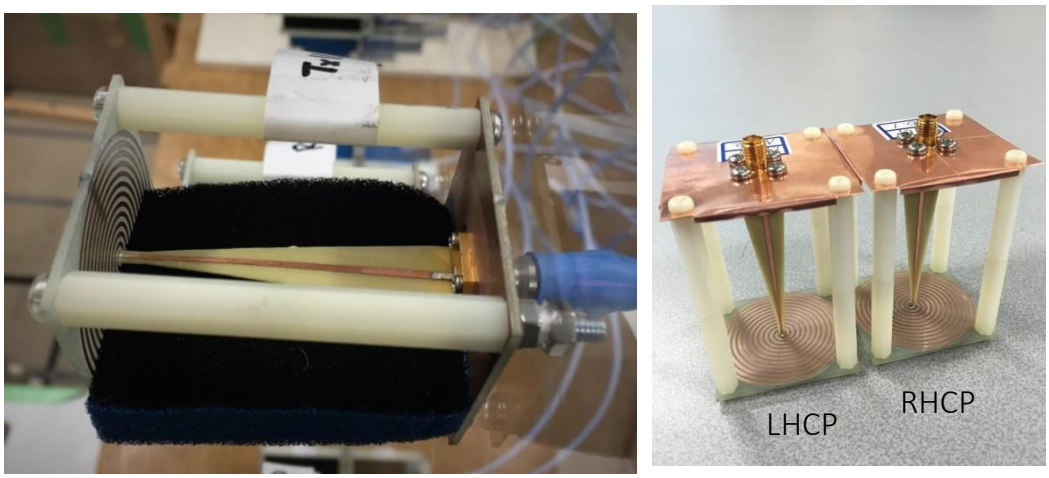

Figure 4 Antenna array element, the spiral antenna with the balancing unit attached to it.

Microstrip lines are designed to feed antenna from coaxial line taken from [13]. Fig 5 shows the dimensions and design of the antenna and the balancing unit. Two 6-turns archimedian spiral lines were printed on a 5mm high-permittivity ($\varepsilon_r = 4.3$) FR-4 substrate.

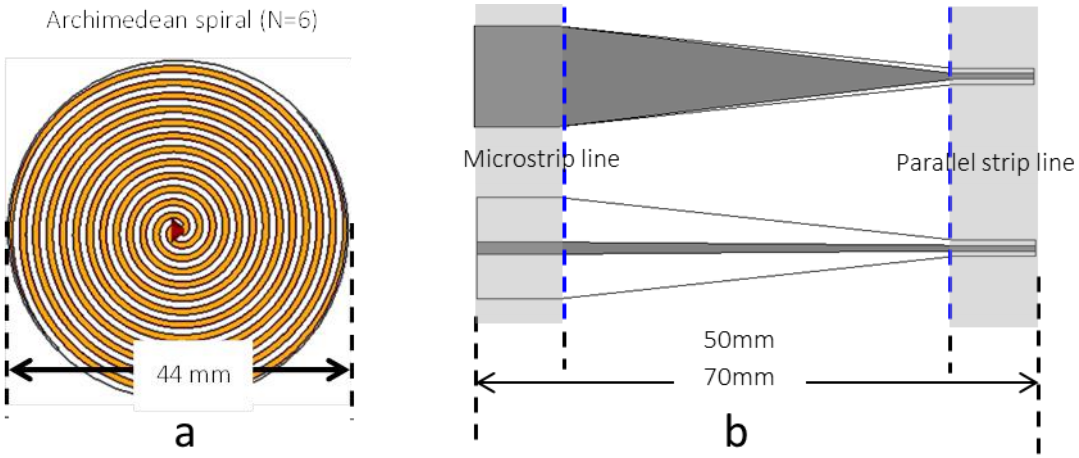

Figure 5 Spiral element (a) and the balancing unit sizes (b).

The performance of the antenna elements is introduced in Figs. 6 - 7. Fig. 6 represents the reflection coefficient in the time domain. Here are six antennas taken randomly from overall measured using a Vector Network Analyzer (VNA). In this figure the reflections from the SMA connector and the patch antenna are observed; performance is directly depends on the quality of the soldering. In the Fig. 7 the reflection coefficient in frequency domain has been shown, and the blue square here represent the radar frequency band. The mean S11 below -20dB shows that antennas radiate energy best at those frequencies.

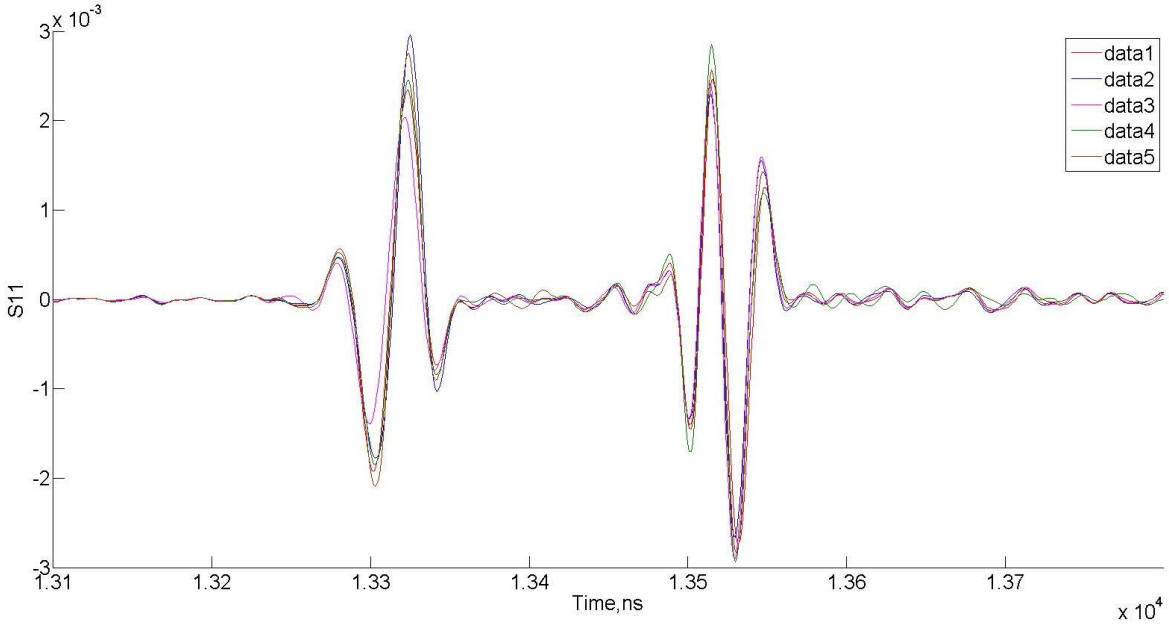

Figure 6 Reflection coefficient in time domain for different antennas.

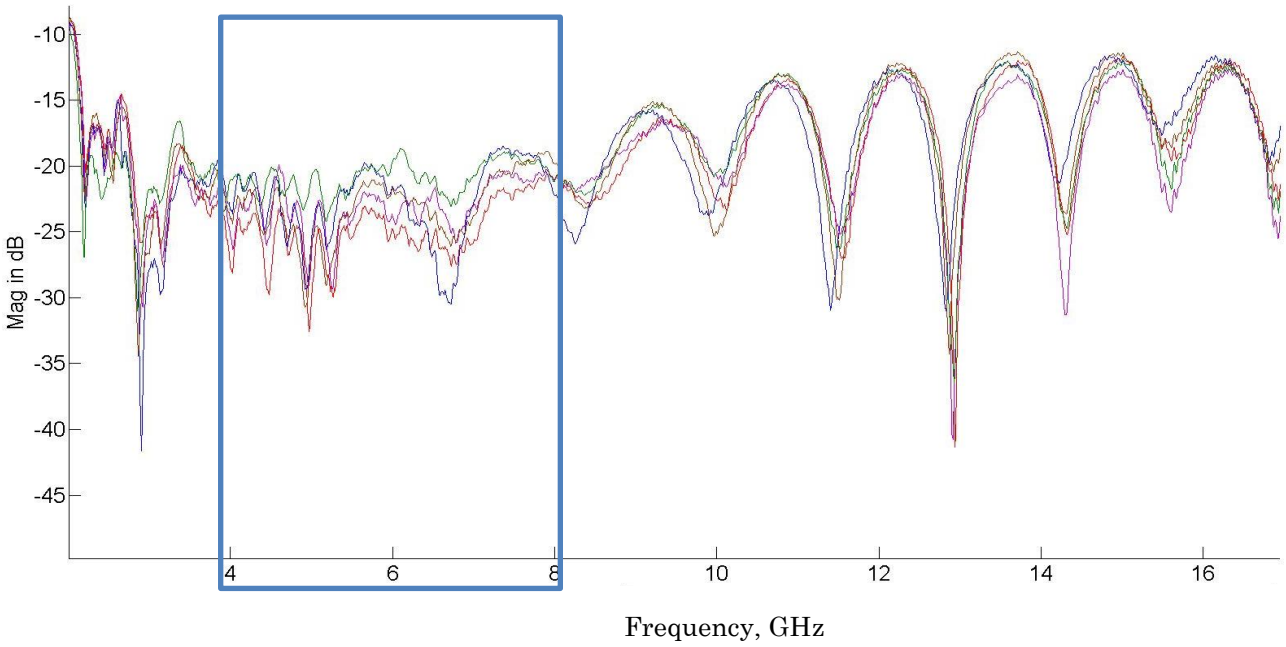

Figure 7 Reflection coefficient in frequency domain. Blue square indicate the radar frequency range

The antenna pattern was calculated by CST Microwave Studio in the Finite-Difference Time-Domain (FDTD) transient solver to see field propagation along the traces in E-plane. Figs. 8-9 represent a radiation pattern of the spiral antenna in 3D and in 2D in linear scale correspondingly. Numerical calculation was done at 4.5GHz.

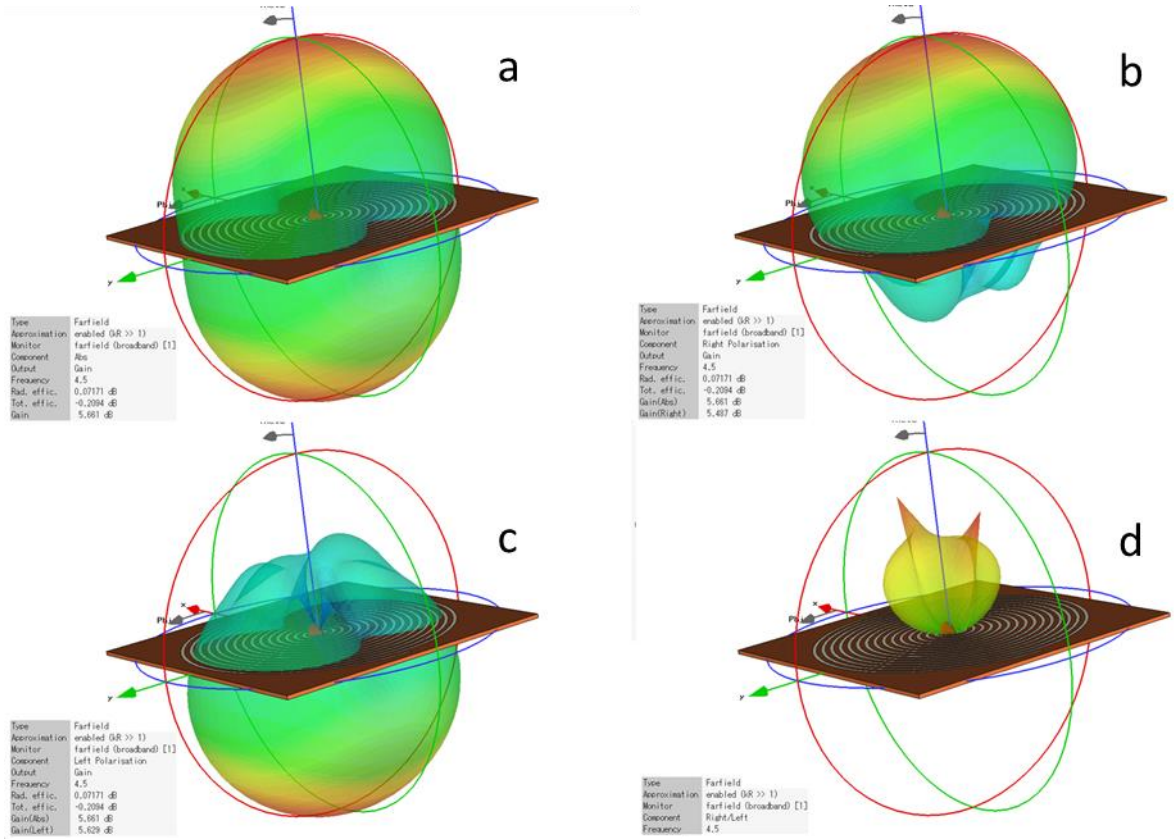

Figure 8 Radiation pattern of the Spiral Antenna in 3D calculated at 4.5GHz. A – absolute value, b – right hand polarization component of the field, c - left hand polarization component, d – ratio of the right to left components.

Fig. 8 represent the calculated farfield in 3D for the typical right hand circular polarization spiral antenna. Taking into account the fact that signal changes its polarization when it reflects from the target, we do not use a polarization information in the simulation of the traveling signal and simulation of the radar system for the optimization algorithm. We only consider thiss information when we build up an antenna array to have the antennas with different polarization for the transmitters and receivers. The second point to consider is a strong back propagation field that should be reduced to not have an influence upon the receiving signal.

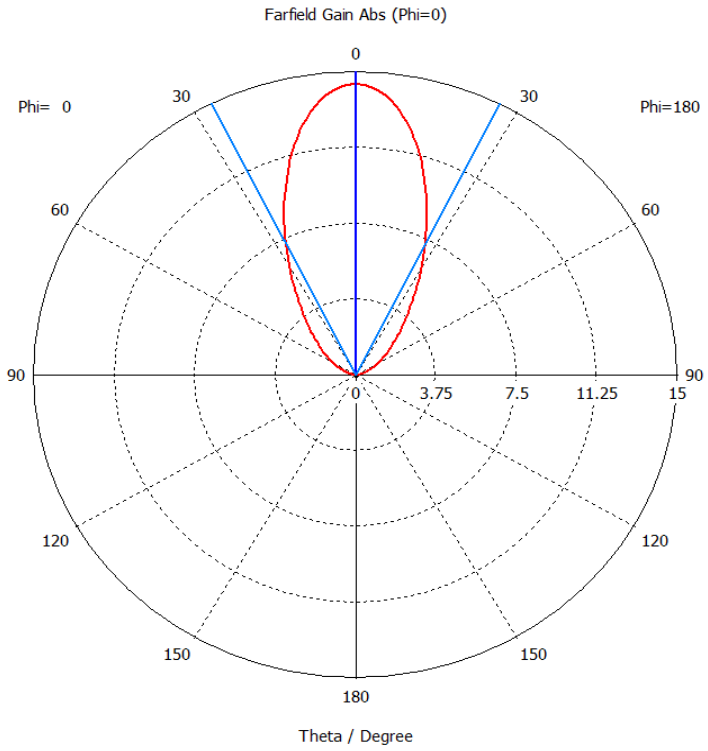

Figure 9 Radiation pattern of the Spiral Antenna in linear scale in 2D calculated at 4.5GHz.

The main beam width of the antenna is about 49 degrees, and the antenna gain at simulated frequency is 11.3dBi. The result of the calculation can be used in the image reconstruction. Simulation of the sparse array imaging based on the point spread function will be more related to the actual system, if we approximately take a directivity coefficient according to the direction of transmitting (arriving) signal.

In order to decrease a strong reflection from the back propagation of the spiral element the absorbing material has been placed along the sides of the balancing unit as it can be seen from Fig.10

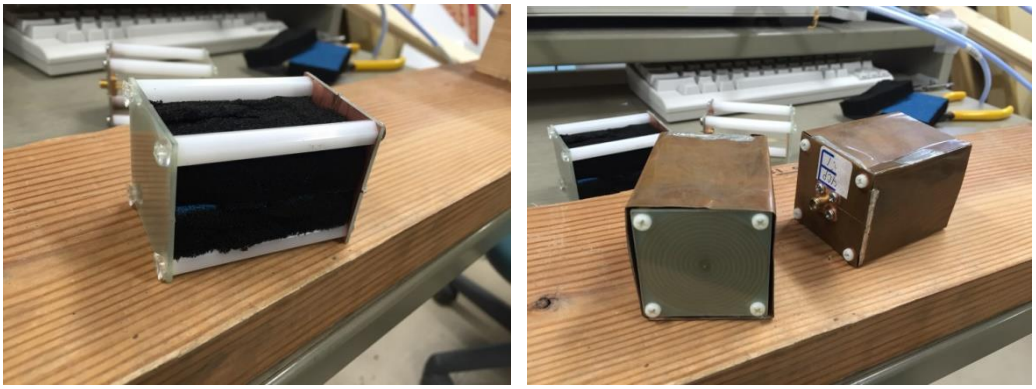

Figure 10 Antenna with absorbing material (a) and placed in copper cavity (b).

To see if it is enough I measured a transmission between antennas, ones with just an antennas, ones with an absorbing material and ones with antennas placed in a copper cavity. Results of the

measurements done on the VNA could be seen at Figs. 11-12. Here comparison of S21 between three antenna cases represented both in a time and frequency domains.

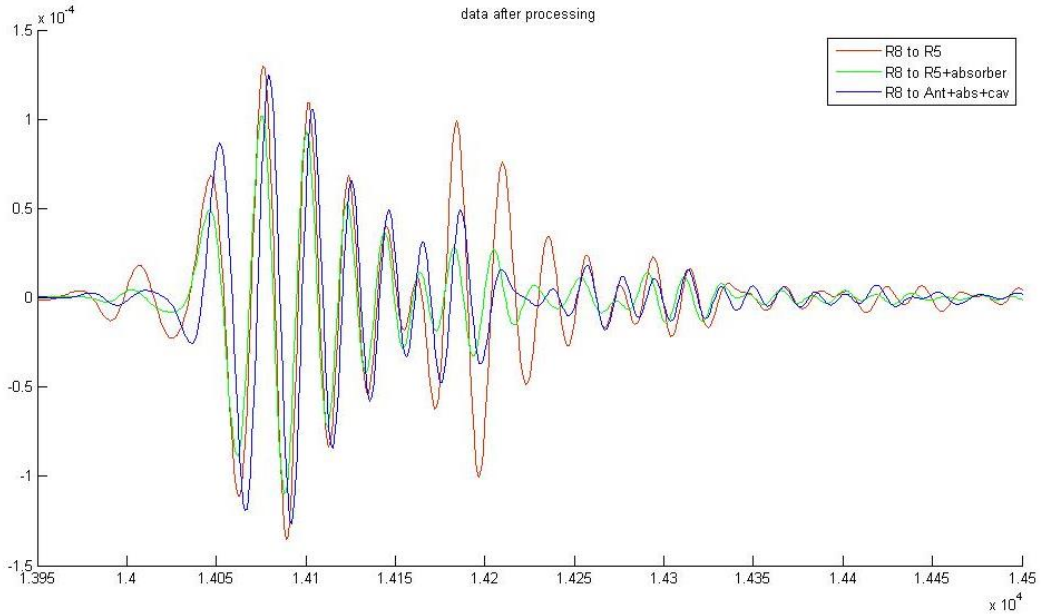

Figure 11 Transmission between two spiral antennas in time domain.

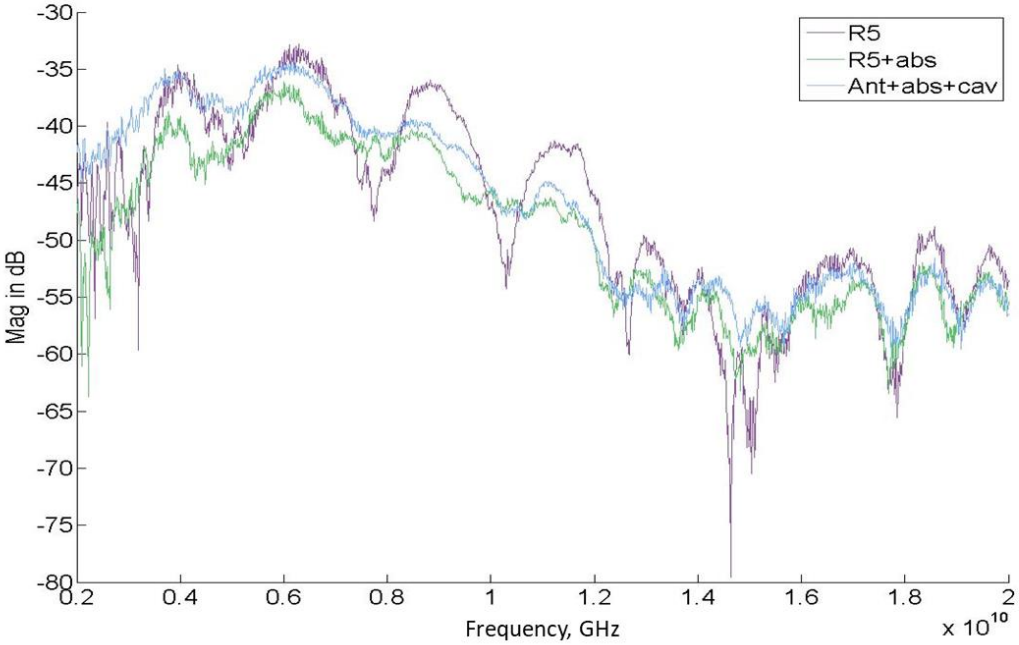

Figure 12 Transmission between two spiral antennas in frequency domain.

From Fig. 11 it can be seen that the additional back reflections of the spiral. Both cavity and absorbing material reduce it, though the only absorber using showed better results, which is also could be seen in Fig.12: here the antennas with absorbing material have in average 4dB higher transmission along the radar frequency band (4 to 8 GHz).

2.1.4 Middle point approximation

The current system has a 2D sparse antenna array in order to obtain the 3D image of a target and several image reconstruction methods, which include the least square and Compressive Sampling Matching Pursuit. The layout for it was build using the middle point approximation [10] that allows any bistatic radar to be associated with a monostatic one.

$$t_{Monostatic} = \sqrt{t_{Bistatic}^2 - \left(\frac{d}{c}\right)^2} \tag{2.2}$$

Where d is a distance between two antennas.

The middle point located at the center between two antennas for each pair transmitter-receiver of the bistatic radar system (Fig.13).

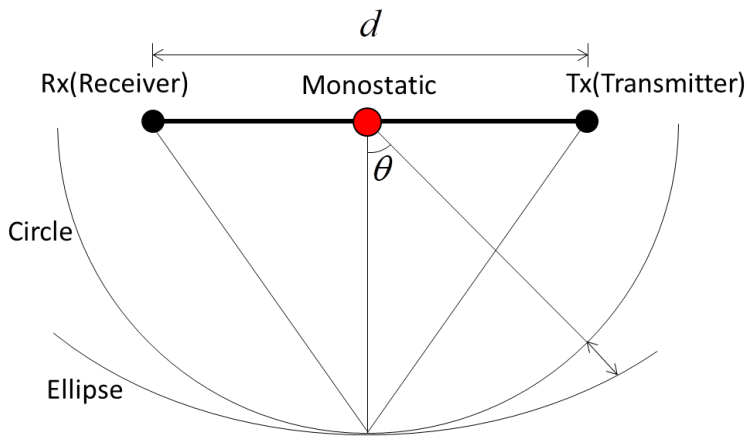

Figure 13 Middle point geometry calculation.

The middle points were uniformly distributed in a rectangular area, though transmitters were put at the edges and receivers are located inside the rectangular. The total size of the 32 antenna array is 75 by 54 cm with middle point distribution area 64 by 45cm. This layout was tested with several experiments showing good results, however, the investigation of the possibility of array optimization should be followed.

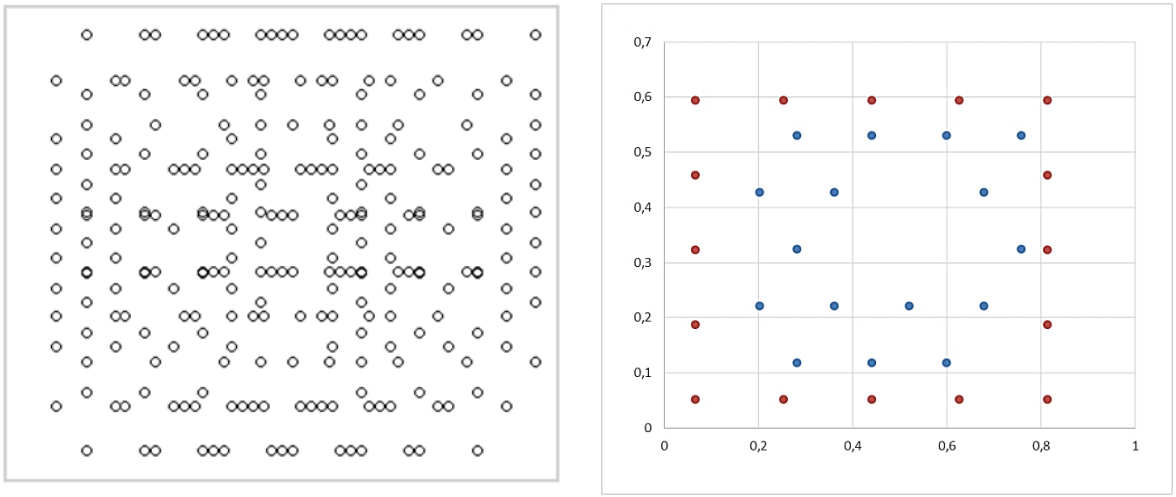

Figure 14 Middle points distribution; (a) and antennas displacement; (b) Transmitters shown by red dots and receivers - by blue dots.

Despite the antenna array layout is not symmetrical, it can be seen that the middle point distribution is quite sparse. Though there is still much space between points and some of them are overlapped. To see if the other layout with more sparse middle point distribution can improve an imaging performance of the actual system, it has been decided to use this antenna pattern as initial for optimization

2.2 Optimization algorithm

2.2.1 Image reconstruction

The optimization method starts from simulation of the antenna array and imaging area, that computes the radar cross-section over the all imaging area, thus each cell (or pixel) is separated computed. The amplitude of the signal at each point in the scan was calculated by summing, over each transmit and receive element, an appropriately delayed and weighted pulse. Fig. 15 represents a geometry of the simulation, the calculated two-way signal from antenna array to the target.

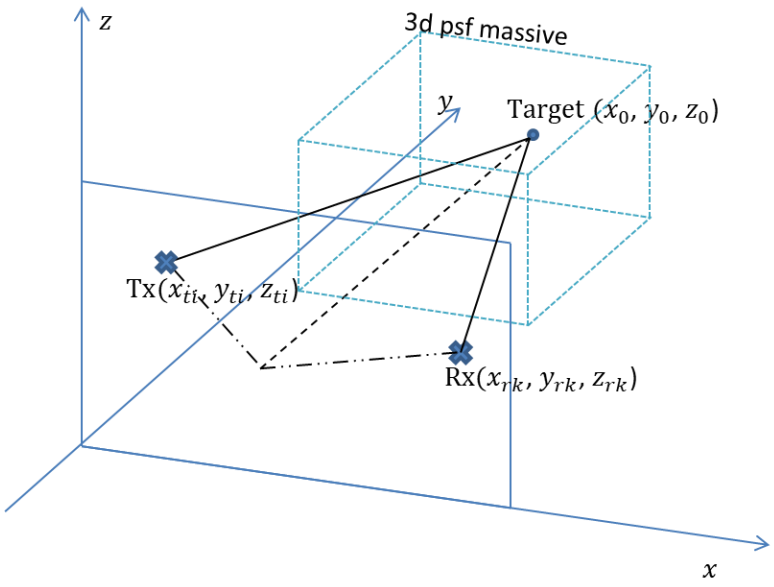

Figure 15 Calculation of the signal for the one Tx-Rx Pair.

To get the focused image of the targets by composing all Tx-Rx signals at each point of imaging area in front of the radar system, I used the back projection algorithm. In this way the reconstructed image is represented by:

$$U(x_0, y_0, z_0) = \sum_{i,k}^{n} R_{i,k} d_{i,k}(\tau_{i,k}) e^{j2\pi f \tau_{i,k}} \quad (2.2)$$

where $d_{i,k}$ is the measured signal and $\tau_{i,k}$ is the travel time for one transmitter-receiver pair at i,k-th positions, $A_{i,k}$ is the measured amplitude and $R_{i,k}$ is the coefficient calculated from the angles between the direction of the reflected signal and direction of the antennas. This is an approximation that considers a radiation pattern in our simulation. Coefficient for each transmitter-receiver pair is taken according to the radiation pattern of the spiral antenna calculated in section 2.1.3.

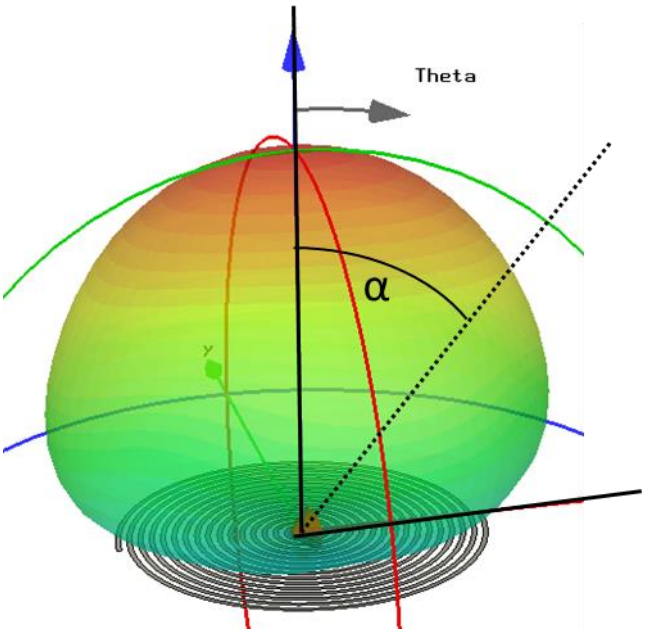

Figure 16 Calculation of the radiation pattern coefficient according to the angle between antenna direction and the signal to the target.

Time delay could be calculated according to:

$$\tau_{i,k} = \frac{\sqrt{(x_0-x_{ti})^2+(y_0-y_{ti})^2+(z_0-z_{ti})^2}}{c} + \frac{\sqrt{(x_0-x_{rk})^2+(y_0-y_{rk})^2+(z_0-z_{rk})^2}}{c} \quad (2.3)$$

In order to weaken the artifacts and focus the targets in whole imaging area we use the cost function described below:

$$S = \frac{\left\| U(x,y,z)|_{x,y\notin\Omega,\ \forall z} \right\|_{L2}}{\left\| U(x,y,z)|_{x,y\in\Omega,\ \forall z} \right\|_{L0.5}} \quad (2.4)$$

where Ω is the position of the targets. For a given number of antennas, the goal in the optimal design is to obtain an array configuration that minimizes this cost function. For this purpose, the optimization starts with an initial antenna configuration that usually taken from the dense array or the actual systems.

2.2.2 Cost function

The method optimizes the antenna pattern by changing the positions of receivers and transmitters. To find the new pattern, which improves a resolution of the imaged targets, we proposed a cost function based on the relations between two norms of the 3D reconstructed image. The simulated antenna array is applied to a problem of imaging the target in front of the radar in different directions. Then cost function is minimized by using the heuristic optimization algorithm, and antennas coordinates are the optimization parameters. Each iteration the algorithm changes values of the coordinates according to the optimization step and calculates a

point spread function (PSF) for the current array.

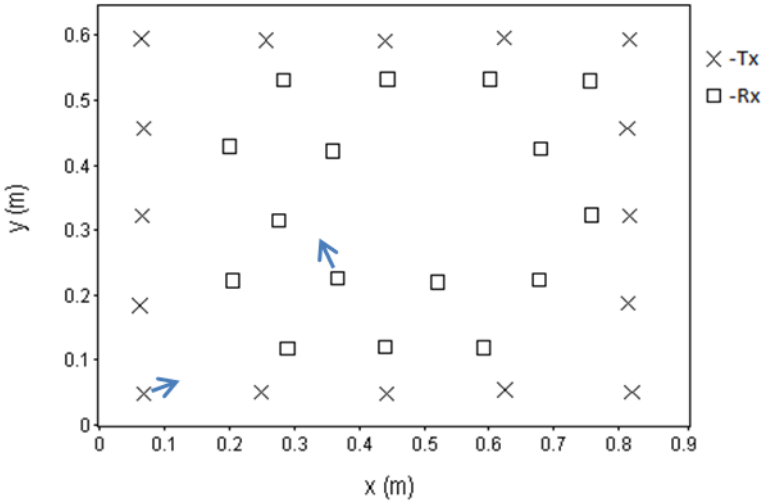

Figure 17 Optimization by changing the antennas positions.

Then it compares the cost function with cost function of the previous iteration, moving to its minimum. As the way to avoid local minimums, the random targets distribution has been used. Each step of the iteration the targets displacement changes, forcing the algorithm to search for a new function minimum.

$$S = \frac{\left\| U(x,y,z)|_{x,y,z\notin\Omega} \right\|_{L2}}{\left\| U(x,y,z)|_{x,y,z\in\Omega} \right\|_{L0.5}} \tag{2.5}$$

In the Fig. 2.12 it is shown which points of reconstructed image the different L-norms took place.

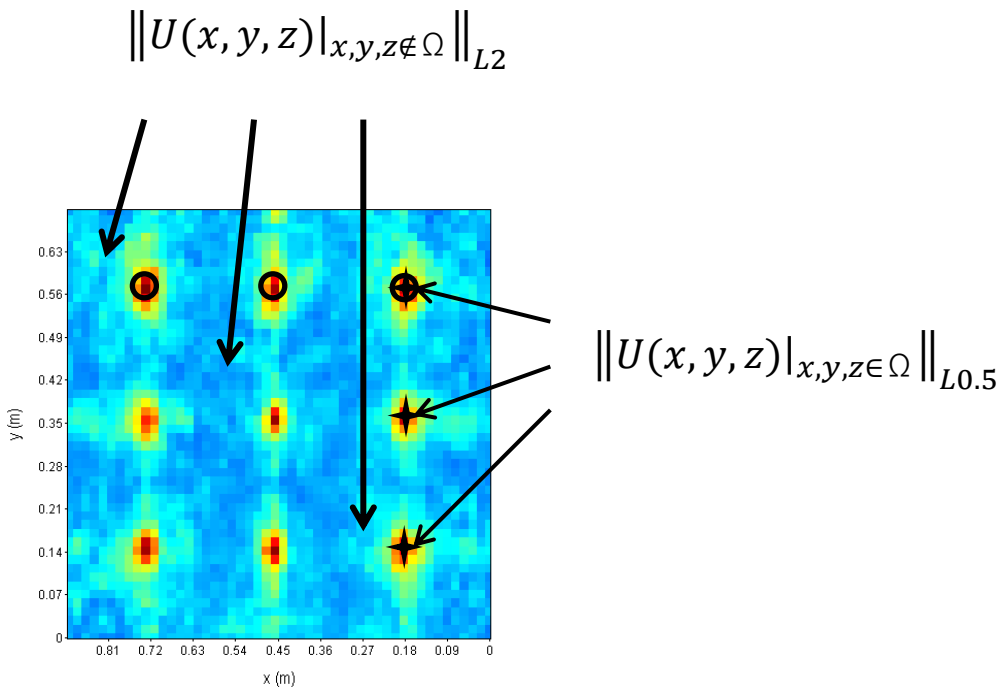

Figure 18 Areas of norm calculations on the reconstructed image.

During the optimization process we minimize the cost function. In the upper part of the fraction we take an *L*-norm of the reconstructed image higher than one in all positions except targets in order to not only minimize but also equalize the artifacts level. And in denominator, we put an *L*-norm lower than one in targets positions to maximize and equalize the level of the targets. The reason of using these norms is that the conventional way, which is an optimization of the signal-to-noise ratio, uses the relation of two L2-norms that is encourage the large components over the small components whenever we maximizing it. It means that the total result of optimization will lead to making the higher component targets even higher keeping the small component targets on the lower level.

To describe how does the norms, less than 1, and higher than 1 behave in terms of our problem, let us represent the norms behavior in a form of a unit circles. At first we define *Lp* norm for *x* as:

$$\|x\| = \sqrt[p]{\sum_i |x_i|^p} \quad \text{where p}\in\text{R} \tag{2.6}$$

and so L_2 and $L_{0.5}$ accordingly as:

$$\|x\|_2 = \sqrt[2]{\sum_i |x_i|^2} \tag{2.7}$$

and

$$\|x\|_{0.5} = \sqrt[\frac{1}{2}]{\sum_i |x_i|^{\frac{1}{2}}} \tag{2.8}$$

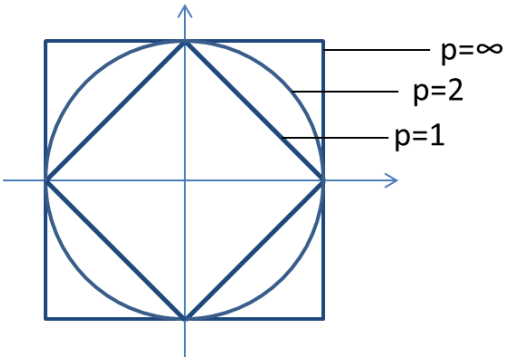

Figure 19 Illustration of unit circles in different norms.

If we go to p=1, our grid norm above, then for two values we are plotting the equation $|x_1| + |x_2| = 1$, which is just four line segments connecting the points (1,0), (0,1), (-1,0), and (0,-1). Fig. 2.13 shows the unit circles for p=1,2, ∞.

The L2-norm is simply the length of the vector ($\sqrt{x_1^2 + x_2^2}$ for the 2-dimensional case). Therefore it makes sense that all points of the same length form a circle around the origin. The infinity norm is defined as $\|x\|_\infty = \max\{|x_1|,\ldots,|x_n|\}$. Therefore, $\|x\|_\infty = 1$ for all (x_1,x_2) where either $|x_1| = 1$ and $|x_2| \leq 1$ or $|x_1| \leq 1$ and $|x_2| = 1$.

In Rn for n higher than 1 the (2.5) defines an absolutely homogeneous function of degree 1 for $0 < p < 1$. For the L_p norms in R^2 ($1 \leq p \leq \infty$):

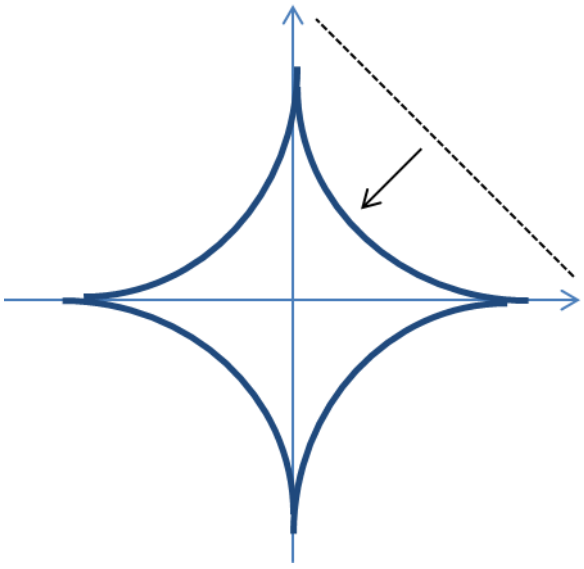

Figure 20 Illustration of unit circle for p=1/2 during minimization of the norm.

And the L_1-norm, whenever it minimized or maximized, has no preference between a few large components and many small components.

To compare the cost function with different L-norms we made a simulation where we trying

to find a solution for cost function to image three targets with different amplitude.

Noting (2.4) let us define

$$\|U(x,y,z)\|_{LhLk} = \frac{\|U(x,y,z)|_{x,y\notin\Omega,\ \forall z}\|_{Lh}}{\|U(x,y,z)|_{x,y\in\Omega,\ \forall z}\|_{Lk}} \tag{2.9}$$

For h,k=0.5, 1 and 2.

From representation of the norms behavior an equalization of the values is still not obvious, but could be observed in applying to the optimization algorithm. Initially we have three targets in front of the antenna array, one in the middle has a higher amplitude. During optimization, we use a different cost function to see how it will effect on the imaging result. In the Fig.20-21 there is a comparison between imaging profiles after optimization.

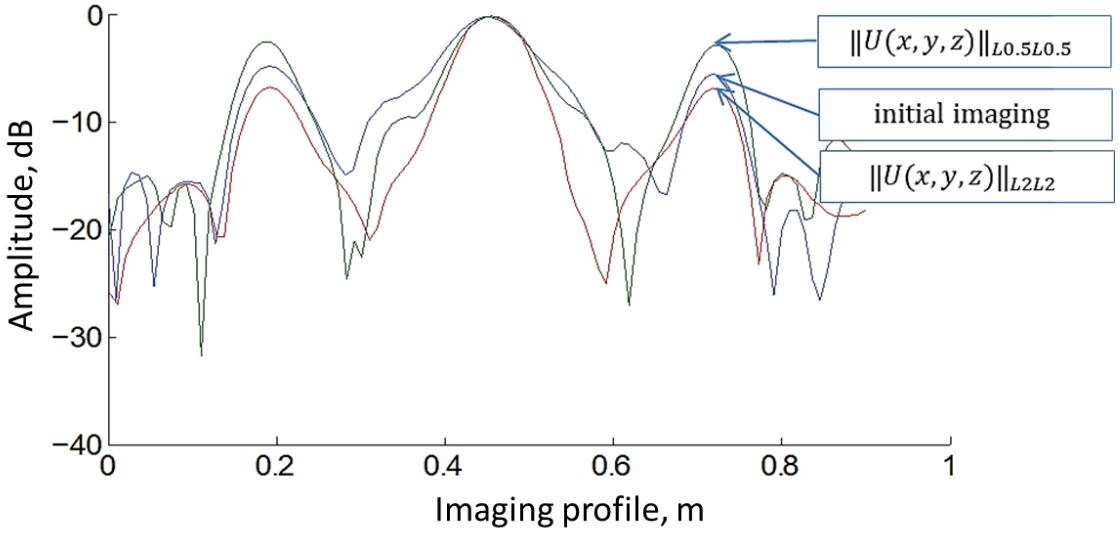

Figure 21 Result optimization with $L_{0.5}L_{0.5}$-norms and L_2L_2-norms cost functions.

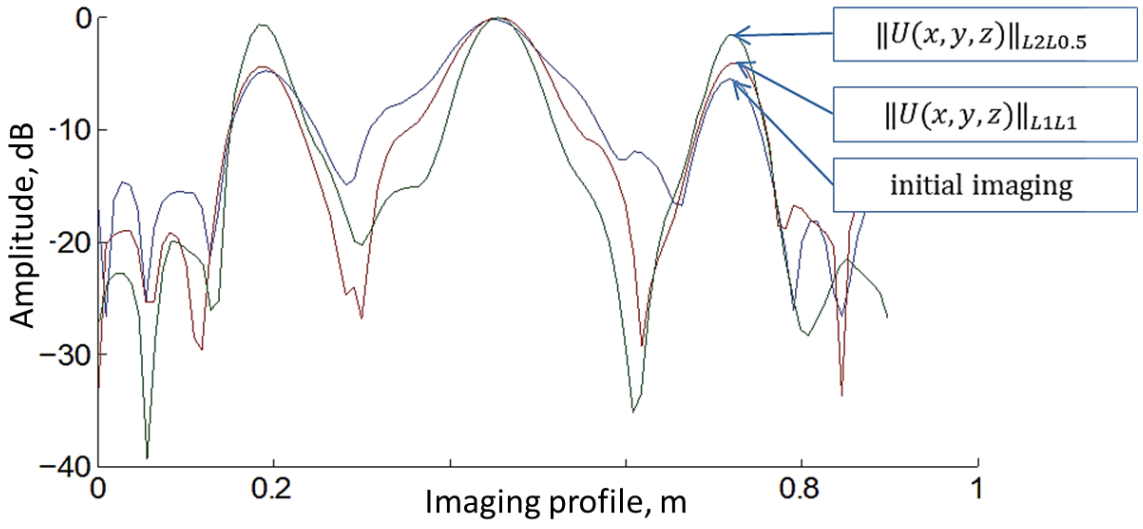

Figure 22 Result optimization with $L_2L_{0.5}$-norms and L_1L_1-norms cost functions.

As it was assumed the cost function with L_2L_2-norm kept the same values for lower component targets and focused the higher component target in the middle, on the other hand, $L_{0.5}L_{0.5}$-norm cost function equalized the target level but has not reduced artifacts level well enough. And as it could be seen from the Fig.21 $L_2L_{0.5}$-norm cost function reduced the noise level and focused targets uniformly.

2.2.3 Optimization algorithm

There are several algorithms for optimizing element deactivation; many of them are detailed in [17] together with their simulation results. All these methods aim to reduce the side lobe level while maintaining the width of the main lobe constant. The most frequently used methods are simulated annealing and genetic algorithms [18]. For the cost function minimization, we use the gradient descent algorithm which is well-known first-order iterative optimization algorithm.

The way it works is we start with an initial guess of the solution and we take the gradient of the function at that point. We step the solution in the negative direction of the gradient and we repeat the process. The algorithm will eventually converge where the gradient is zero (which correspond to a local minimum). The both, gradient descent and gradient ascent finds the local maximum nearer the current solution by stepping it towards the positive direction of the gradient, are first-order algorithms because they take only the first derivative of the function.

Let's say we are trying to find the solution to the minimum of some function f(x). Given some initial value x0 for x, we can change its value in many directions (proportional to the dimension of x: with only one dimension, we can make it higher or lower). To figure out what is the best direction to minimize f, we take the gradient ∇f of it (the derivative along every dimension of x). Intuitively, the gradient will give the slope of the curve at that x and its direction will point to an increase in the function. So we change x in the opposite direction to lower the function value:

$$x_{k+1} = x_k + \gamma \nabla f(x_k) \tag{2.10}$$

The γ>0 is a small number that forces the algorithm to make small jumps. That keeps the algorithm stable and its optimal value depends on the function. Given stable conditions (a certain choice of γ), it is guaranteed that $f(x_{k+1}) \leqslant f(x_k)$.

A wrong step size γ may not reach convergence, so a careful selection of the step size is important. Too large it will diverge, too small it will take a long time to converge.

Any differentiable function has a maximum derivative value, i.e., the maximum of the

derivatives at all points. If this maximum is not infinite, this value is known as the Lipschitz constant and the function is Lipschitz continuous [19].

$$\frac{\|f(x)-f(y)\|}{\|x-y\|} \leq K(f), \text{ for any x,y} \tag{2.11}$$

This constant is important because it says that, given a certain function, any derivative will have a smaller value than the Lipschitz constant. The same can be said for the gradient of the function: if the maximum second derivative is finite, the function is Lipschitz continuous gradient and that value is the Lipschitz constant of ∇f.

$$\frac{\|\nabla f(x)-\nabla f(y)\|}{\|x-y\|} \leq K(\nabla f), \text{ for any x,y} \tag{2.12}$$

Each iteration it changes the antennas position making a step proportional to the negative of the gradient of the function at the current point:

$$a_{l+1} = a_l + \gamma \nabla S(a_l) \tag{2.13}$$

Where

$$\bar{a_l}\begin{Bmatrix}(x_r, y_r, x_t, y_t)_1, \\ \dots \\ (x_r, y_r, x_t, y_t)_i\end{Bmatrix} \tag{2.14}$$

Where γ is the coefficient describing how fast function moves to the gradient, and l is the number of iteration.

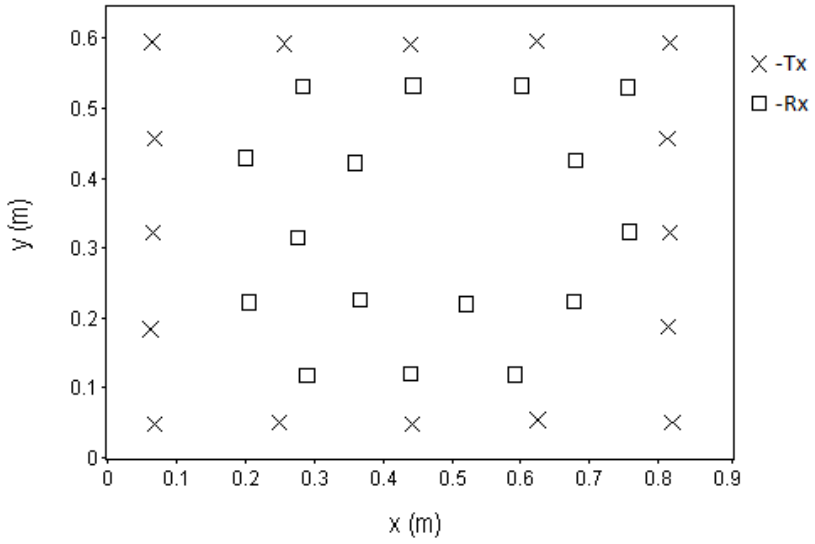

Figure 23 Initial layout for the optimization.

The parameter of the optimization is the coordinates of the antennas, and for the initial values we took positions of the antenna array elements from the actual system used in the study in order to improve radar performance.

The simulation with fixed target positions below shows the algorithm work and compared the

focused images with the optimized and un-optimized antenna array. To get the focused image of the target in different positions we first simulate 27 point-targets in front of the array: 9 targets at 0.2m, 0.5m and 0.8m range The sizes of the antenna array was taken from the actual one that we used in our study.

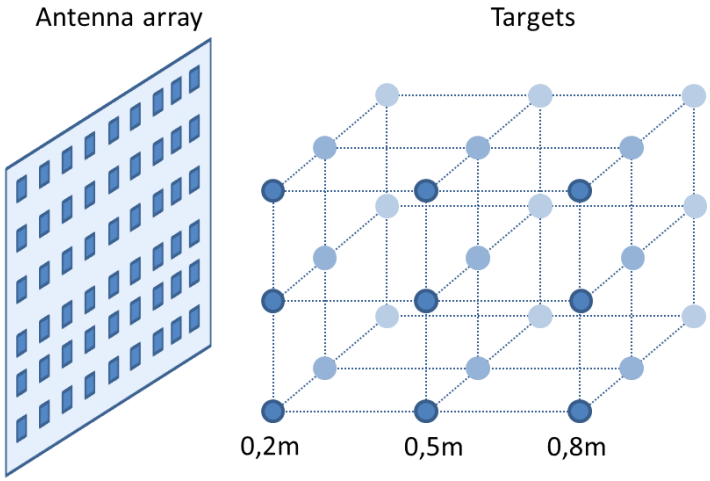

Figure 24 Simulation set-up.

A 3D stacked PSF figures represent 100 stacked slices along the z-direction from 0 to 1m (toward the face of the array), so we can see the stacked image of all 27 targets.

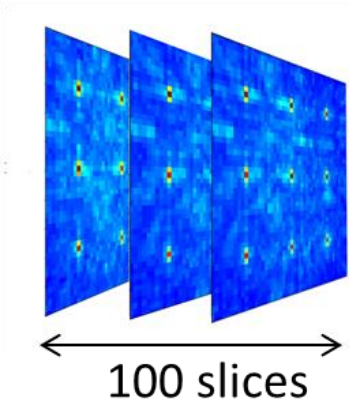

Figure 25 Representing of the stacked image.

In Fig. 25 we show results of the simulation of the dense equally spaced antenna array and sparse array. In this simulation, we uniformly change the size of both antennas and plot the dependence of the cost function we used on the scale factor. The scale factor is a value describes how much time we enlarge the array from its initial size. The figures represent 50 stacked slices along the z-direction from 0 to 1m (toward the face of the array), so we can see the stacked imaging of all 27 targets.

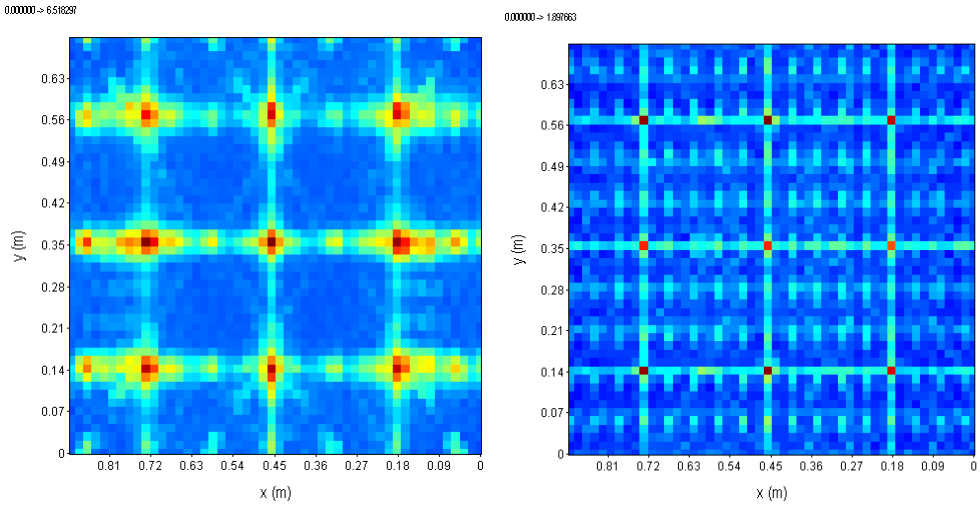

Figure 26 Stacked 3D PSF of the 27 targets imaged by 256 elements antenna array (a) and 9 times enlarged array (b) with same amounts of the elements.

We can see well, as it was expected, the grating lobes at the image made by the enlarged array. For the scale factor *m*, linearly changing during optimization, the positions of the antennas changes from initial x_0, y_0 as:

$$\begin{cases} x = mx_0 \\ y = my_0 \end{cases} \tag{2.15}$$

And the cost function progress, representation of changing value of the cost function during the simulation, could be seen on the Fig

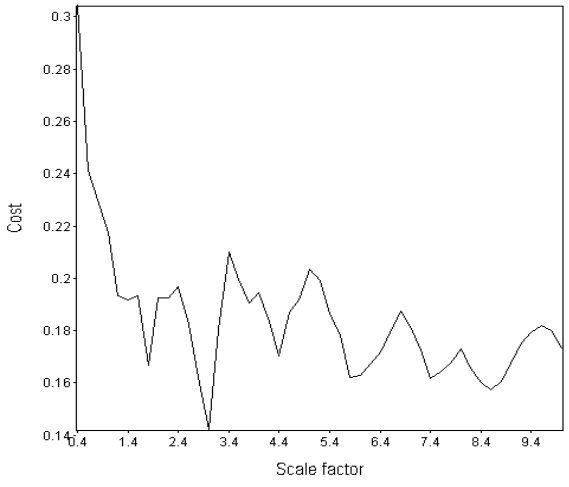

Figure 27 Dependence of the function on the scale factor for 256 elements dense antenna array.

Then after we made a simulation of the 32 elements sparse array scaling its size in the same way to see how the array deals with the grating lobes problem.

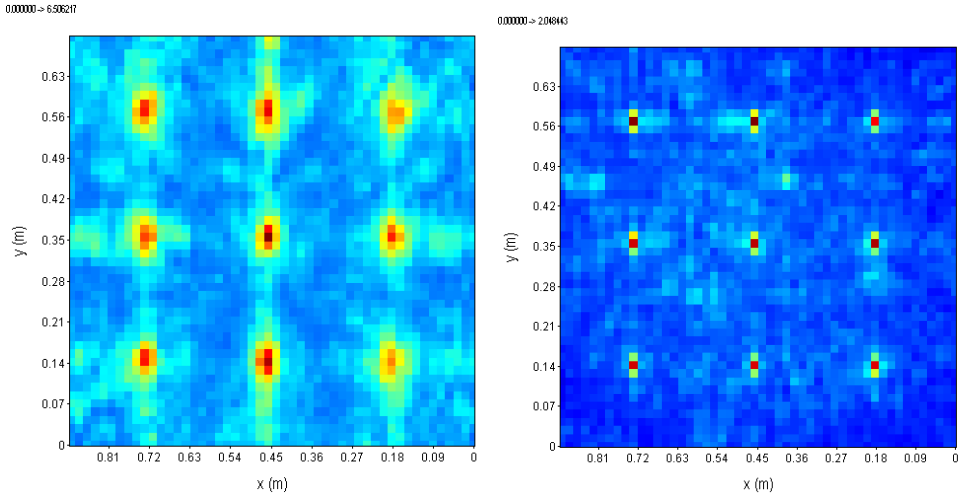

Figure 28 Stacked 3D PSF of the 27 targets imaged by the 32 elements sparse array and 9 times enlarged array (b) with same amounts of the elements.

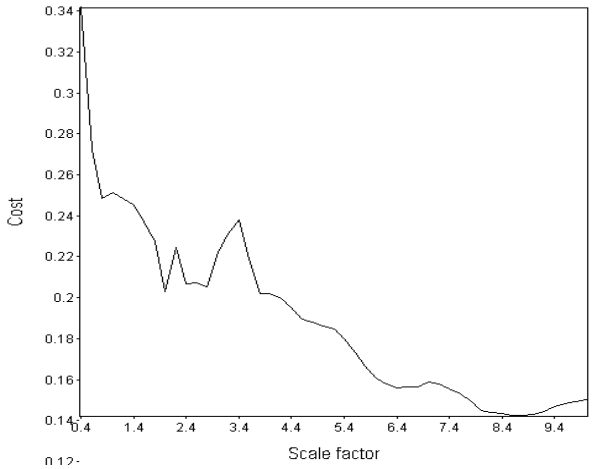

Figure 29 Dependence of the function on the scale factor for the 32 elements sparse array.

The figures also show the behavior of the cost function that can help us to see how it will be changing when we apply the optimization algorithm. From the figures imaged by sparse array, we observe not only a lack of the artifacts but also how the performance of the radar used in this study could be improved if we make larger aperture.

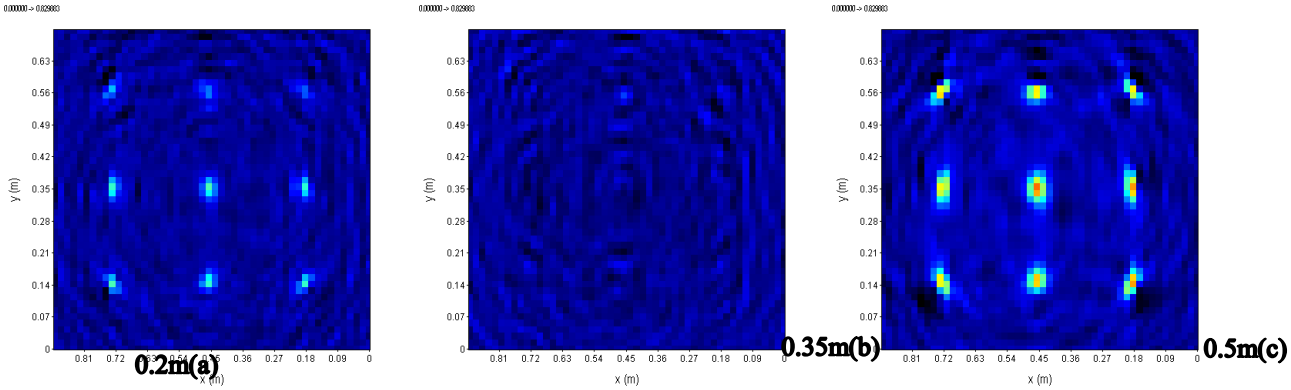

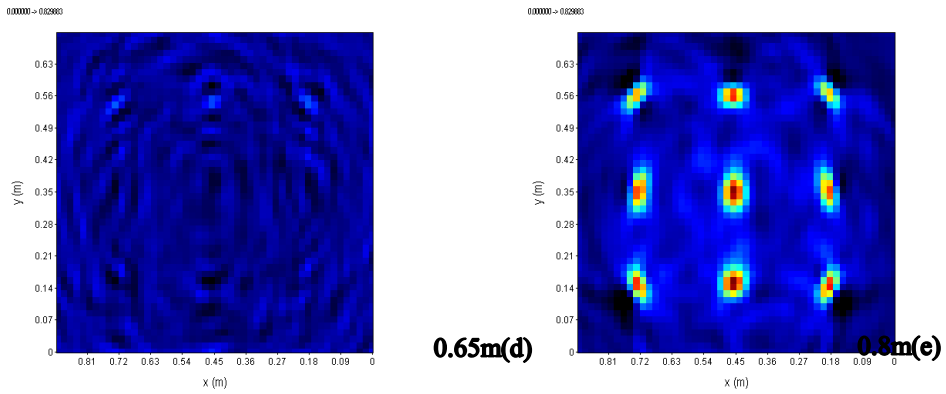

Figure 30 Slices of the 3D image of the targets at 0.2m(a), 0.35m(b), 0.5m(c), 0.65m(d) and 0.8m(e), imaged by optimized array.

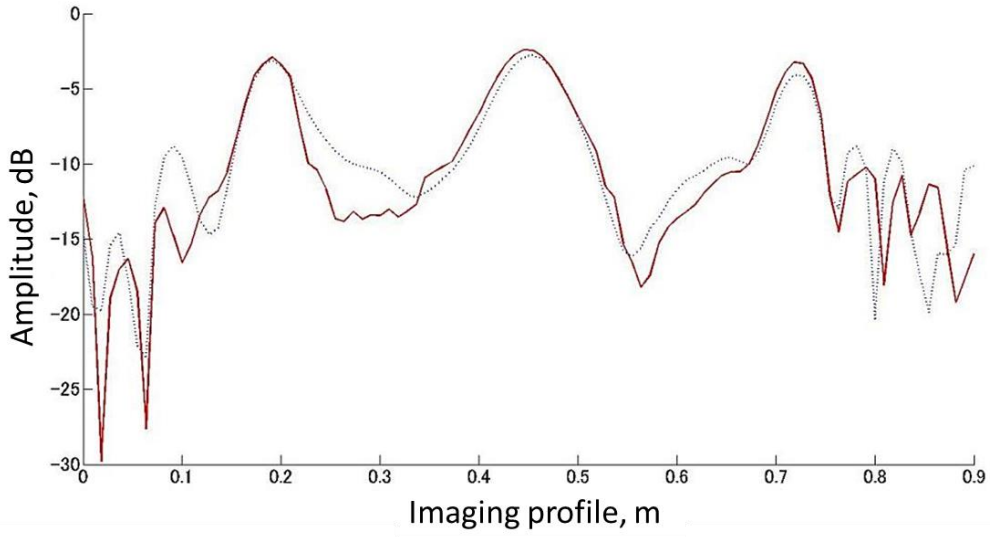

Figure 31 Comparison the optimized layout and initial one.

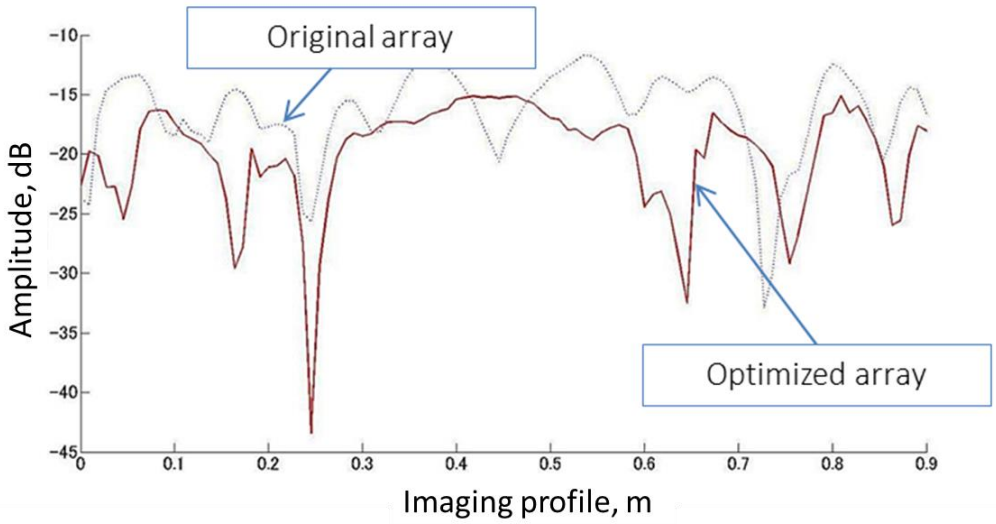

Figure 32 Comparison the optimized layout and initial one.

2.2.4 Model Validation

As soon as in my optimization method the actual sparse array system was simulated we can compare how our simulation related to the experimented results. The influence of the approximation in using calculated radiation pattern of the antenna should be also noted. Results of the experiment to evaluate the simulation for the proposed method are represented in Figs 32-25.

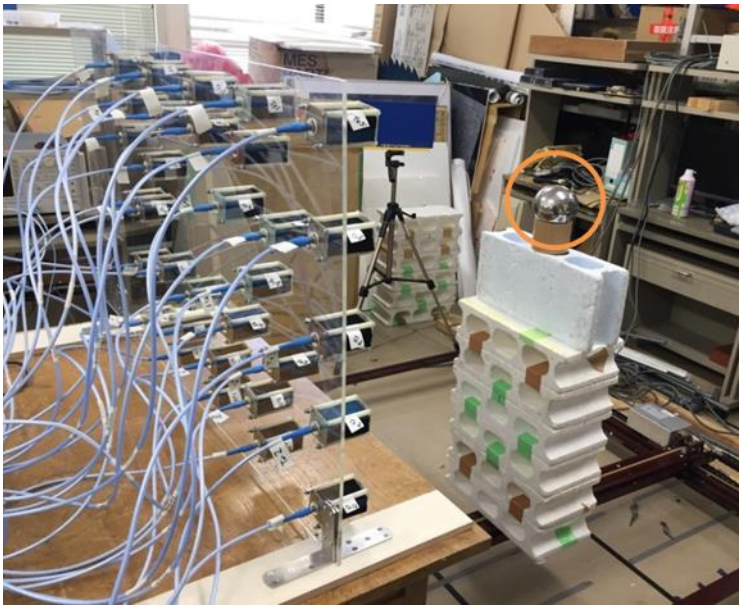

Figure 33 Experiment set up with a metal sphere moving away from the array aperture.

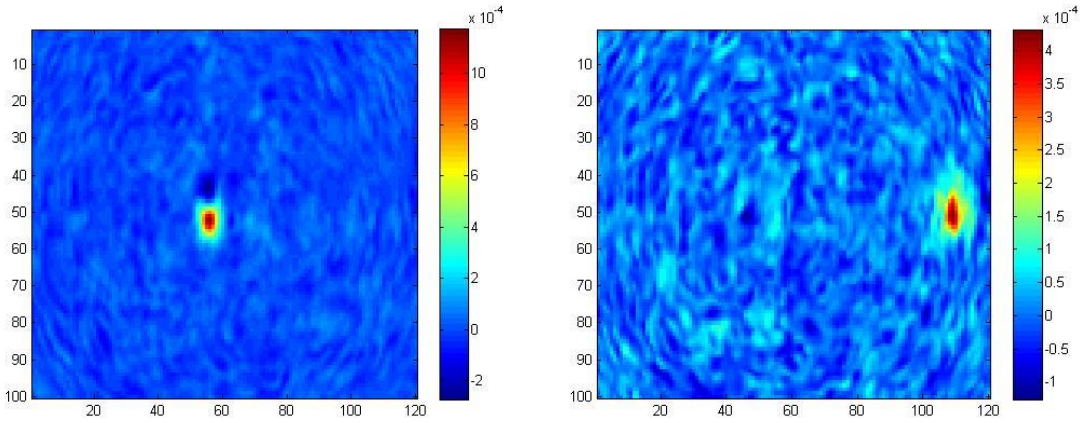

Figure 34 Reconstructed image in the experiment with the target in front of the array(a) and moved by 50 cm(b).

A metal sphere (10cm diameter) was shifted in front of the antenna array at 1m range out of

the antenna aperture in x direction. For the simulation was done the same using the point reflector, and considering the radiation pattern in one case and not considering in other.

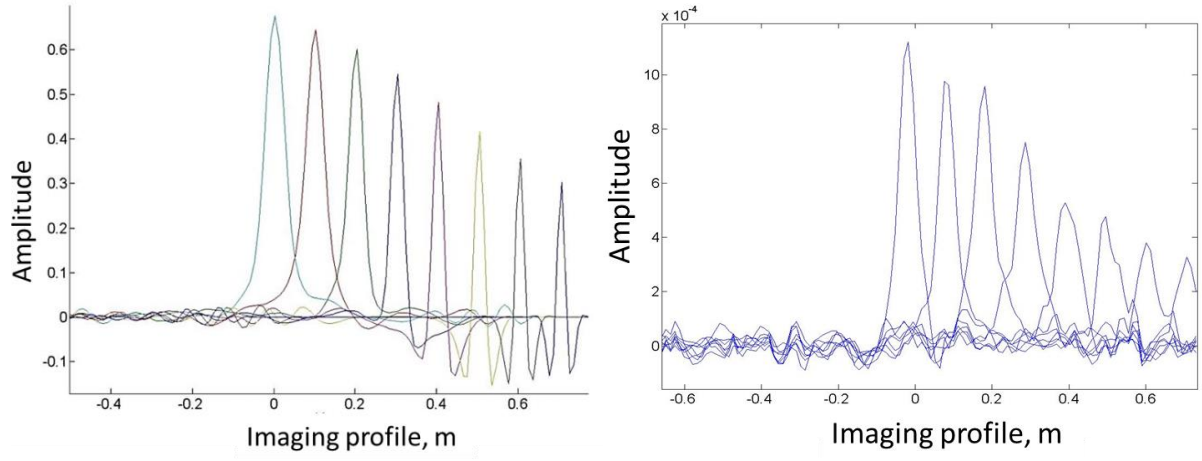

Figure 35 Signal amplitude in the simulation with included radiation pattern (a) and in experiment with metal sphere (b).

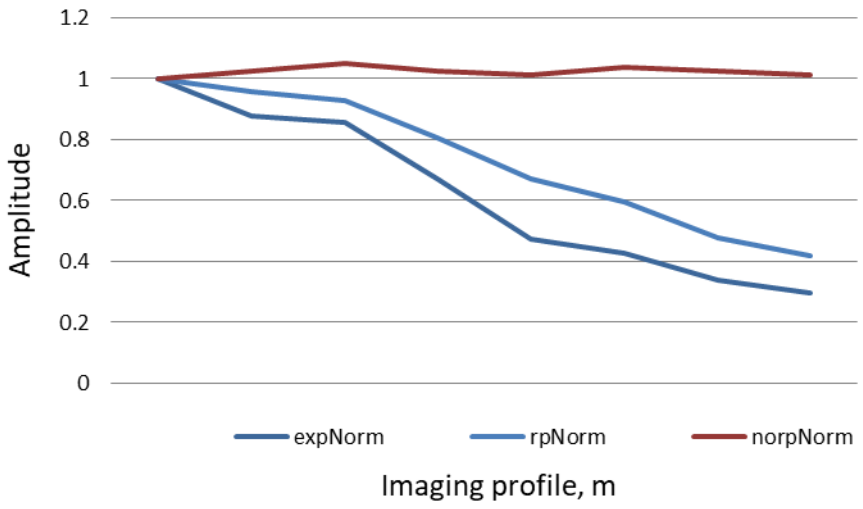

Figure 36 Comparison between experiment results and simulation with using radiation pattern and without.

As it can be observed from comparison in the Fig. 35 the numerical simulation corresponds to the real measurements with sparse array radar used in the study. Plots are normalized to the high value. Here are results of tracking the target that is moving away from the middle of the antenna array aperture. Considering the radiation pattern we can use proposed optimization method to find a new antenna layout for the radar system.

2.2.5 On the target distribution

The other thing to make the optimized array been warranted for different targets and been independent on the target position is using the random target distribution during the optimization. Using the targets with fixed position the algorithm will find the solution only for simulated problem. It means the new antenna layout, corresponded to founded minimum of the cost function, will not increase an imaging resolution for the targets in other position. It could be seen from the Fig. 36.

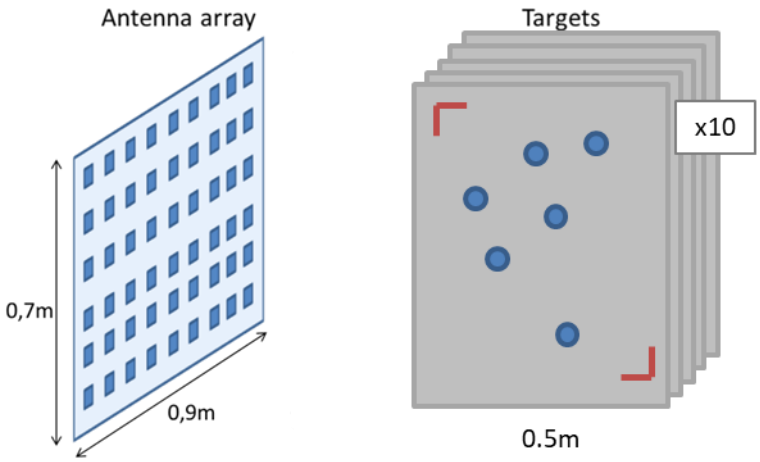

Figure 37 Set up for the simulation.

Here after 200 iterations of the optimization the targets positions were shifted to the new position and the algorithm lost the minimum value of the cost function starting to find a new one all over again.

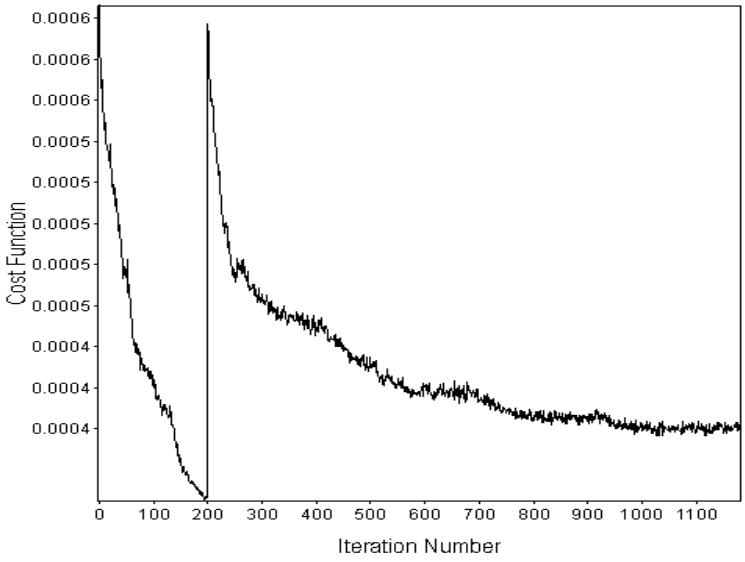

Figure 38 Cost function progress.

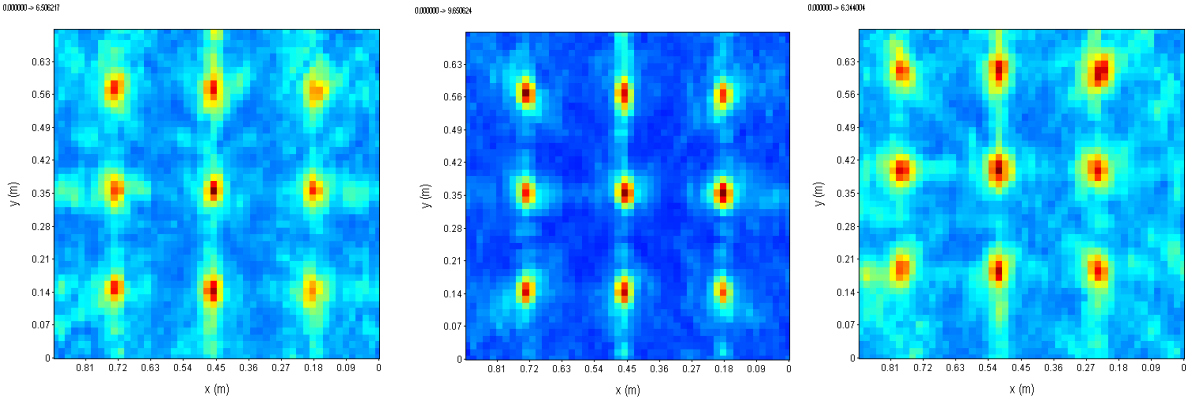

Figure 39 Reconstructed Image at with shifted targets .

To avoid this problem we used the random target distribution. Now each step of the optimization we use 10 packs of 6 targets with different position in each pack (Fig. 6) to accumulate the cost function and move to the next step:

$$S = \sum \frac{\left\| U(x,y,z)|_{x,y,z\notin\Omega} \right\|_{L2}}{\left\| U(x,y,z)|_{x,y,z\in\Omega} \right\|_{L0.5}} / Ntar \to min \tag{2.15}$$

The method optimizes the antenna pattern by changing the positions of receivers and transmitters.

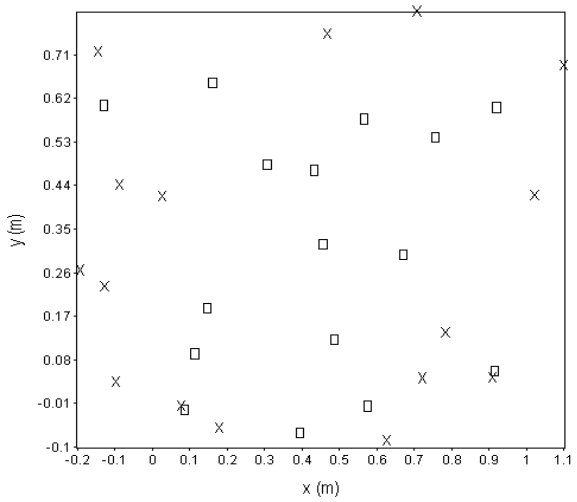

Figure 40 Optimized antenna pattern with optimization without accumulation.

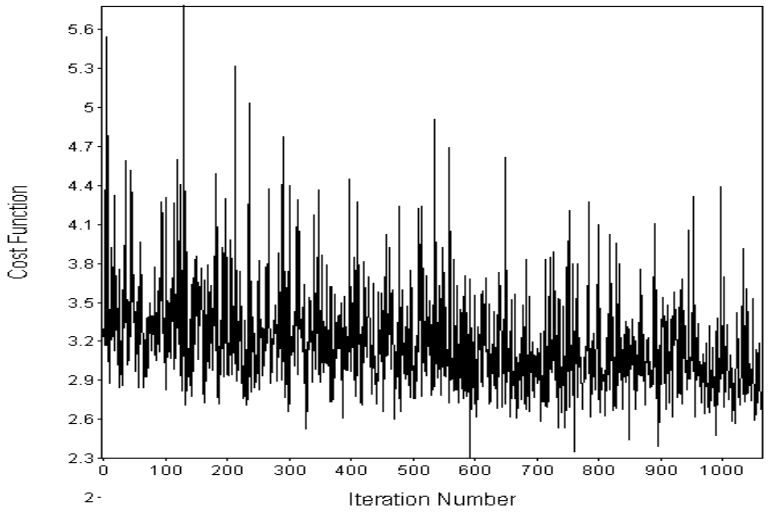

Figure 41 Cost function progress during the optimization.

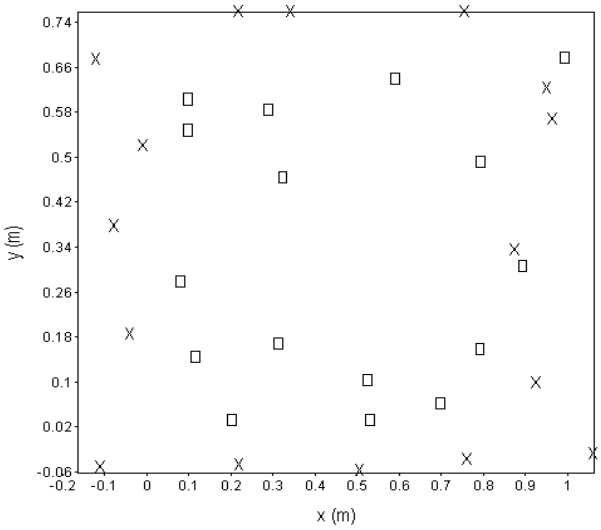

Figure 42 Optimized antenna pattern with accumulating optimization.

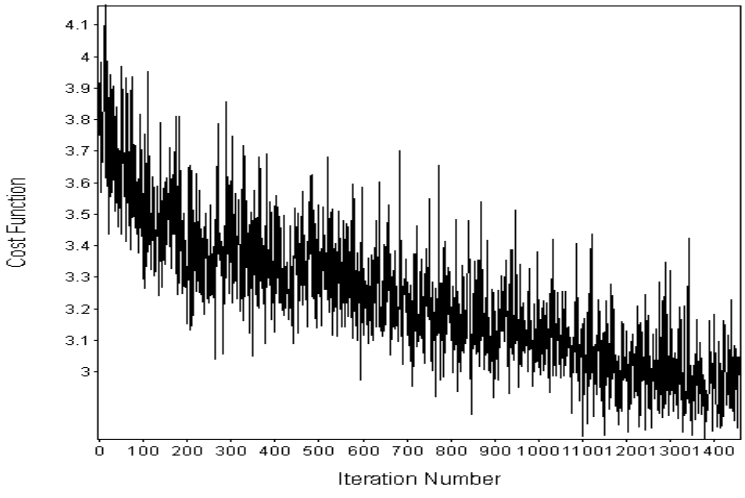

Figure 43 Cost function progress for 32 element array optimization for the optimization with accumulating.

This batching of 10 packs is necessary because without such accumulation the algorithm will stack on the same values of the cost function as shown.

Here presented the cost function progress during optimization of 32 elements antenna array. For the case of using batches the algorithm successfully found the minimum after 1300 iterations and the algorithm without such accumulation keeps oscillating around same values, demanding more time or being stacked at local minimum.

2.2.6 Numerical Calculation

We proposed a method of the array optimization and presented results of the optimization for a two-dimensional sparse array system. The algorithm of the optimization searches a minimum of the cost function, that is based on the relation of $L_2L_{0.5}$-norm of the reconstructed image, and uses random target distribution to make the final solution layout warranted for any position of the target in front of the radar. To increase the resolution of this radar system we used coordinates of the antennas in its sparse array as initial parameters for the optimization. At the end the algorithm has found a solution for the optimization in a form of the cost function minimum. The solution corresponds to the layout for the sparse array that could be tested experimentally.

There are results of the optimization of the 2D sparse array according to the simulation with batches of 6 targets in random positions. The total simulated area for optimization is a 1m side cube represented by 3D matrix the size of 50x50x50 points. For the initial parameters we use the positions of the actual antenna array elements. The wavelet has a hamming function form in frequency domain with bandwidth corresponds to the actual sparse array equipment (270MHz to 8GHz).

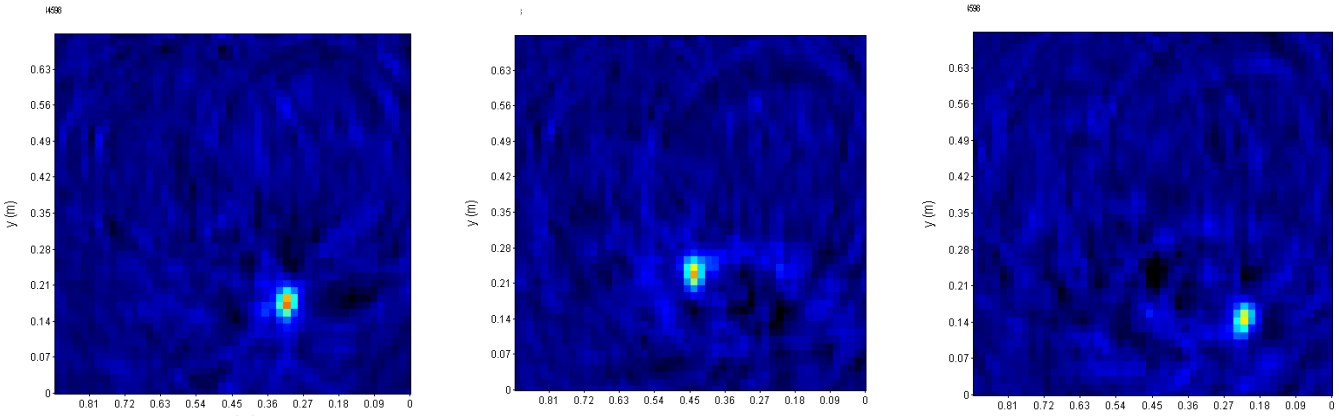

(a) 0.2m (b)0.35m (c)0.5m

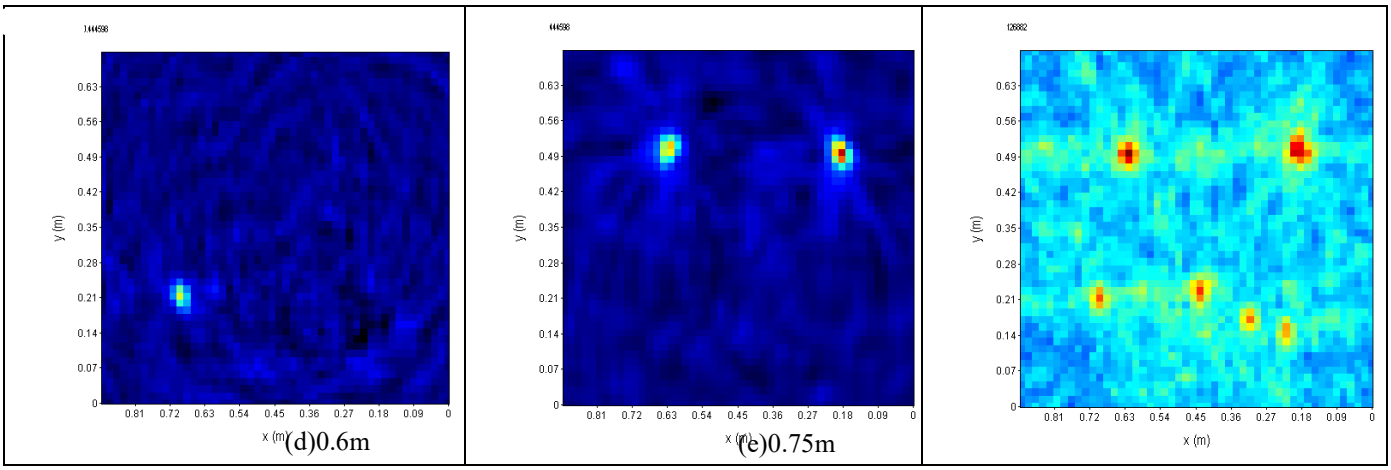

Figure 44 Slices of the 3D image of the targets at 0.2m(a), 0.35m(b), 0.5m(c), 0.65m(d) and 0.8m(e), imaged by optimized array.

In the Fig. could be seen the comparison between the optimized array after the simulation and the scaled array with initial parameters. For the border characteristics of the simulation we chose the 1.5 times larger zone to increase the total size of the antenna array and increase the aperture. In that way to make the comparison fair the initial array was also enlarged 1.5 times and for the targets we used 27 point-targets as shown in the figure.

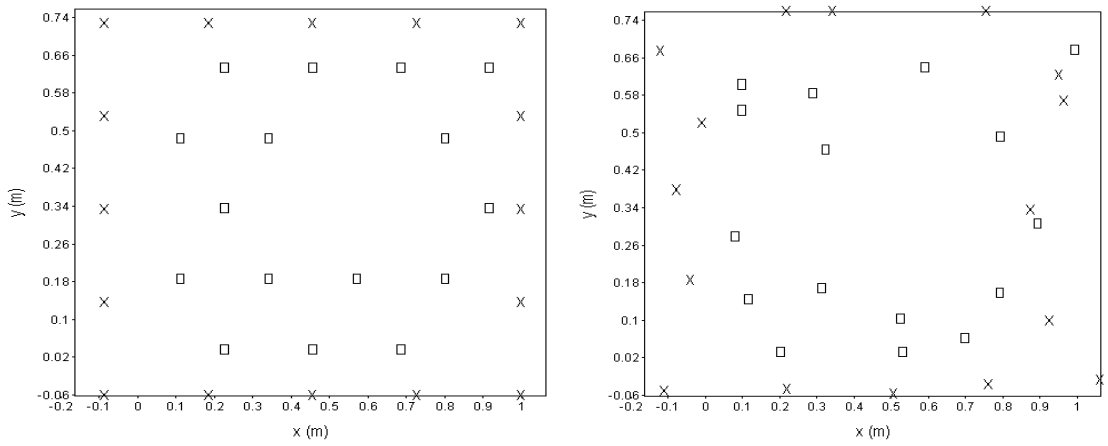

Figure 45 Configuration of the initial antenna layout(a) and optimized layout(b).

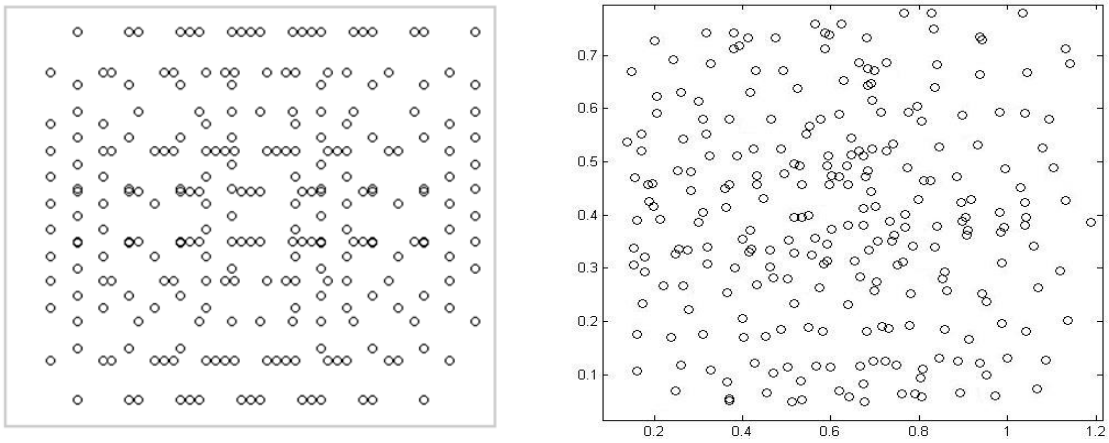

Figure 46 Distribution of the middle points for the initial antenna array layout and optimized antenna array.

Compare to the initial sparse array layout the new pattern gives more sparse middle point distribution as it was predicted. To look closer, in Figs.46-48 there is a comparison between this two antenna array pattern; here represented a several profiles taken as it is seen from the Fig.49.

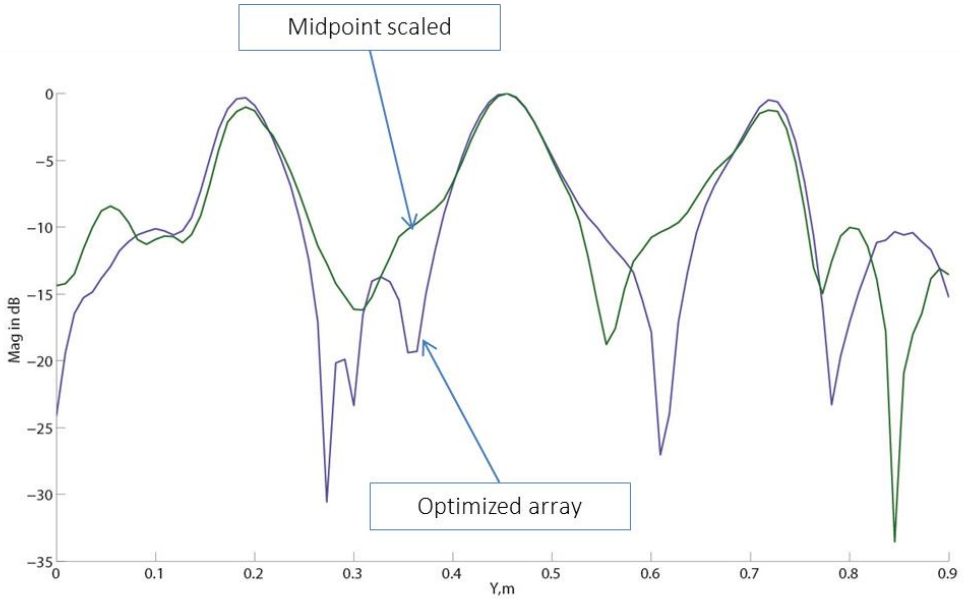

Figure 47 Comparison the optimized layout and initial one.

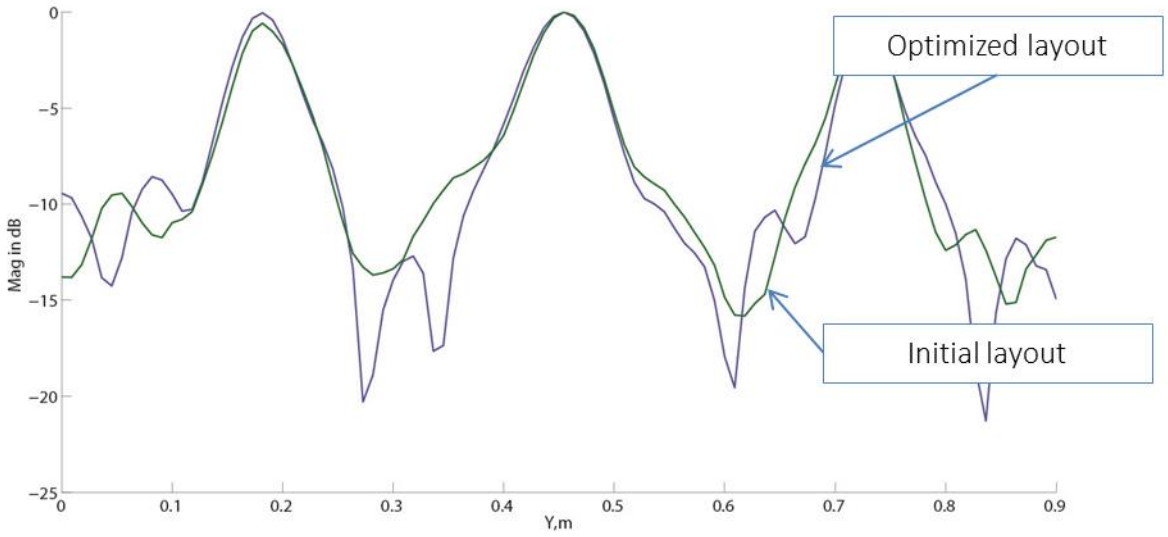

Figure 48 Comparison the optimized layout and initial one.

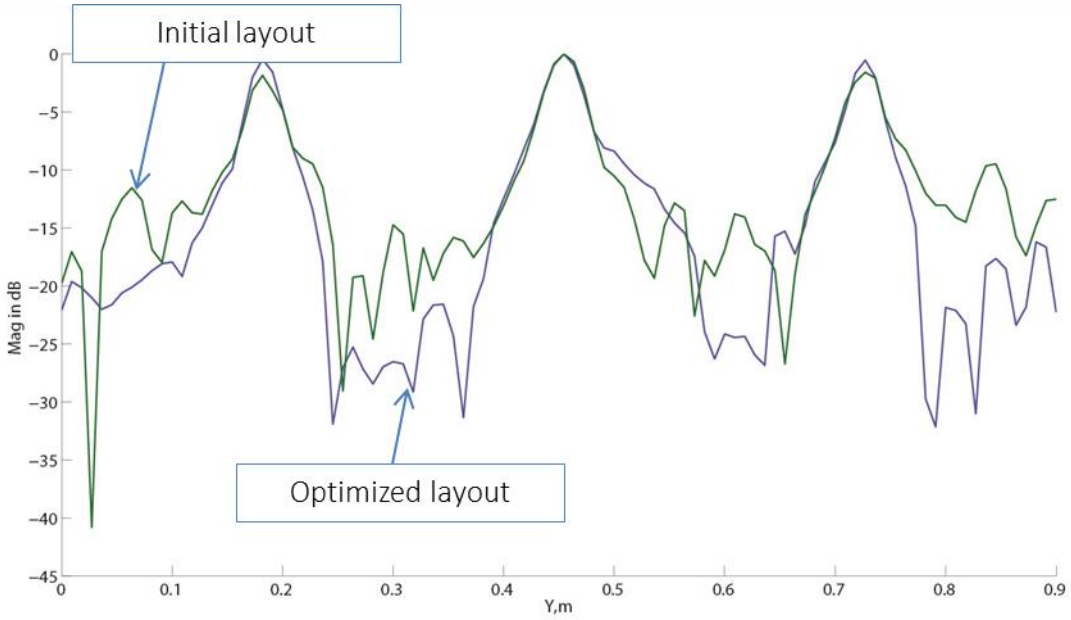

Figure 49 Comparison the optimized layout and initial one.

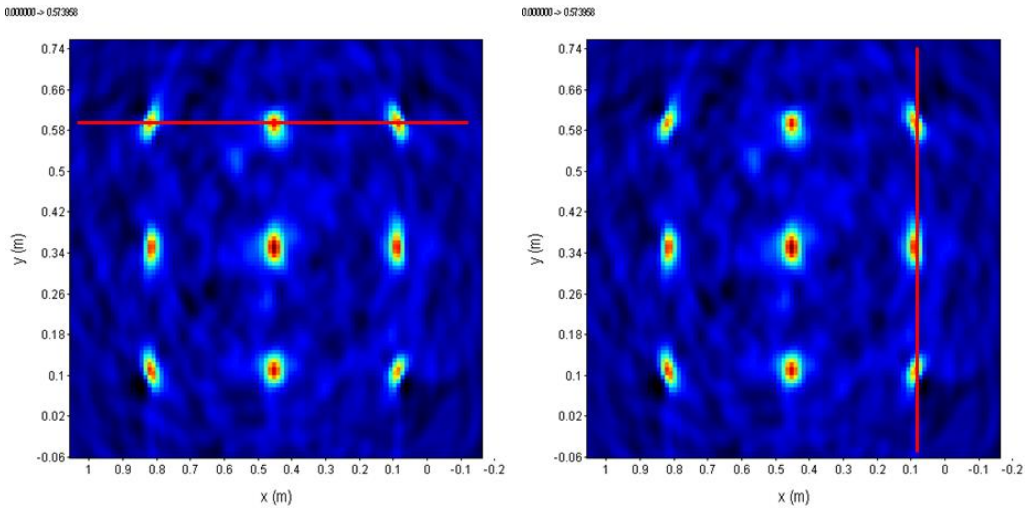

Figure 50 Slice of the imaged targets.

On the Fig there are slides of the 3D reconstructed image from the last iteration and the stacked image of 50 slides along the z direction from 0 to 1m (toward the face of the array). For the simulated problem the algorithm found a solution in a form of new antenna array layout.

2.2.7 Experiment with optimized antenna array

In order to validate the simulated model we carried out an experiment with the step frequency continues wave radar. To increase the resolution of this radar system we used coordinates of the antennas in its sparse array as initial parameters for the optimization. We also used the random target distribution in the optimization algorithm so the total solution layout will be warranted any position of the target.

Figure 51 Imaging of the object in front of the radar system.

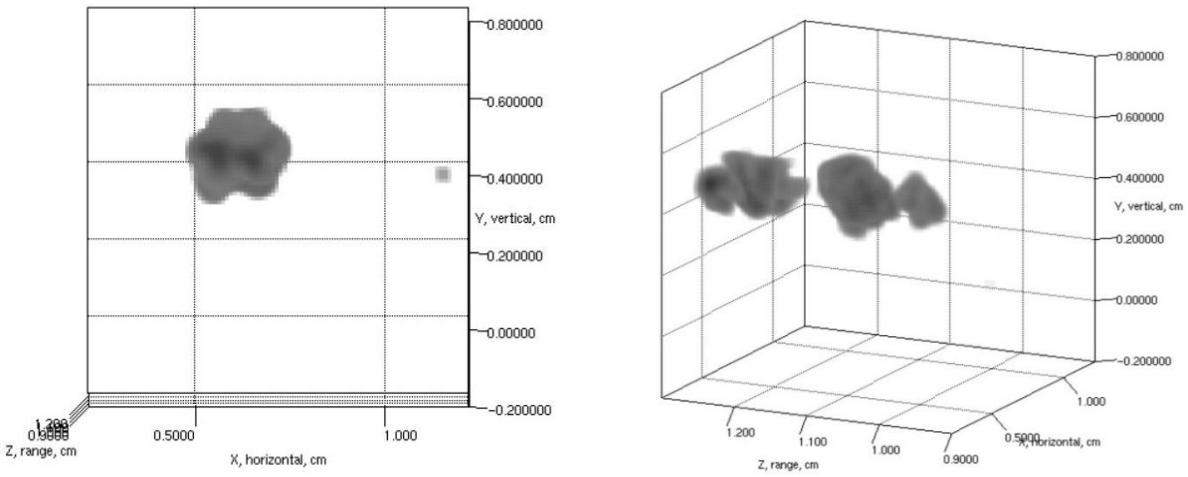

Figure 52 Reconstructed Image of the metallic star in 3D.

To observe the influence of radiation pattern on the near range imaging, we acquired the data with a few metal shaped forms, located at about 1m from the radar. Fig. shows the reconstructed images by the least square and Compressive Sampling Matching Pursuit methods with radiation pattern information. If the image was reconstructed without the radiation pattern information, some additional artifacts can be observed. The amount of the artifacts decreases with increasing the distance to the target object. It also strictly requires the accurately measured relative amplitude information for the different channels.

The proper calibration of the signal should be done for the system to avoid the kinds of artifacts that could occur as it shown in the Fig.51. This additional images of the metal star-shape target appears along the curve in range, repeating the wrong reference signal.

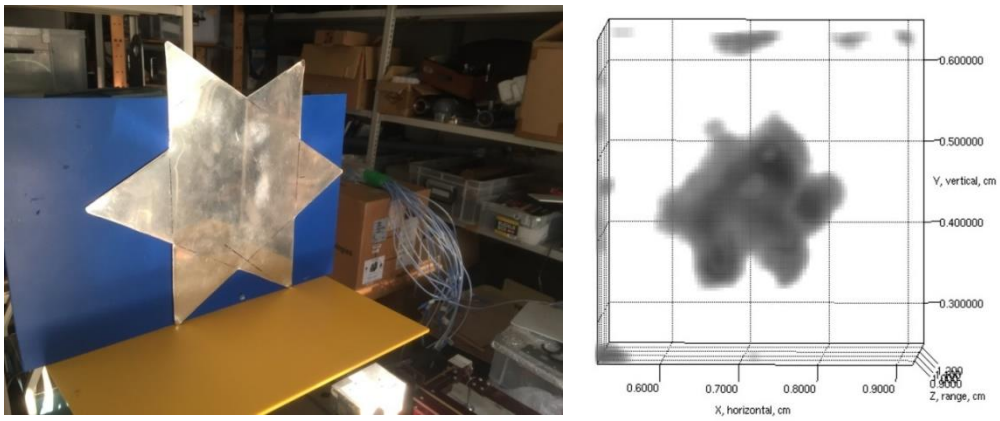

Figure 53 Reconstructed Image.

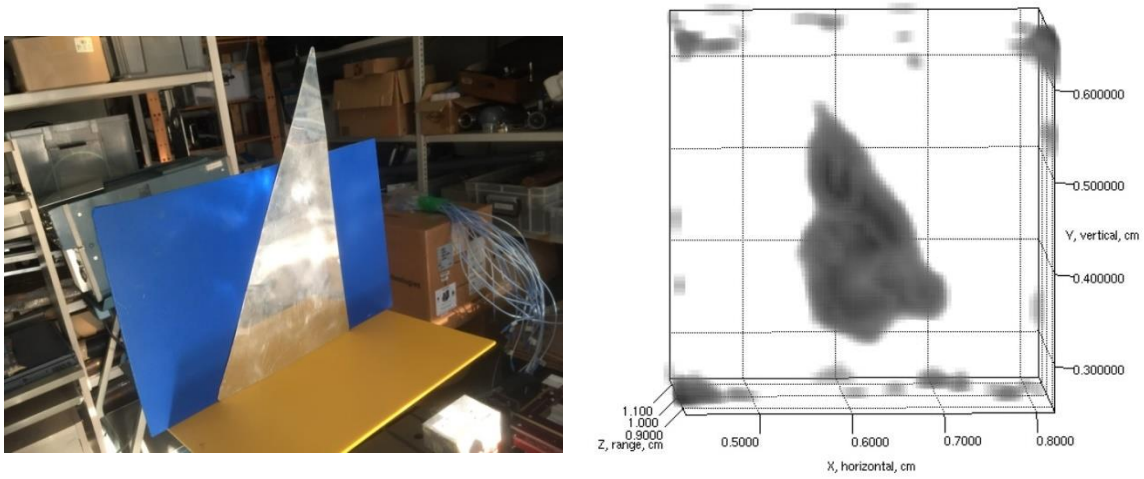

Figure 54 Reconstructed Image.

As it been represented in section 2.2.6, where I compared a performance of two antenna array patterns, the difference in the actual values of the imaged targets is not too big. 2-3dB difference will not bring the significant improvements in focusing abilities that could be catch by the eye. Furthermore, the manual manufacturing of the antenna array, small data errors and not perfect experiment environment conditions (that theoretically could be reach in anechoic chamber though) unfortunately makes comparison irrelevant. On the other hand, during the optimization the boundary conditions were set in a way to make the antenna pattern 1.5 times larger, that could be more useful in a term of radar applications.

Chapter 3 High resolution 3D Imaging with Millimeter Wave Radar

Many research institutions as well as a companies have developed [22] GB-SAR system and successfully used in wide application field such as monitoring of deformations. Due to high frequency band GB-SAR could achieve a very high resolution allowed to detecting the small changes for example on a runway pavement in an airport [23]. Most of ground radar systems use linear track to achieve synthetic aperture, which limits the scope of observation. The other point of consideration is that the rail using for SAR could be quite large depends on the purpose of the radar, and the whole system could demand for additional supply and a special treatment. A small millimeter wave radar could be used with higher mobility placed on a moving vehicle or a human body. The free movement of a system could be used instead of a rail to get the desirable resolution, and the multiple number of antennas could be used to reconstruct the 3 dimensional image.

Chapter 3 introduces the millimeter wave system, using multichannel migration, used to track reconstruct a 3D image of the target.

3.1 Imaging with millimeter wave radar

3.2.1 Continues wave radar

The principal of the Continues Wave consist in the fact that radar is transmitting a high-frequency signal continuously, and the reflected signal is received and processed permanently. However it allows the system to face the problem of a feedback connection when the emitted energy directly goes to receiver. It could be prevented by the spatial separation of the transmitting antenna and the receiving antenna, and the frequency dependent separation by the Doppler-frequency during the measurement of speeds.

As long as a CW radar has no range- or time-discrimination capability the time resolution of a CW radar is equivalent to an infinity long pulse length [25]. But if frequency modulation (FM) is applied to transmit signal, then the range resolution could become possible. Simple continuous wave radar devices without FM cannot determine target range because it lacks the timing mark necessary to allow the system to time accurately the transmit and receive cycle and to convert this into range. Such a time reference for measuring the distance of stationary objects, but can be generated using of frequency modulation of the transmitted signal.

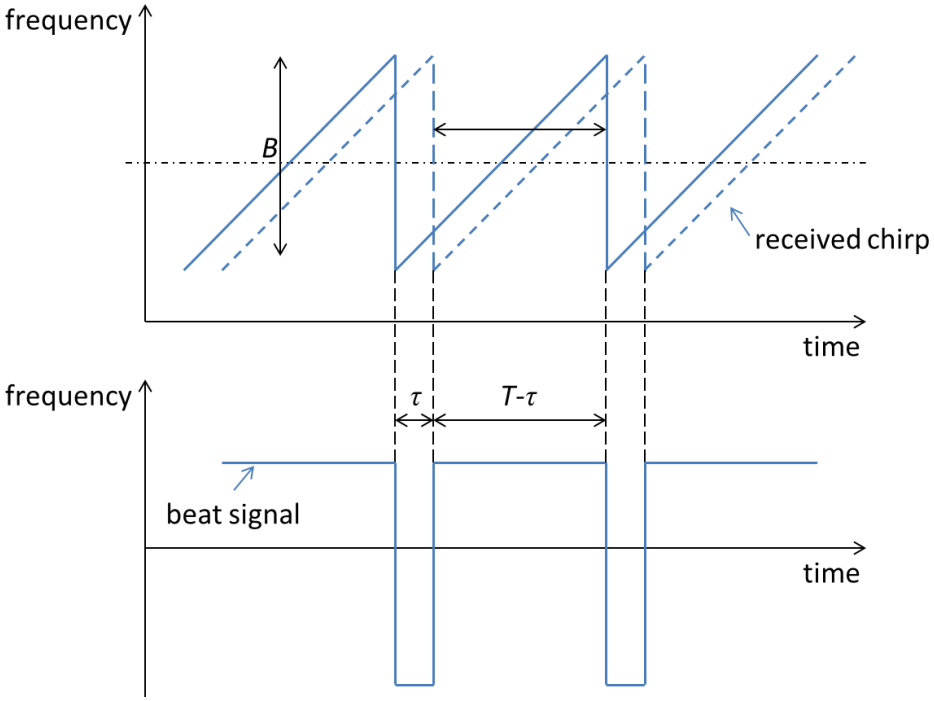

Figure 55 The signal delay in the FMCW radar.

Here a signal is transmitted, which increases or decreases in the frequency periodically. When an echo signal is received, that change of frequency gets a delay τ (by runtime shift) like the pulse radar technique. In pulse radar, however, the runtime must be measured directly. In frequency modulated continues wave radar are measured the differences in phase or frequency between the actually transmitted and the received signal.

The signal that we observe on the oscilloscope is multiplication of transmitted Linear Frequency Modulated (LFM) signal and received the sum of LFM signals with some delays. Let us suppose that signal frequency sweeps upward, linearly, over one sweep repetition interval T. Using a complex number representation [27], the transmitted signal S_{TX} with unity amplitude can be expressed as the real part of:

$$S_{TX}(t) = \sum_{n=-\infty}^{\infty} S_{TX}(t - nT) \tag{3.1}$$

where $S_{TX}(t)$ is the linear chirp pulse

$$S_{TX}(t) = \text{rect}\left(\frac{t}{T}\right) exp\left[j2\pi(f_c t + \frac{1}{2}\alpha t^2)\right] \tag{3.2}$$

and

$$S_{TX}(t) = \text{rect}\left(\frac{t}{T}\right) exp[j\varphi_{TX}(t)] \tag{3.3}$$

Here t represents the time variable, $j = \sqrt{-1}$ is imaginary unit, f_c is the central frequency of the chirps and α is the frequency sweep rate. *Rect* is a rectangular function represented by:

$$rect(x) = \begin{cases} 1, \ if \ |x| < \frac{1}{2} \\ \frac{1}{2}, \ if \ |x| = \frac{1}{2} \\ 0, \ if \ |x| > \frac{1}{2} \end{cases} \tag{3.4}$$

There is a fixed relationship between the phase in one sweep and the next, it comes from a coherency of the FMCW, which allows to use it in Doppler processing [..] to determine information on the velocity of detected targets. In this case we assume that the transmit signal is periodic, and phase-coherent from one sweep to the next. Since the instantaneous frequency $f_{TX}(t)$ is a derivative of the phase, we have

$$f_{TX}(t) = \frac{1}{2\pi}\frac{d\varphi_{TX}}{dt} = f_c + \alpha t \tag{3.5}$$

What can be seen from the frequency excursion over one sweep repetition interval is *B* the chirp bandwidth. The instantaneous frequency of the transmit signal is plotted in Fig.54 as the solid line.

3.2.2 Radar configuration

Fig. 55 illustrates the schematic of the MMW FMCW Radar. radar consists of a sweeping source connected to a frequency multiplier which are used for transmitting and Local Oscillator (LO) generation simultaneously. The transmitted signal is linearly frequency modulated. The frequency swept signals returned from the object are delayed copies of the transmitted signal. The delay is given by the round trip propagation time to the object and back.

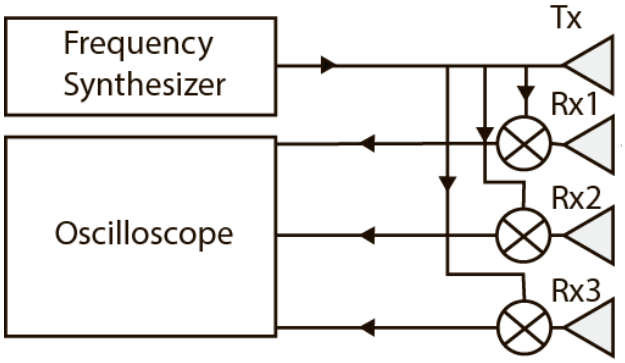

Figure 56 Radar simplified functional diagram.

The transmitted signal is generated by a voltage controlled oscillator (VCO) operating between 12GHz and 12.5GHz. It drives a frequency multiplier which has a multiplication factor of 6. The usable output frequency range of the multiplier stage lies within 72 GHz and 75 GHz.

The transmitted signal is emitted by a linear polarized horn antenna. For transmitter and receiver separate antennas are used in order to avoid the effects of the return loss.

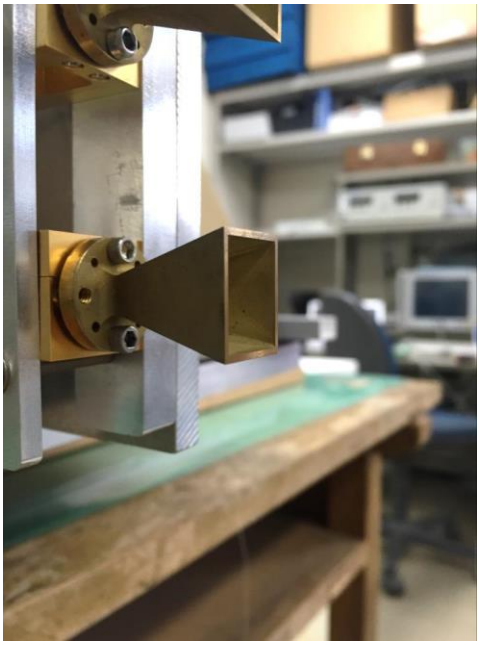

Figure 57 The horn antenna.

Another reason for separation is that we consider to have three receiving channels. These three channels can be used for interferometric imaging approaches.

The received signal is amplified by a low noise amplifier before downconverting to IF. The IF signal is a low frequency low pass signal (0 Hz to 300 kHz). The upper frequency limit is only depending on the maximum expected range.

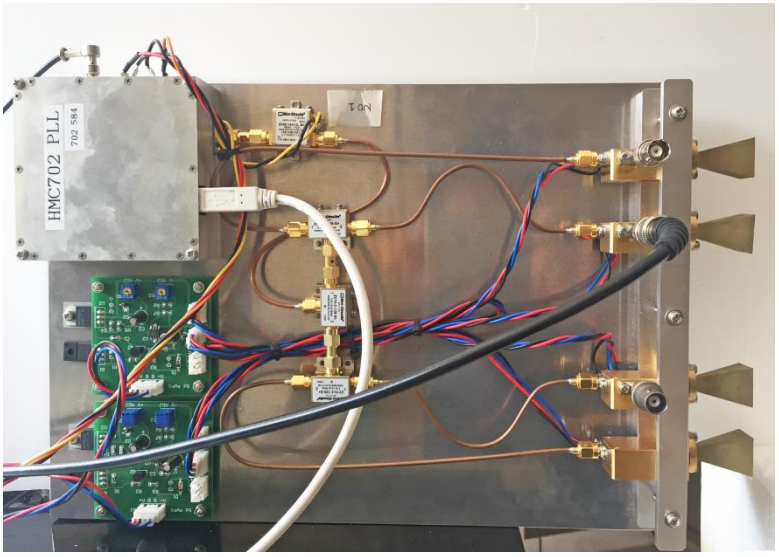

Figure 58 The millimeter wave radar used in the study.

The radar system used in this study has one transmitting and three receiving rectangular horn antennas at variable positions. The distances between transmitting and receiving antennas are 4.7cm, 12.2cm and 16.6 cm. The system periodically sweeps from 12.5 GHz to 13 GHz and

transmitted signals, that multiplied six times, have frequency ranging from 75 GHz to 78 GHz with 3 GHz bandwidth. The sweeping time is 3 ms.

It also should be taken into account that frequency resolution for that system, which is follow from:

$$\Delta f = \frac{1}{T_{chirp}} \tag{3.6}$$

converting to time delay:

$$\Delta t = \frac{\Delta f}{\partial f / \partial t} \tag{3.7}$$

And we get 0.03ms calculating to total distance (two directions) $c * \Delta t$ 0.1m. That is give us the theoretical range-resolution for 3 GHz bandwidth is about 0.5 cm.

3.2.3 Radiation pattern

Trying to reach the high resolution in 3-dimensional imaging we faced the problem of obtaining high resolution in vertical axis (that one where antennas are laying). The azimuth resolution can be reach by high numbers of the data acquisition during the scanning for SAR, but for vertical axis we have only 3 signals received by each step of scan.

There are 3 major ways to achieve better resolution: increasing distance between antennas, increasing of the beamwidth of antenna pattern, increasing number of elements. Let us consider the antenna pattern in our radar system.

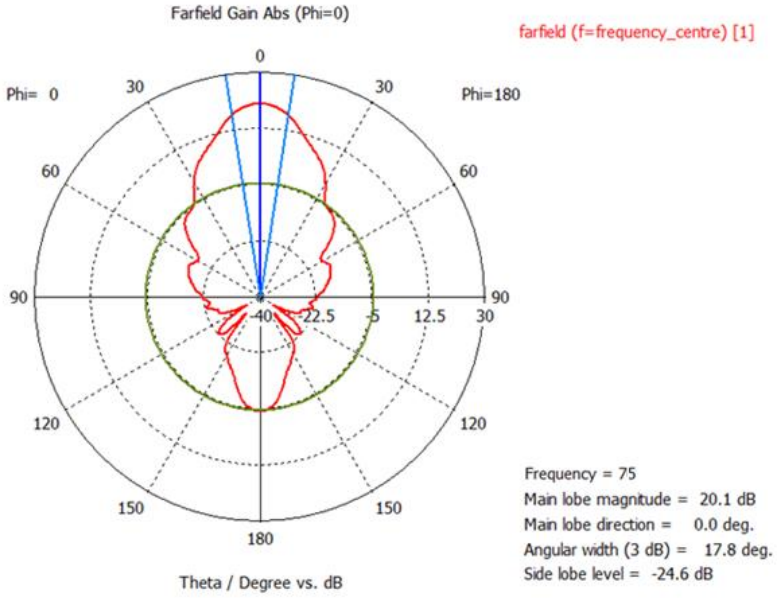

Figure 59 Radiation pattern of the horn antenna.

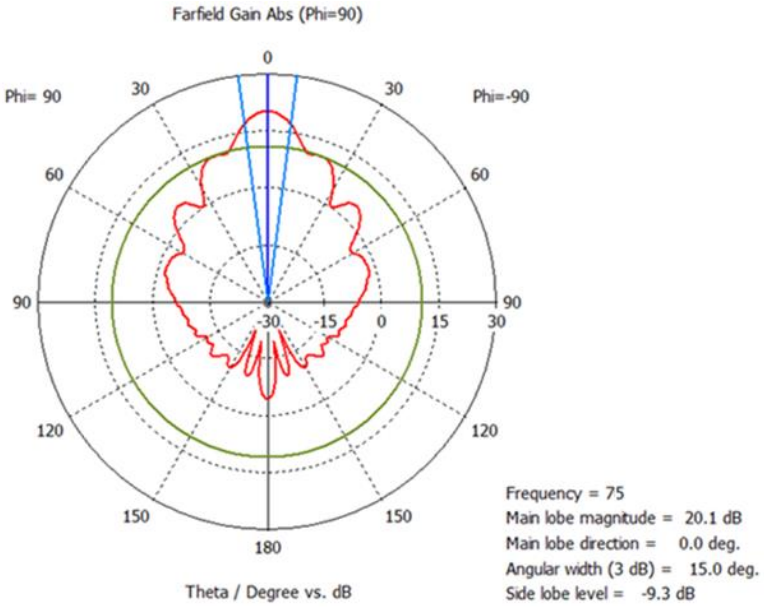

Figure 60 Radiation pattern of the horn antenna.

Figs. 58-59 represent a radiation pattern of the horn antenna used in the study that was calculated in CST Microwave Studio in the Finite-Difference Time-Domain (FDTD) transient solver. The antenna has a very narrow beam, which is typical for that high gain horn type antennas. The main beam width of the antenna is 17.8 degrees in H-plane and 15 degrees in E-plane, and the antenna gain at simulated frequency is 20dBi.

To compare the simulation results of the calculated antenna and check the performance of the one receiver measurement I carried out an experiment.

As first proof-of-concept measurement, a 3 channel prototype of the system described in section 3.2.1 has been used to make a sequence of one channel measurements of a static scenery. Radar was placed at static position and the 10cm metal sphere, used as a target, have been moved in an azimuth direction for a few data sets.

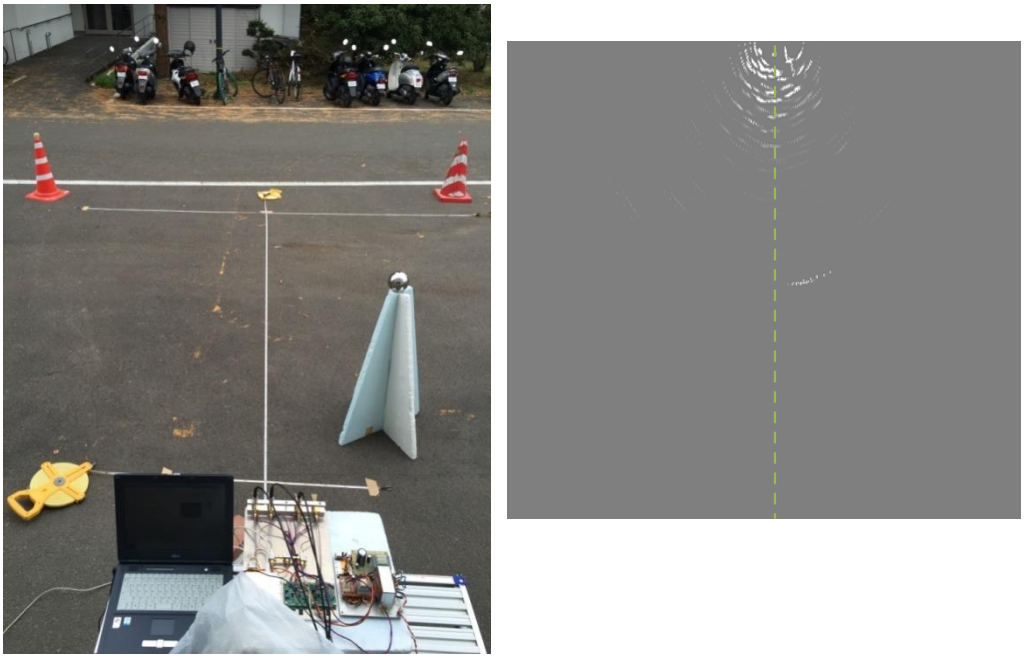

Figure 61 Experiment set up and reconstructed image.

To obtain a reconstructed image, a back projection algorithm and a caustic finding algorithm [28] have been used. A caustic finding algorithm worked much better for the one shot experiment as it could be seen from Figs.61-62.

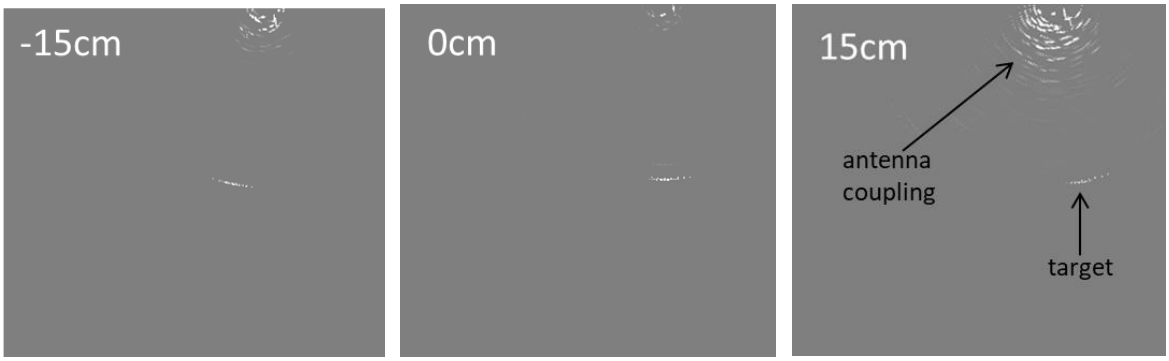

Figure 62 Reconstructed image using caustic finding algorithm.

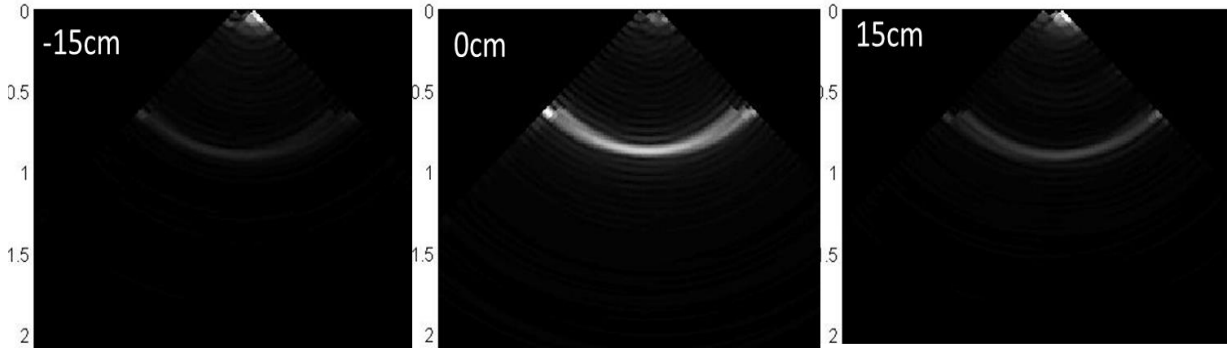

Figure 63 Reconstructed image using back projection algorithm.

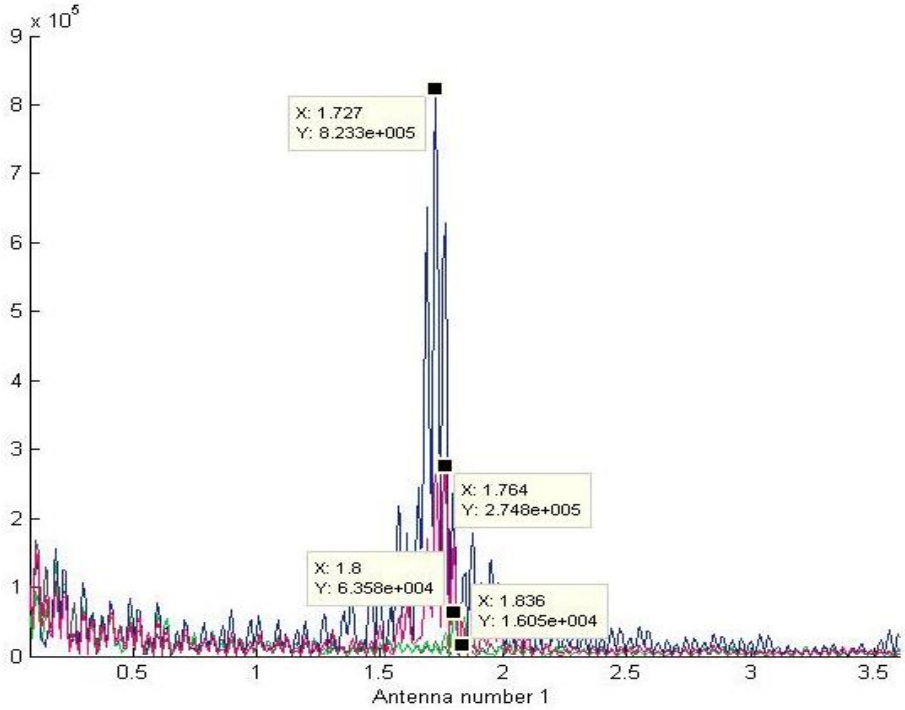

Figure 64 Energy with distance in absolute values.

Now we only consider in vertical axis so let us consider this aspect. The main lobe width at 75 Ghz is 17.8 deg. with side lobe level -24.6 dB. It could be observed from Fig.63, that is representing the reflection from the target at different positions. The object is poorly recognizable at 40 cm from central position, a capacity decreases at -17dB from the value at central position of the system.

3.2.4 Signal processing

A linear scanning as well as the type of free movement is used to collect the signals for the SAR processing. Fig. 64 represents millimeter wave radar used in imaging of target.

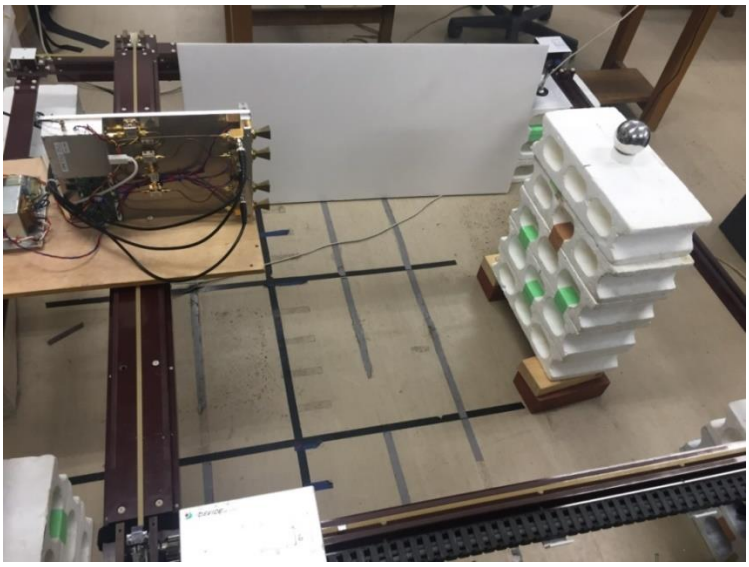

Figure 65 Millimeter wave radar at object recognition.

Obtaining the raw signal from the oscilloscope we making the background substraction witch could be done by averaging the noise. Fig. 66 represent an example of the signal during one sweep. Here it can be seen the mixed signal of the LO signal and received in time domain (showed by green colour) and.

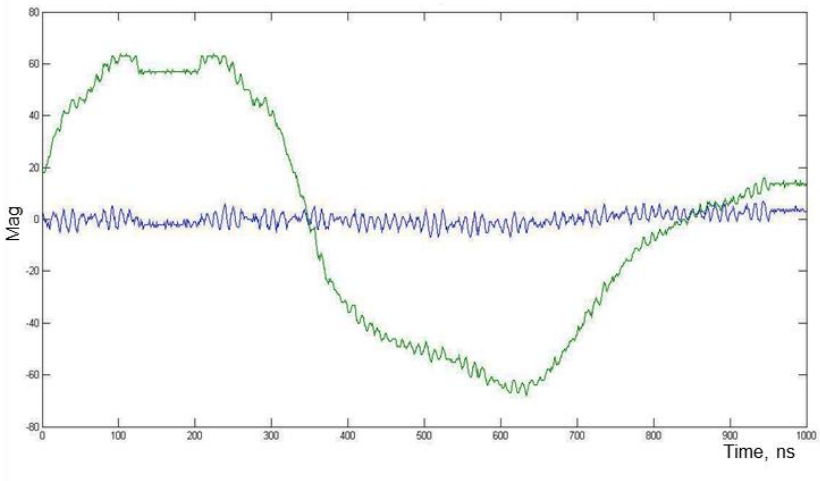

Figure 66 Raw data from oscilloscope.

Subtraction of the average background is done by only mean value, which is quite enough, and depends on the data aquistion could be the only way to reduce low frequency noise.

After that we apply a Hilbert transform and time delay compensation, which can should be done due to the specify of the radar configuration.

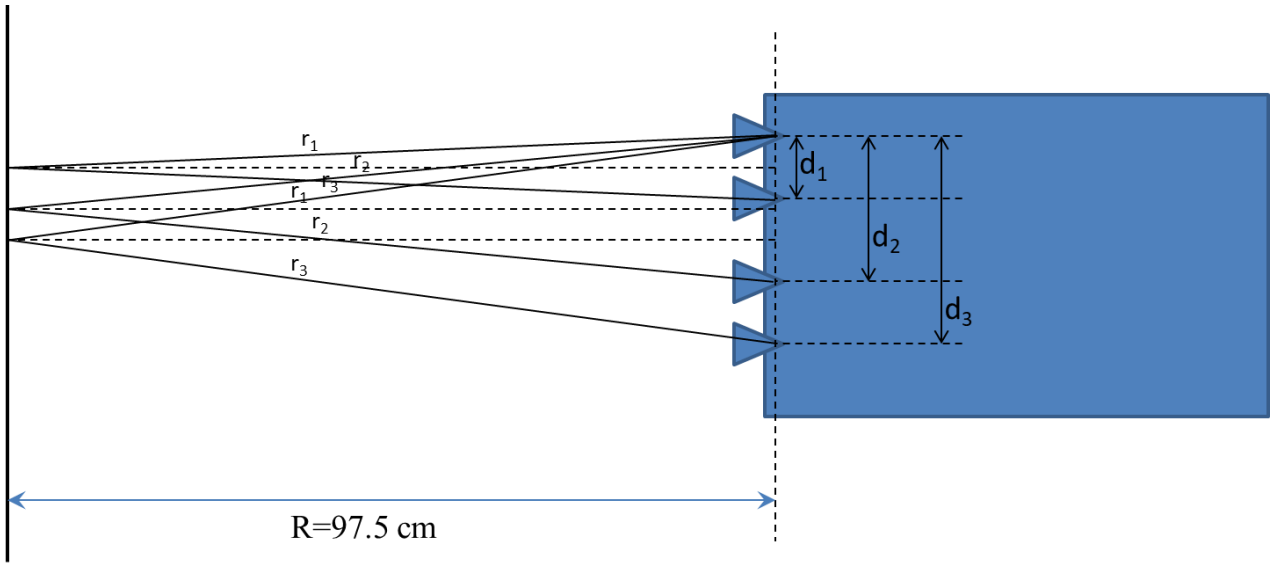

Figure 67 Time delay calculation.

Placed at the different distance from the transmitter three receivers have different travel delay to the target area, obtaining separate images that could be combine in one 3D image . The possible resolution of such method, as well as the ways of obtaining the azimuth resolution and applications should be discussed.

Time delay shift for each antenna is given by

$$\Delta T_i = \frac{\Delta X_i}{c} = \frac{2r_i - c \cdot t_i}{c} \tag{3.7}$$

where, t_i is measured time delay, and

$$r_i = \sqrt{R^2 + \left(\frac{d_i}{2}\right)^2} \tag{3.8}$$

For the actual millimeter wave system, time delays for each receiving antennas been calculated during the experiment with metal wall.

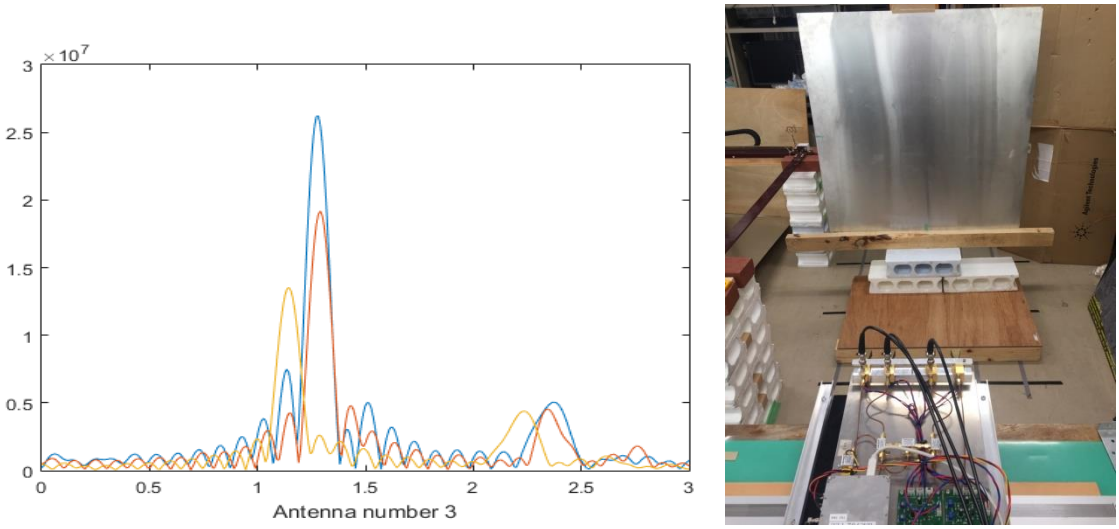

Figure 68 Time delay calculation

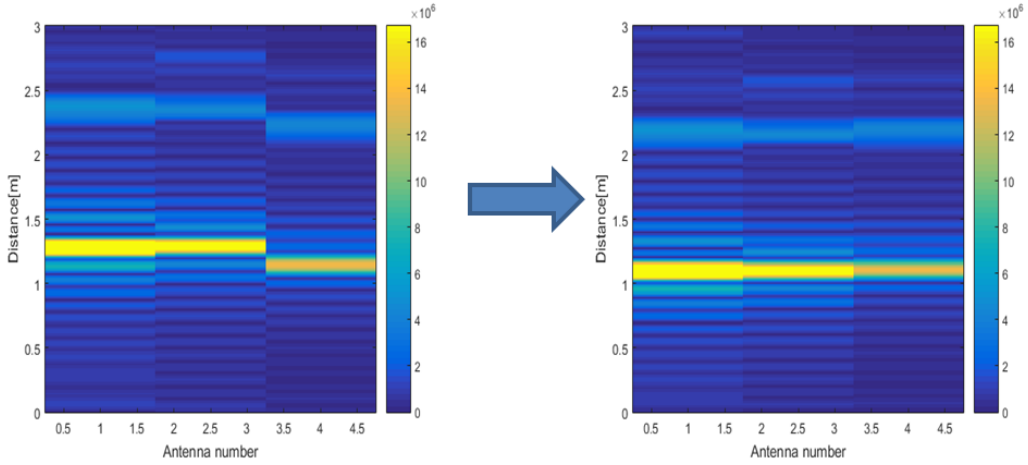

Figure 69 Time delay calculation.

After that the back projection algorithm is used to reconstruct the image. Fig. 69 graphicaly represent the linear scanning by the radar and the way of calculating of the signal delay for particular problem.

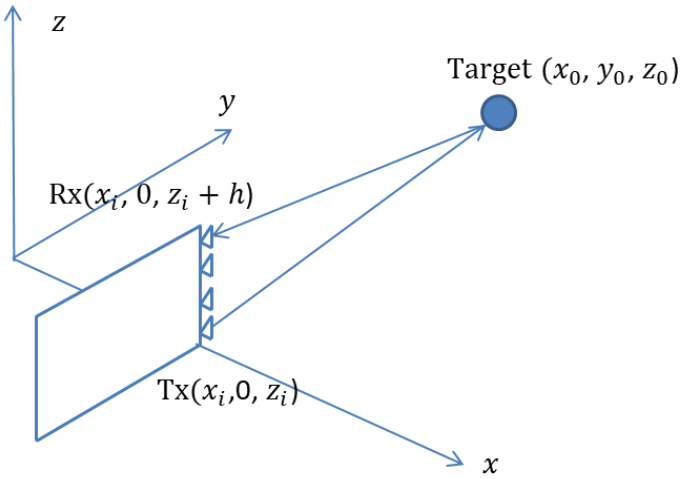

Figure 70 Delay calculation

Algorithm of back projection can be described by:

$$U(x_0, y_0, z_0) = \sum_i^n d_i(\tau_i)\, e^{j2\pi f \tau_i} \tag{3.4}$$

And the time delay calculated as

$$\tau_i = \frac{\sqrt{(x_0 - x_i)^2 + {y_0}^2 + (z_0 - z_i)^2}}{c} + \frac{\sqrt{(x_0 - x_i)^2 + {y_0}^2 + (z_0 - z_i + h)^2}}{c} \tag{3.6}$$

Make it to the point that (3.6) describes the time delay calculation for the linear scan. After back projection we looking for the overlap of the reconstructed imaging picking up the high values.

3.3 3D imaging with millimeter wave radar

3.3.1 3D imaging with linear scan

Based on the basic Fourier analysis, the spatial resolutions in the resulting 2D reflectivity images are determined by the extent of the data support region in the spatial frequency domain. Hence, they depend on the frequency bandwidth, the center frequency and the extent of the synthetic aperture. Besides, the traditional resolution formulas are usually defined according to a separable 2D coordinate system assuming that the support region is nearly in rectangular shape. These formulas, however, lose their validity for wide-angle data collections in which the range and cross-range resolutions are not essentially independent. In that case, the image resolutions should be deduced by approximations. One simple approach for predicting these resolutions is given in [31] that is based on the numerical calculation of the point spread function.

The imaging of several objects was done with linear scanning.

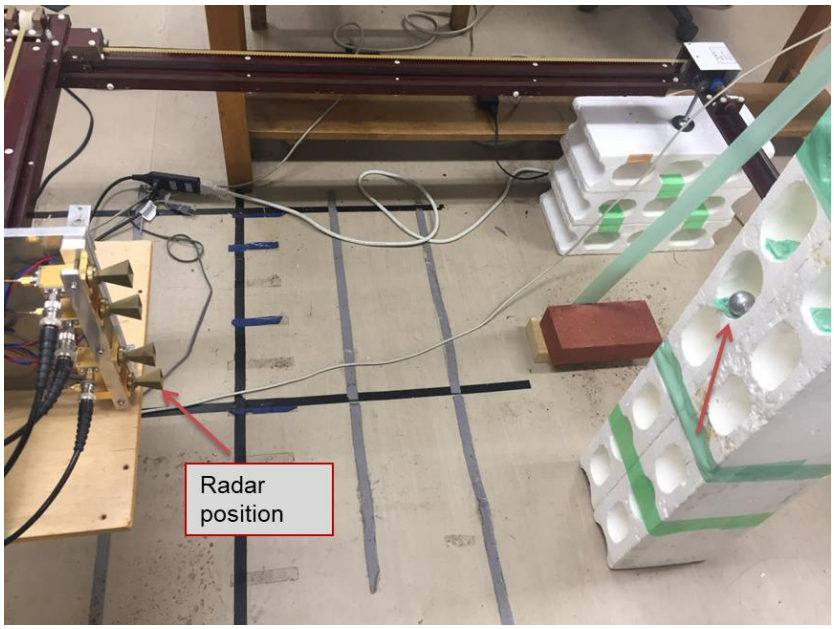

Figure 71 experiment set up.

Table 4.1 Parameter settings for the experiment

Radar bandwidth	3GHz (72GHz…75GHz)
Sweep time	3ms
Samples/sweep	800
Radar position height (by Tx)	0.53m
Aperture length	0.4m
SAR step	1.5mm
Target	Metal sphere 7.5cm diameter
Target position range	0.58m
Target position height	0.65m

Following section 3.2.4 imaging was done and results represented in Fig.71-76.

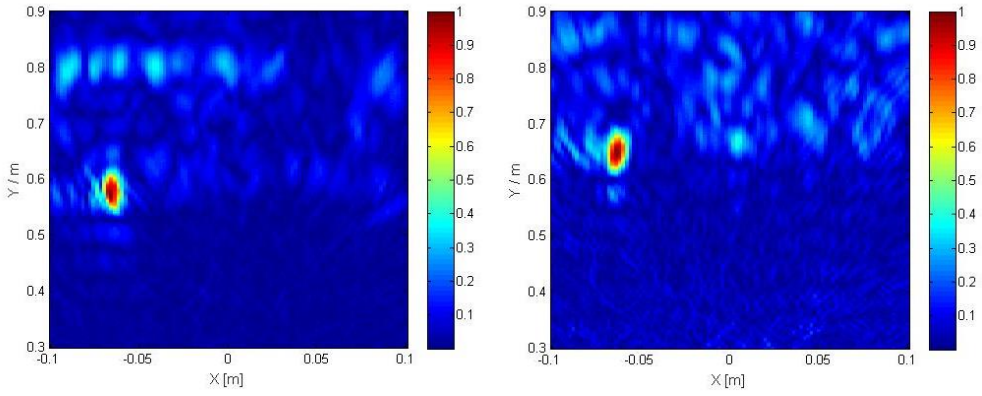

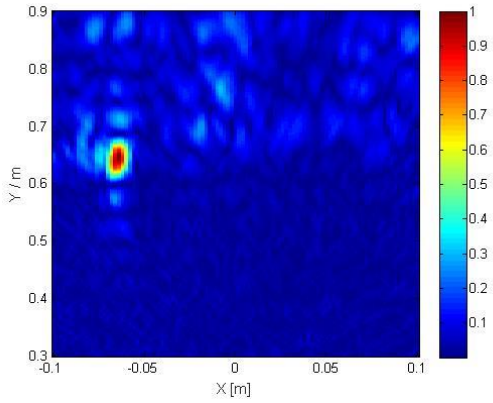

Figure 72 Reconstructed Image for each channel in 2D.

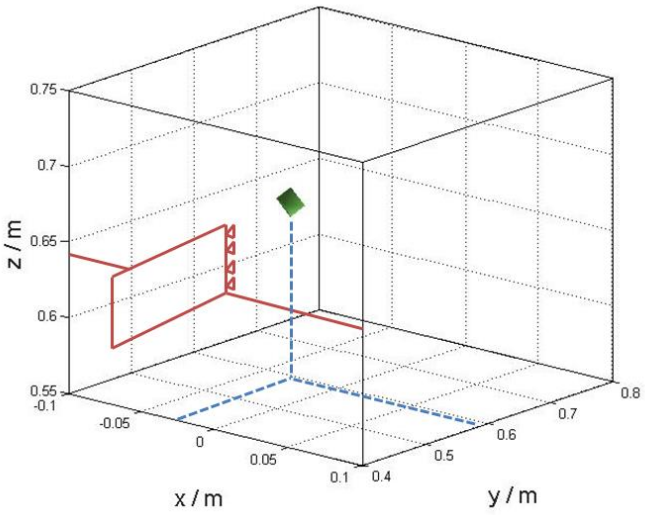

Figure 73 3D image from all channels.

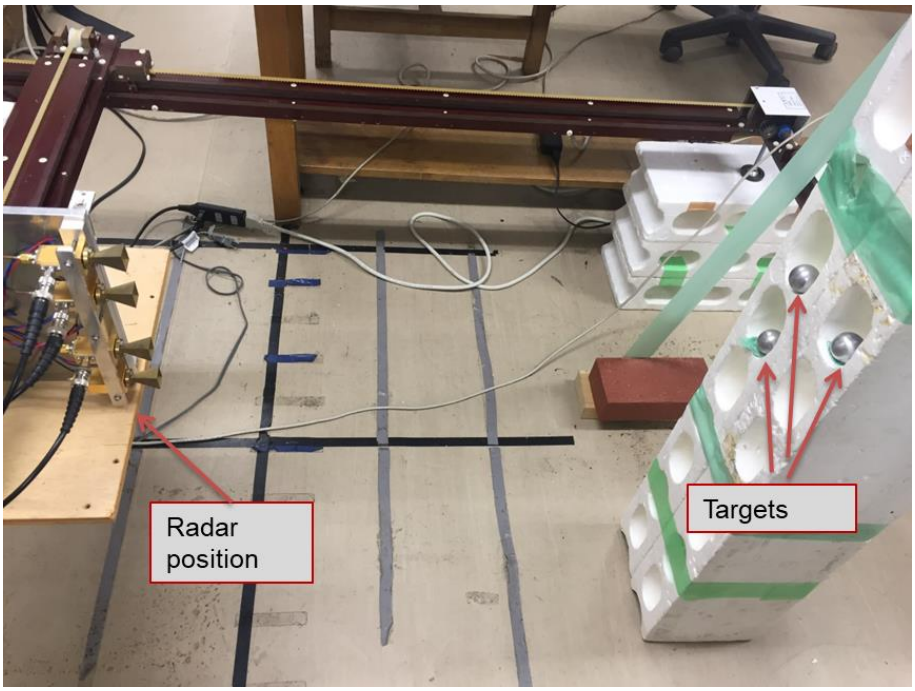

Figure 74 experiment set up.

Table 4.1 Parameter settings for the experiment

Radar position height (by Tx)	0.53m
Aperture length	0.4m
SAR step	1.5mm
Target	Three metal spheres 7.5cm diameter
Target position range	0.63m
Target position height	0.71(for two) and 0.57m

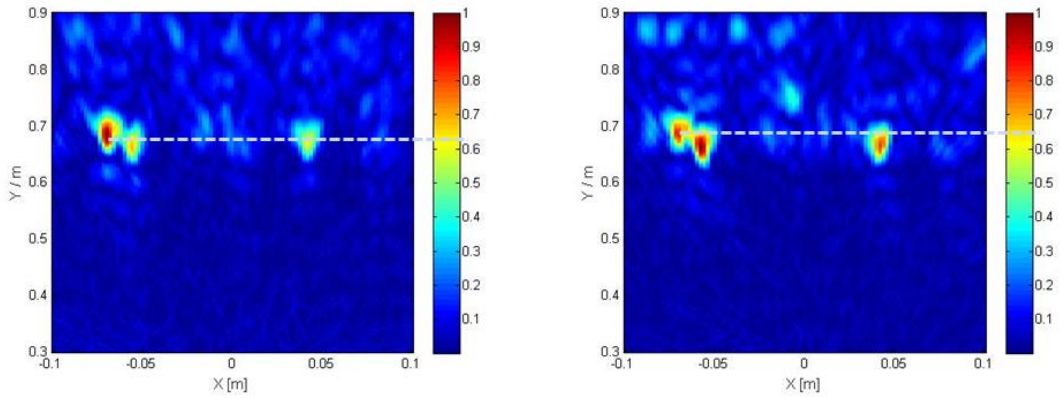

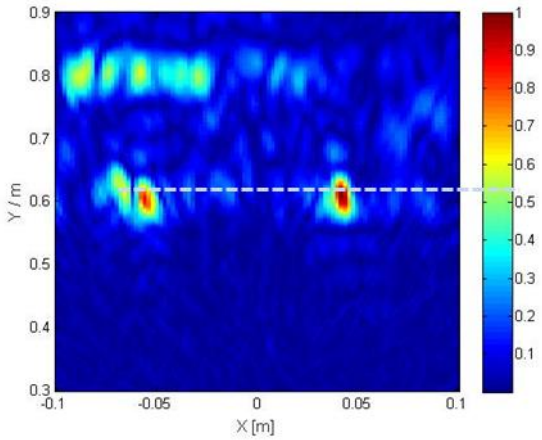

Figure 75 Reconstructed Image for each channel in 2D.

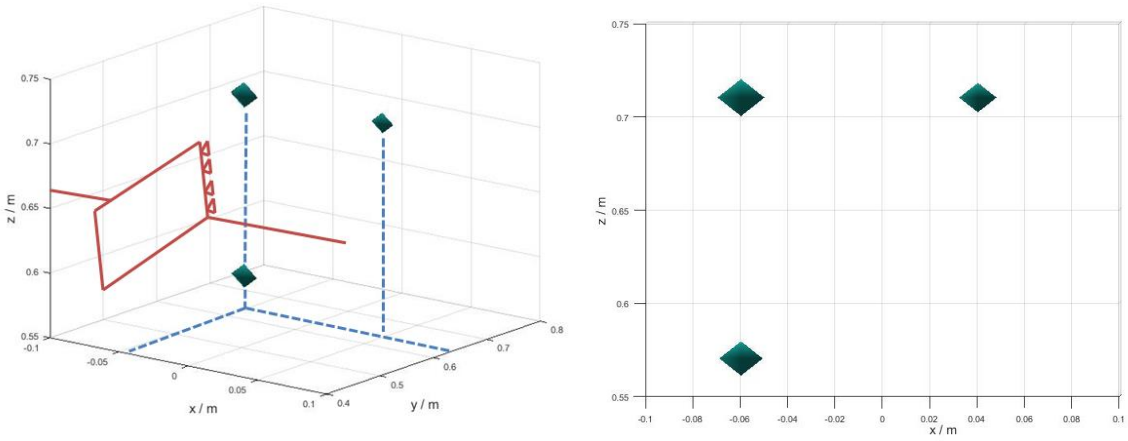

Figure 76 3D image from all channels and its zx-projection.

3.3.2 Image reconstruction for the rotating radar

Most of ground based radar systems use linear track to achieve synthetic aperture, which limits the scope of observation. A few ground based SAR systems adopted arc observation geometry [30], to achieve higher efficiency data acquisition and wider observation comparing with linear scanning system. The radar system via transmitting and receiving wideband electromagnetic signals to achieve high range resolution. The basic idea of this system is to synthesize a large aperture exploiting the spatial diversity of data acquired by an antenna fixed to a horizontally rotating table.

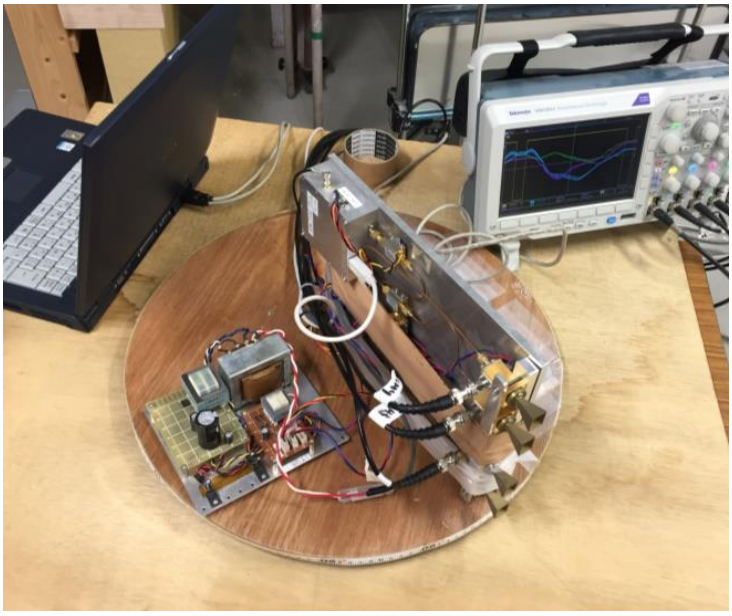

Figure 77 Set-up for the rotating system.

Due to its multichannel specificity the millimeter microwave system uses the different time delay from the receiving antennas placed on a different height to obtain a 3D image of the target. For the azimuth and also range resolution we use SAR, scanning an imaging area with rotation scan as it shown in Fig.76.

In order to get the reconstructed image we use the back projection algorithm from 3.1 and assume that the time delay calculated as

$$U(x_0, y_0, z_0) = \sum_i^n d_i(\tau_i) e^{j2\pi f \tau_i} \tag{3.3}$$

where

$$\tau_i = \frac{\sqrt{(x_0 - r_0 \sin\theta_i)^2 + (y_0 - r_0 \cos\theta_i)^2 + (z_0 - z_i)^2}}{c} + \frac{\sqrt{(x_0 - r_0 \sin\theta_i)^2 + (y_0 - r_0 \cos\theta_i)^2 + (z_0 - z_i + h)^2}}{c} \tag{3.3}$$

where $d_{i.}$ and $\tau_{i,}$ are , correspondingly, a measured signal and a time delay for one transmitter-receiver pair at *i*-th positions, and the angle θ_i , radius of the rotating platform and height of the receiving antennas is taken according to to the configuration of the system described by Fig.77.

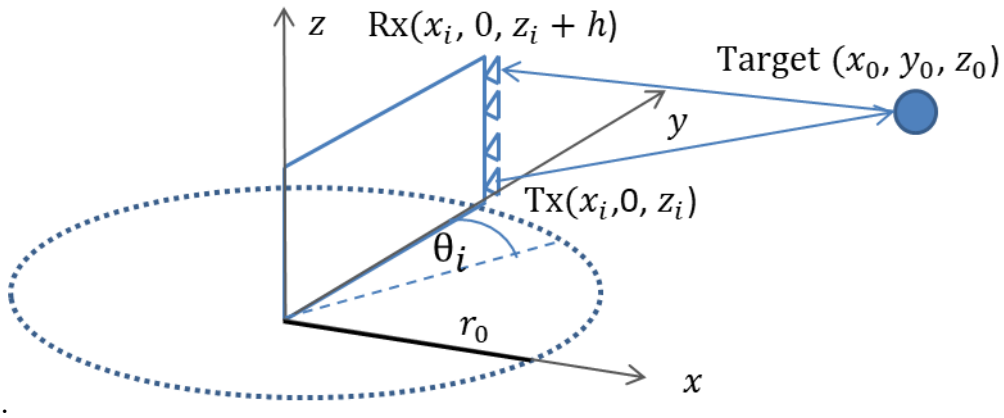

Figure 78 Reconstructed image using diffraction stacking algorithm

After obtaining the IF data from the oscilloscope from each channel, we subtract a background by averaging signal and use Hilbert transform. Then after we calculate the time delay for each antenna and use 3D back projection algorithm from (3.3) to reconstruct an image.

3.3.3 Azimuth resolution

An advantage of the turning SAR system, with comparison to the conventional ground-based linear SAR, is its possibility obtain radar images at 360° with a constant angular resolution. This is an obvious consequence of the circular symmetry of the geometry.

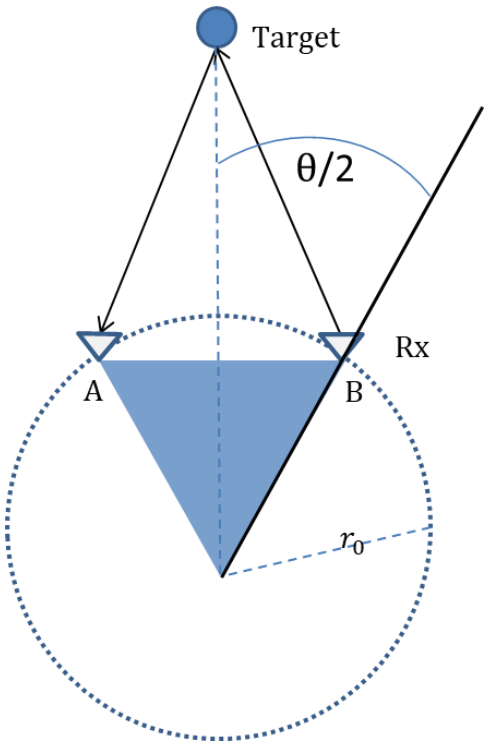

Figure 79 Reconstructed image using diffraction stacking algorithm,

With reference to Fig. 78, if θ is the angular aperture of the antenna, the part of the arc that contributes to the target is AB. On the other hand, the azimuth resolution of the SAR image depends on the linear length of the chord of arc as seen from the image point.

$$d \sin(\frac{\theta}{2}) = \frac{\lambda}{4} \tag{3.12}$$

$$d = 2r \sin(\frac{\theta}{2}) \tag{3.13}$$

where the azimuth resolution depends on the antenna width.

3.3.4 3D Imaging of corner reflectors

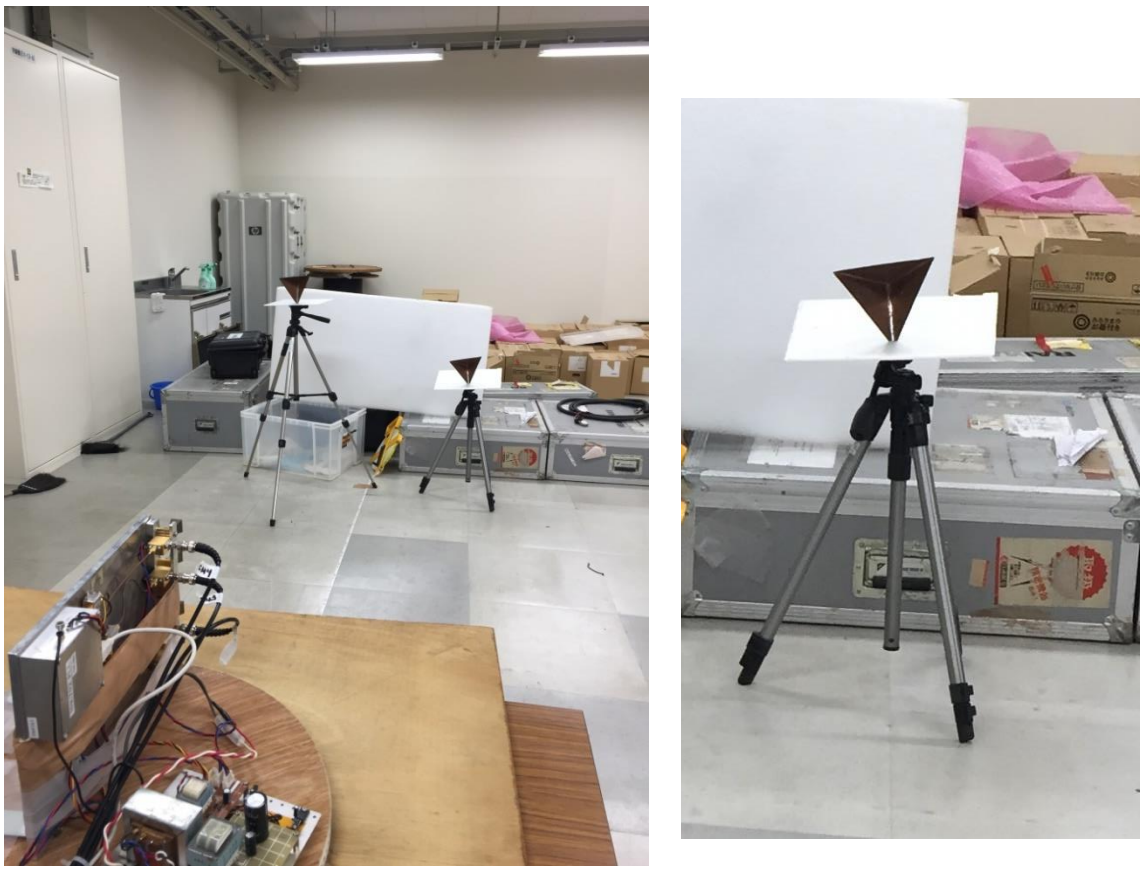

Figure 80 Set-up for the experiment with rotating system.

Table 4.1 Parameter settings for the experiment

Radar position height	0.72m
Aperture length	0.4m
SAR step	4cm

Target	Two trihedral corner reflectors 13cm side
Target position range	≈ 2.2m
Target position height	0.83m and 1.03

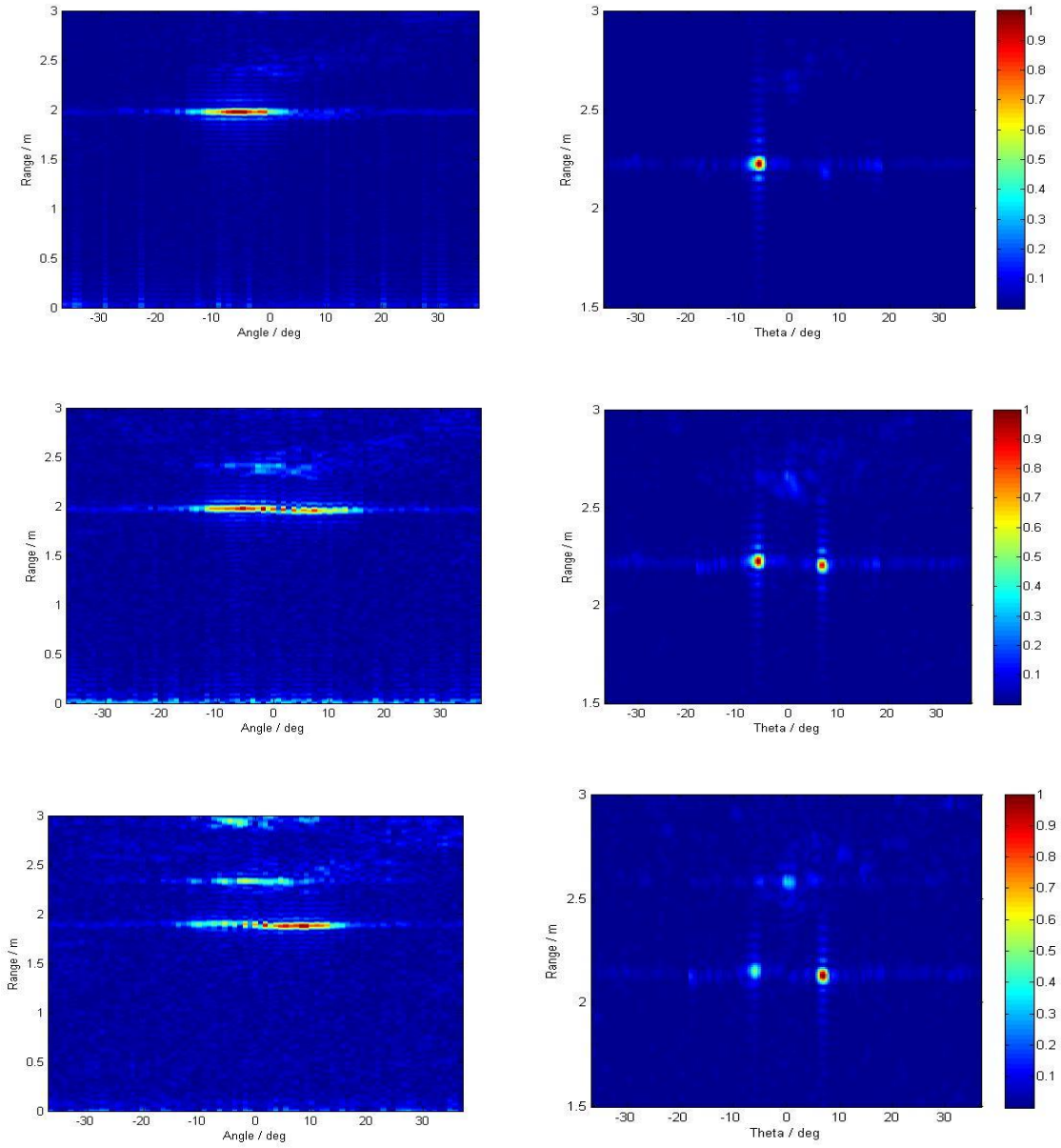

Figure 81 Raw data after FFT and after back projection algorithm for each channnel.

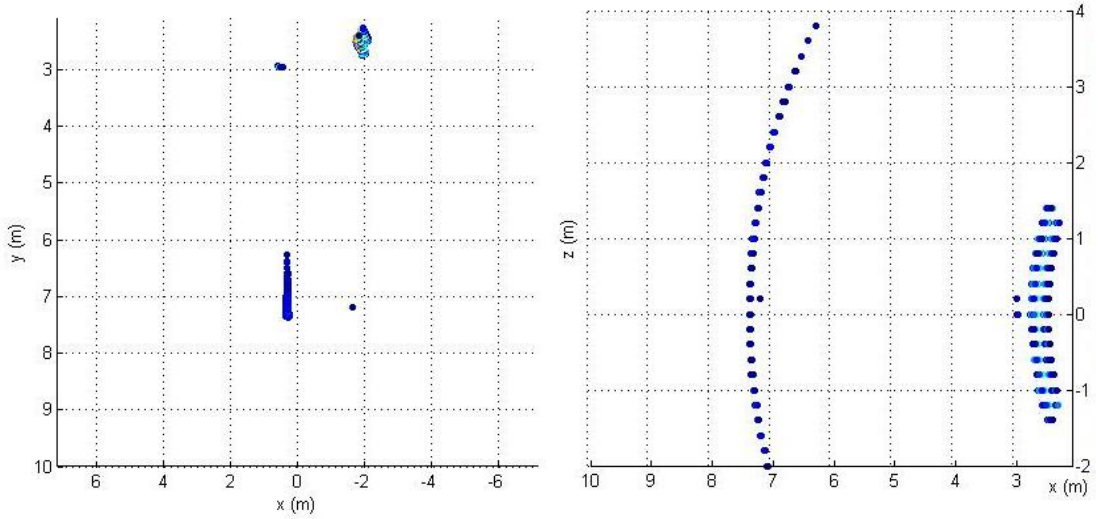

Figure 82 Reconstructed image using diffraction stacking algorithm

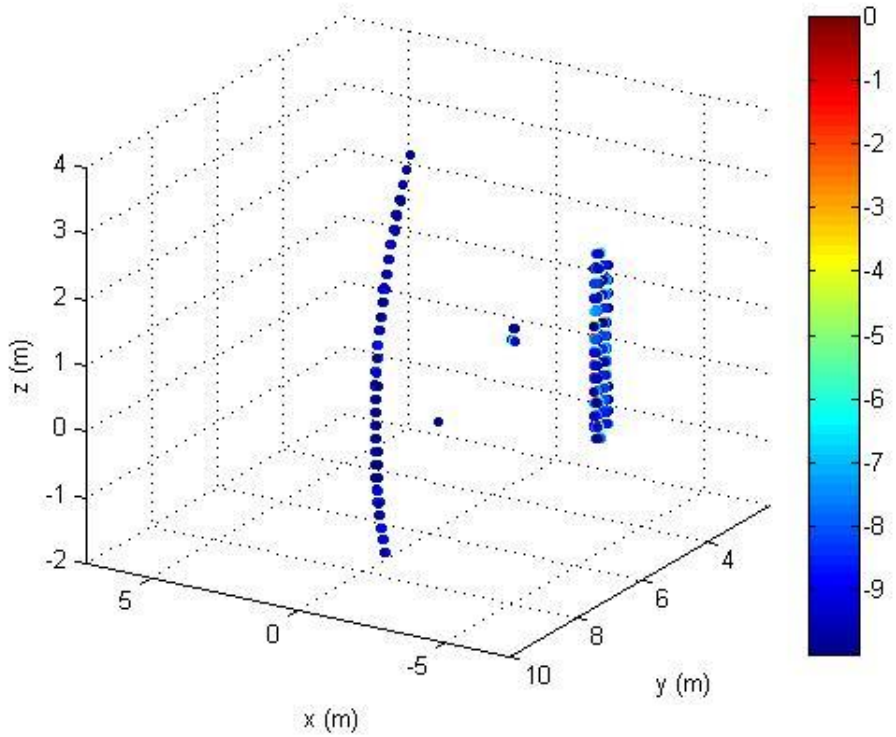

Figure 83 Reconstructed image using 3D back projection algorithm

As it seen from Fig.3 there are several curves stand out sharply against the background, and, by changing the intensity, we can put up a threshold to pick up a high values. The figure represent an images of two metal corner reflectors and objects on the background. Cross section is highly depend on the direction of the reflectors, so the intensity is chosen in a way to show a very sharp reflection of the corner reflector on the right and the second reflector is represented by long curve on the left.

3.4 Radar Tracking system

The basic idea of using the multichannel millimeter microwave system consist in using the different time delay from the receiving antennas placed on a different height to obtain a 3D image of the target. For the azimuth and also range resolution we use SAR, scanning an imaging area with rotation scan. An advantage of the turning SAR system, with comparison to the conventional ground-based linear SAR, is its possibility obtain radar images at 360° with a constant angular resolution. This is an obvious consequence of the circular symmetry of the geometry. Knowing the position of the target, one can solve the reverse problem: if the radar is placed on the moving vehicle, by rotating the radar we can track that vehicle, obtaining the position of the system in three dimension.

3.4.1 2D tracking of the moving cart

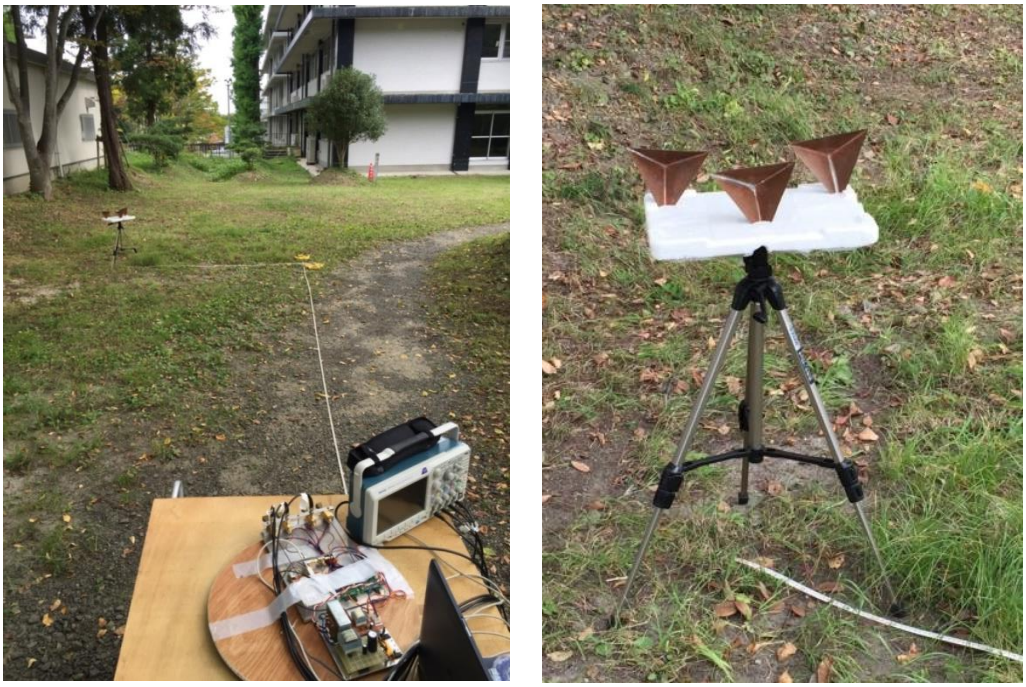

Figure 84 Set up of the tracking experiment and the target.

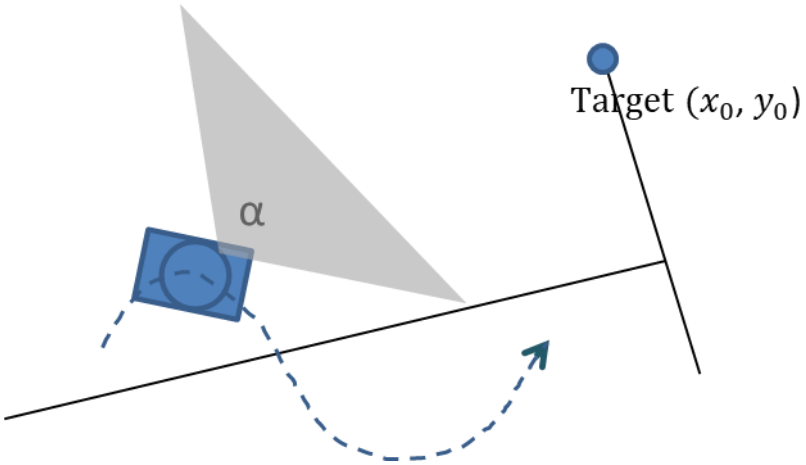

Figure 85 Direction of the moving cart and the total angle of the data acquisition.

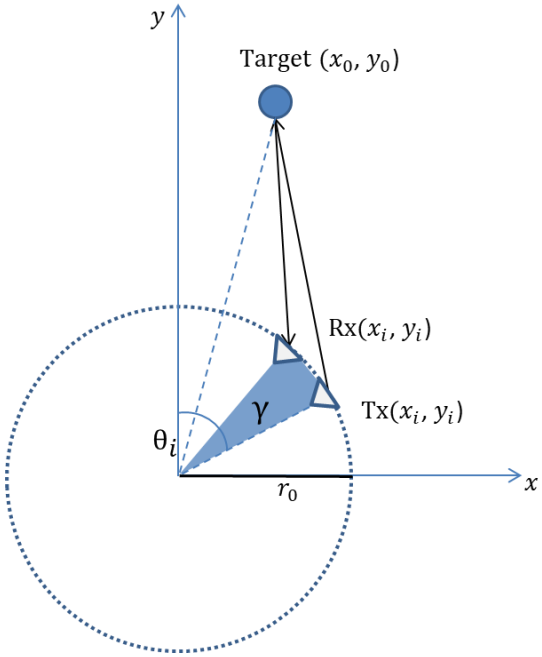

Figure 86 Calculation of the time delay for the rotating radar.

In order to get the reconstructed image we use the back projection algorithm from 3.1 and assume that the time delay calculated as

$$U(x_0, y_0, z_0) = \sum_i^n d_i(\tau_i) e^{j2\pi f \tau_i} \tag{3.3}$$

where

$$\tau_i = \frac{\sqrt{(x_0 - r_0 \sin\theta_i)^2 + (y_0 - r_0 \cos\theta_i)^2}}{c} + \frac{\sqrt{(x_0 - r_0 \sin(\theta_i - \gamma))^2 + (y_0 - r_0 \cos(\theta_i - \gamma))^2}}{c} \tag{3.3}$$

Where is the θ_i – angle between i-th position of transmitter and y-axis, γ – angle between antennas and r_0 - radius of the turn table.

Table 4.1 Simulated antennas characteristics and size

Bandwidth	3GHz (72GHz…75GHz)
Sweep time	3ms
Samples/sweep	800
Aperture length	0.36m
SAR step	4cm
Target	Three trihedral corner reflectors 13cm side
Target position range	variates

Unfortunately, this resolution is not high enough to be exploited to synthesize 3-D imaging but it could be enough to give an "defocusing effect" when an image is focused on the rotation plane.

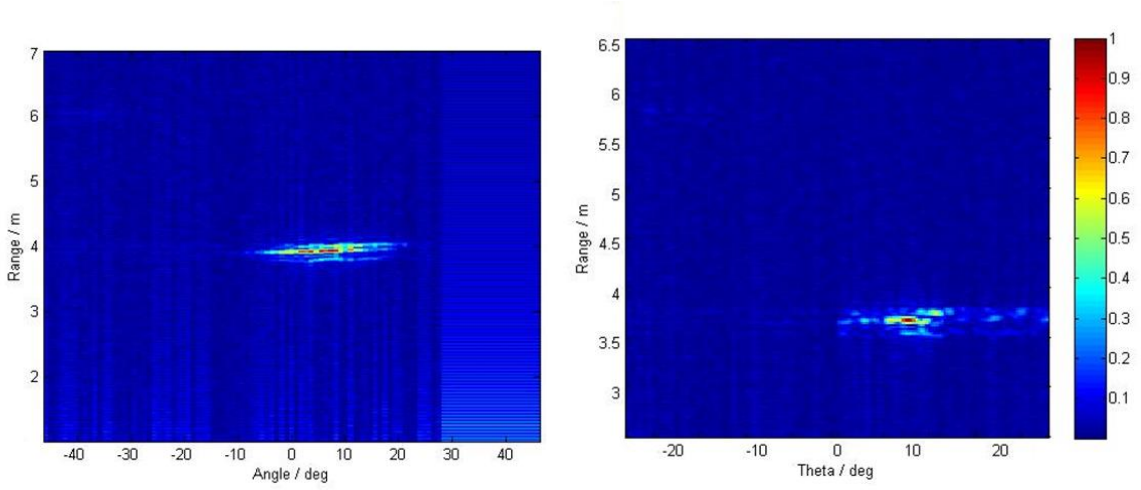

Figure 87 Raw data after FFT and processed image

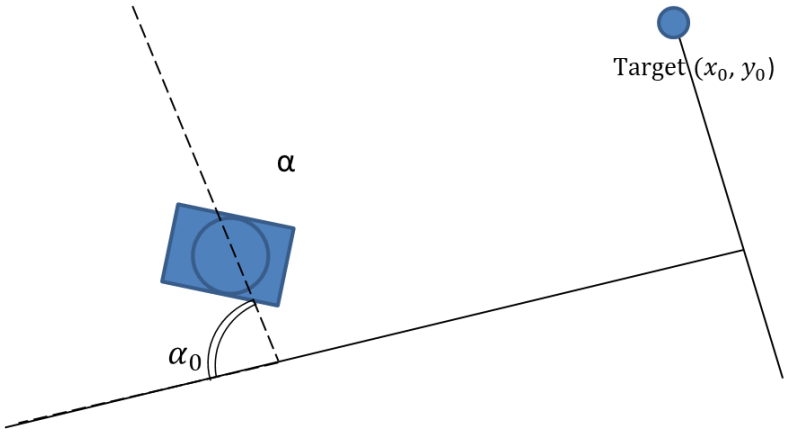

Figure 88 Calculating of the radar position from the range and angles from the reconstructed image.

After getting the distance to the target and angle between the north direction and direction to the target from the reconstructed image by:

$$\begin{cases} x = x0 - \mathrm{r} \cdot \cos(180 - \alpha - \alpha_0) \\ y = y0 - \mathrm{r} \cdot \sin(180 - \alpha - \alpha_0) \end{cases} \tag{3.3}$$

We get position of the radar along the set of 6 experiments

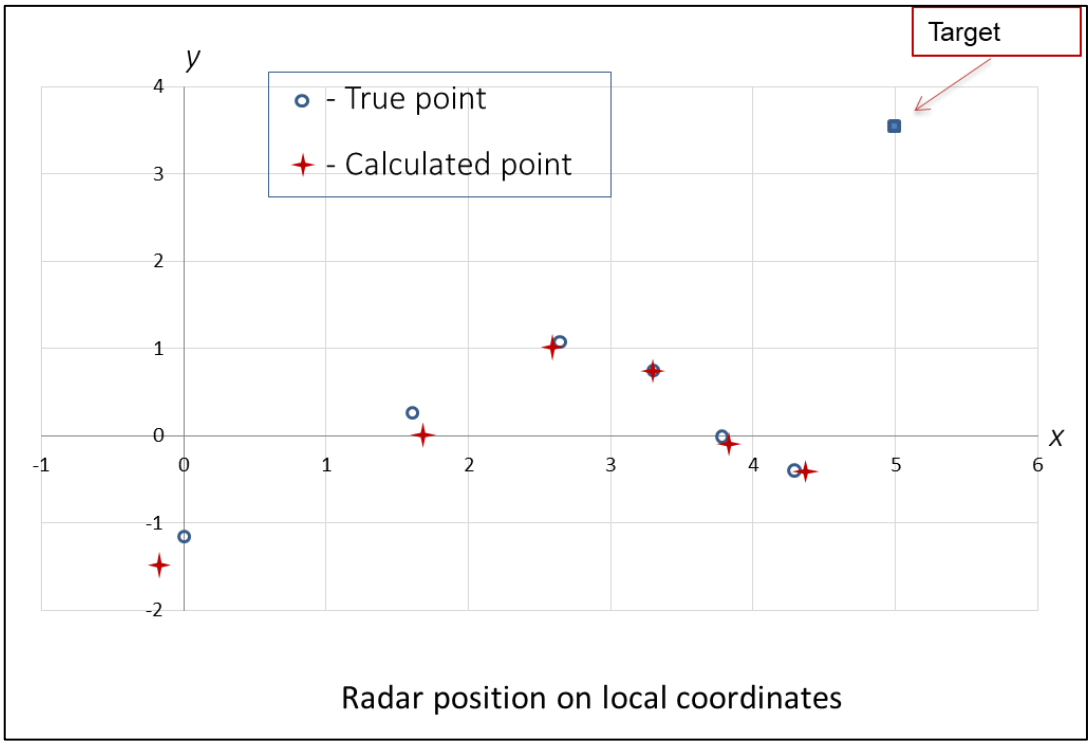

Figure 89 Turn table position tracking along the way around the target

Using the rotation of the radar intensively increasing the imaging area however the resolution in azimuth direction is reducing, that is increasing the error of the target detection with distance

However, the two-dimensional data acquisitions of such system is using the mechanical movement, which seriously affect the data acquisition efficiency.

3.4.3 3D tracking experiment

In order to use the rotating millimeter wave radar for the 3D tracking, we paced a turn table on a cart and moved it in front of the three corner reflectors as it shown in Fig. 88.

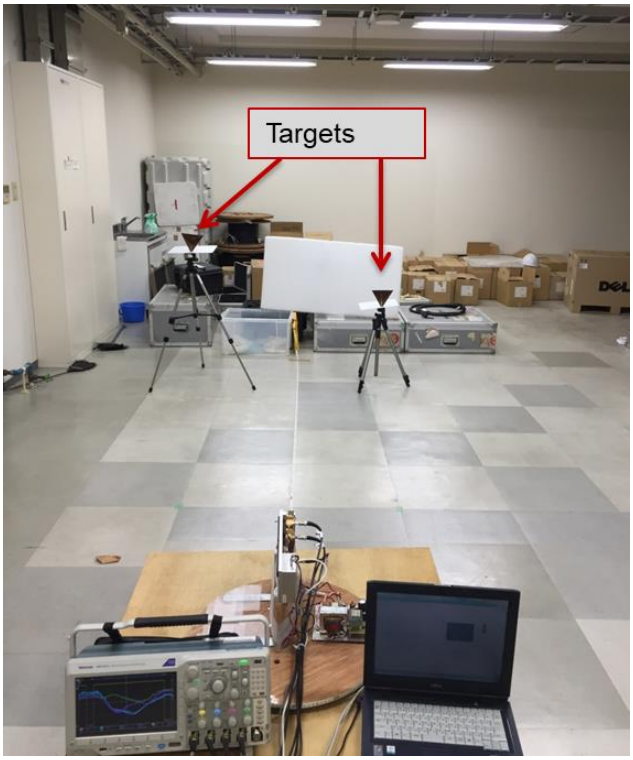

Figure 90 Turn table position tracking along the way around the target

Initially we have three target in front of the moving system, a three trihedral corner reflectors 13cm side, each on a different height. During the experiment we move a cart along some random track, and made 7 positions to obtain data. For different positions a height of the radar was also changed randomly from 0.33m to 0.92m. Data acquisition was done by circular rotating with 0.4 aperture length and 4cm SAR step.

Table 4.1 Parameter settings for the experiment

Radar position height	Variates from 0.33 to 0.92
Aperture length	0.4m
SAR step	4cm
Target	Three trihedral corner reflectors 13cm side
Target position range	Variates
Target position height	1.15m, 0.95 and 0.75

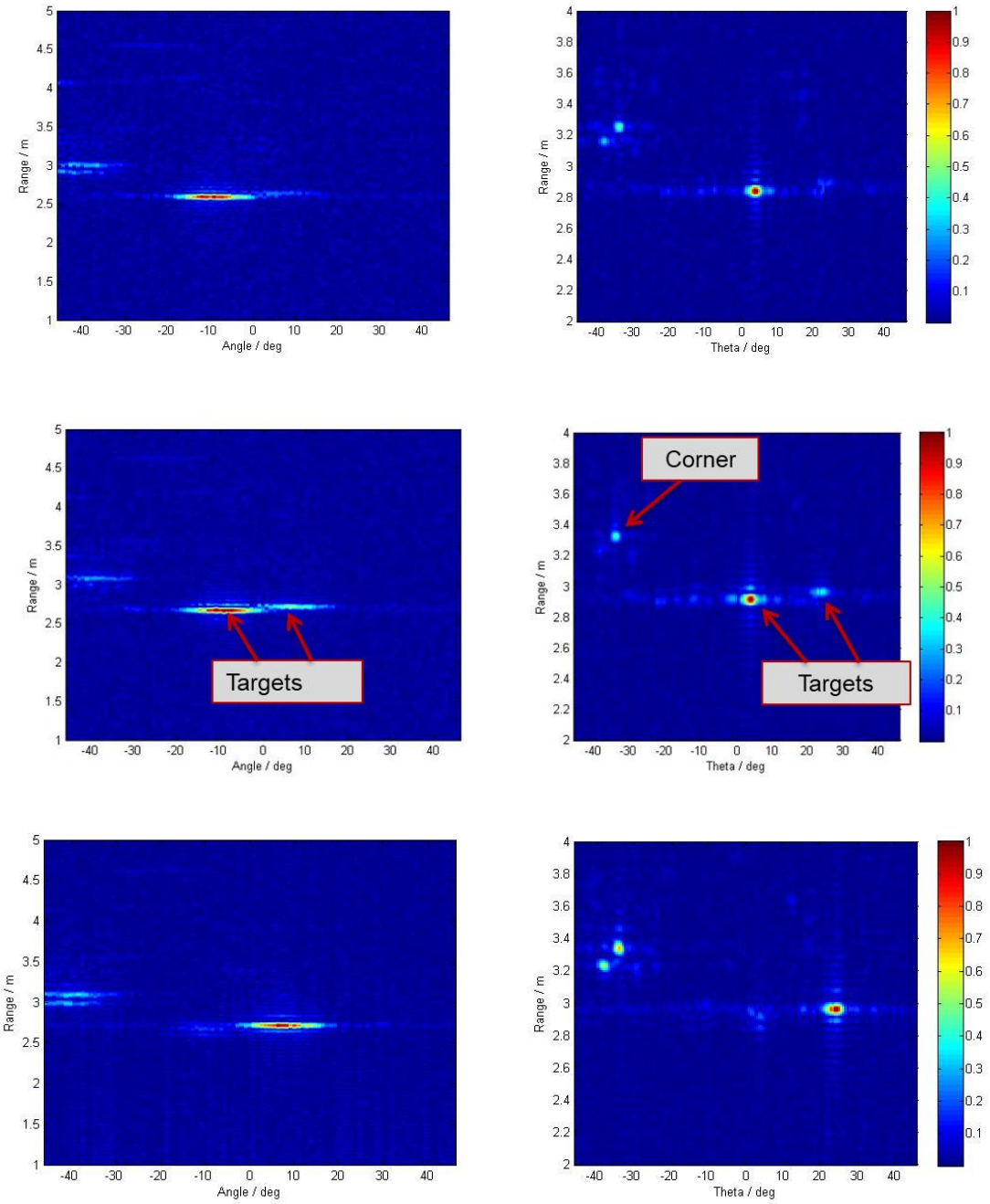

Figure 91 Raw data after FFT and processed image for three channels

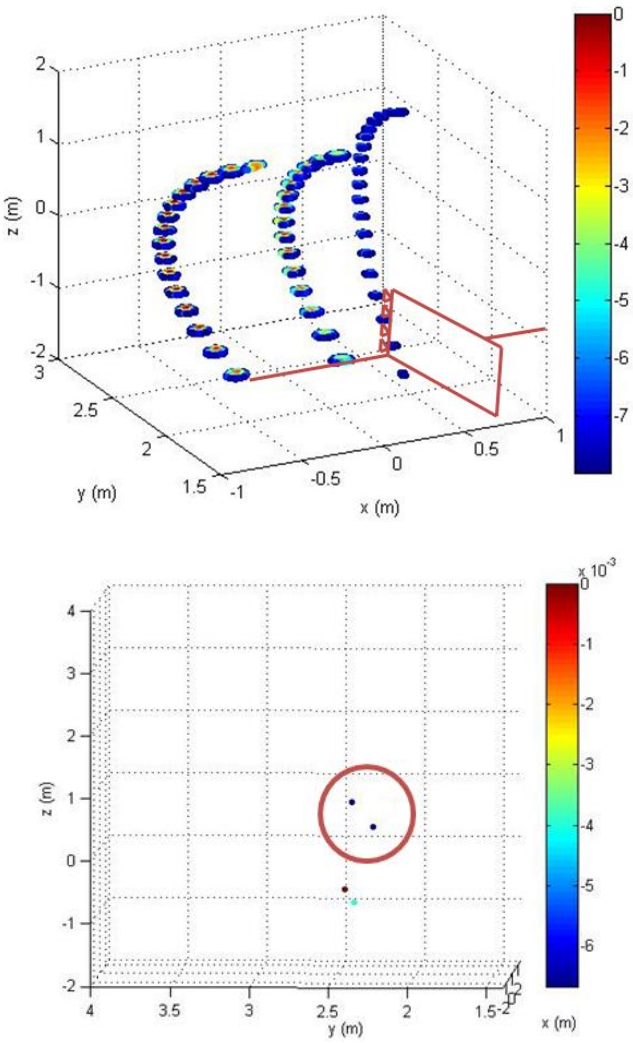

Figure 92 3D image of the corner reflectors (a), and a focused image of two corner reflectors of the same data in height and distance to the target

As it seen from Fig.90 there are several curves stand out sharply against the background, and, by changing the intensity, we can put up a threshold to pick up a high values. The figure represent an images of three metal corner reflectors and objects on the background. Cross section is highly depend on the direction of the reflectors. Last figure represents the focused image of two corner reflectors of the same data as the previous image. The threshold of the intensity was chosen to pick up the high values.

Three curves representing each of the targets, and the high values of its represent the position of the reflectors in 3D. Knowing coordinates of the targets we can track the position of the radar and compare it with coordinates of the radar position from the experiment. It could be calculated relatively to the any of the target, and Figs. 91-92 represent the results of the tracking of the cart with radar system on it relatively to the 3rd target

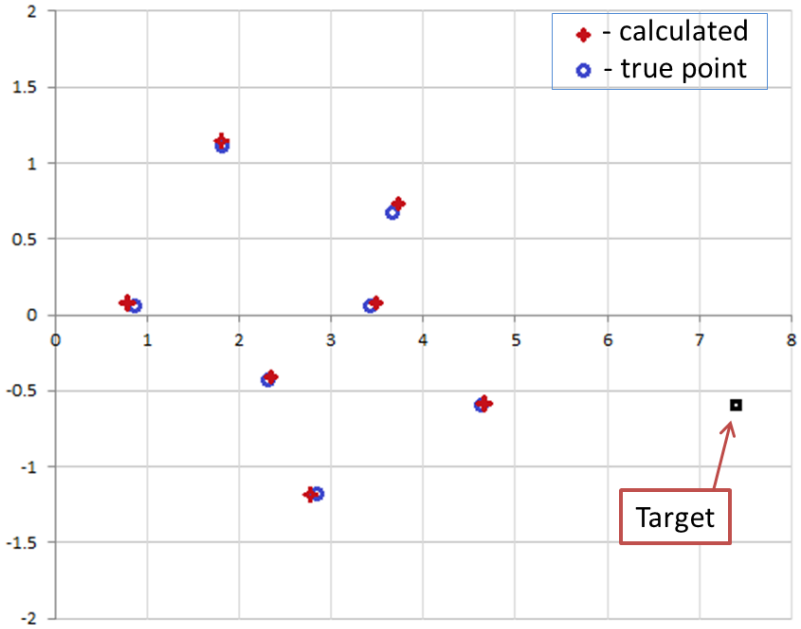

Figure 93 Turn table position tracking along the x and y dimensions.

Figure 6 represent a tracking of the cart with radar on it done in azimuth and range axis. Wide imaging area, given by rotation of the radar, losing the azimuth resolution compare to linear scan, however, at least 5 cm accuracy at this distances is achieved. Accuracy here is guaranteed by large aperture of the SAR.

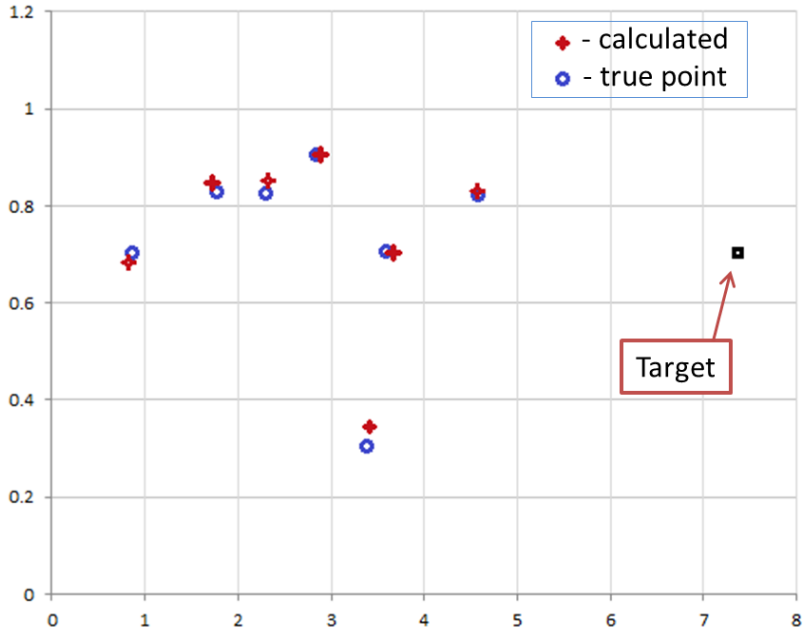

Figure 94 Turn table position tracking along the distance and height.

Figure 6 represent a tracking of the cart with radar on it done in height and range axis. Resolution here, besides the distance to the target, is depend on the radiation pattern. We can

calculate the position of the radar relatively to the other target and see the error.

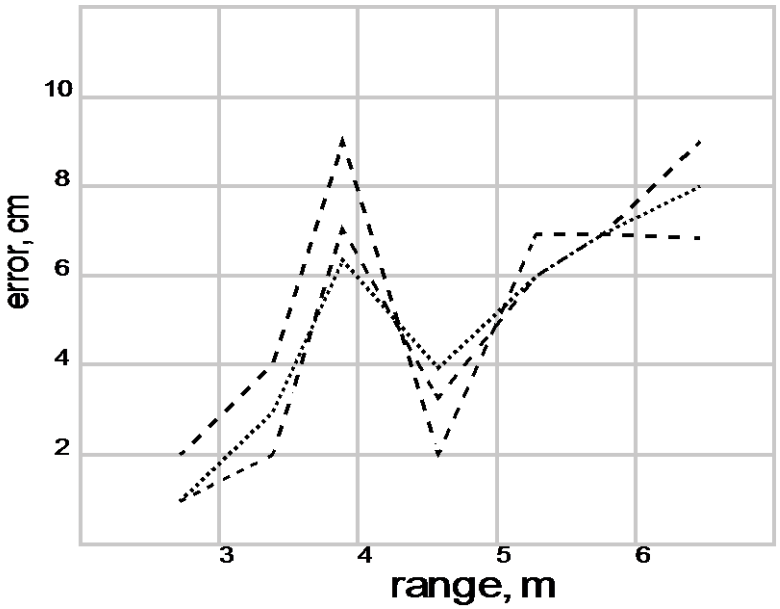

Figure 95 Turn table position tracking along the distance and height.

Fig.92 represent the rising error of the radar position in height calculated relatively to three separate targets The obvious increasing of the error with range is also meet the higher error when the position of the radar was too low. It leads directly to the radiation pattern and also direction of the corner reflectors. The other reason is the different radar cross section due to different direction of the corner reflections. It could be solved using the omnidirectional reflector as a target for the tracking reference.

Chapter 4 Optimization of the Antenna Array for a Millimeter Wave Radar

In order to increase the vertical resolution for the 3D imaging with millimeter wave radar, one can simply add more antennas in the vertical axis. In this case we could use the optimization algorithm from the Chapter 2 to find antenna positions for the radar. In this chapter I give the results of several numerical calculations to simulating linear array for the FMCW radar.

4.1 Antenna array for a millimeter wave radar

4.1.1 Radiation pattern

Theoretically speaking, the wider the antenna pattern the better the azimuth resolution. An omnidirectional antenna can synthesize an aperture equal to its diameter or the largest possible aperture. Unfortunately, the wider the antenna pattern the higher the side lobes in the focused image. Images affected by such side lobes are unusable in most applications. By limiting the analysis to the horn antennas, we can simulate the PSF for a target at a range R using the following parameters:

Here are results of calculation of current antenna and two antennas with different radiation pattern: wide only in H-plane and wide in both planes. Antennas calculated at 75GHz frequency.

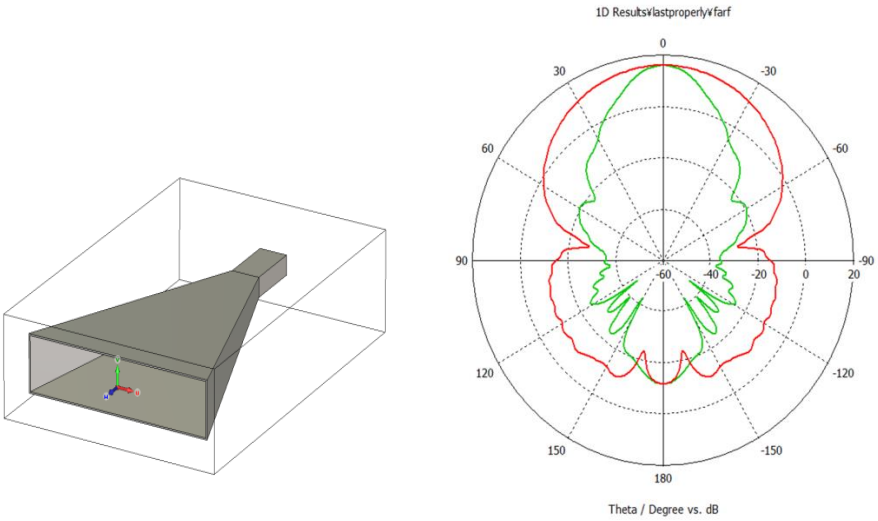

Figure 96 Low gain horn antenna with wide beam in H-plane (a) and its radiation pattern (b)

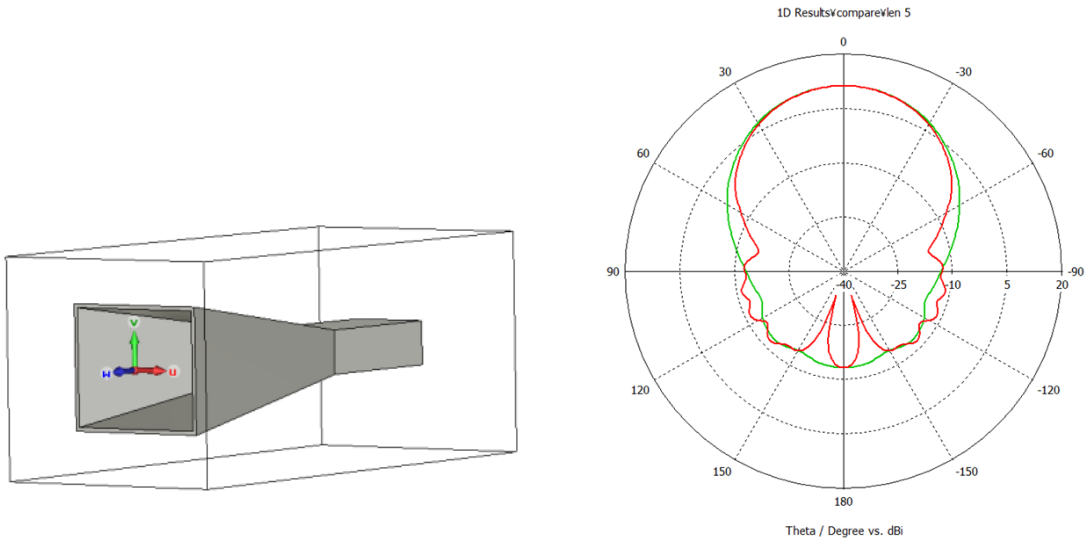

Figure 97 Low gain horn antenna with wide beam in both planes (a) and its radiation pattern (b)

Table 4.1 Simulated antennas characteristics and size

Name	Antenna parameters	Geometry (in mm)
High gain Antenna	Main lobe H-plane: 16.8º	Aperture height: 15.35
	Main lobe E-plane: 18.1º	Aperture width: 18.25
	Side lobe level: -12.6dB	Flare length: 24
	Directivity: 20.5dBi	Waveguide length: 5.3
Low gain Antenna 1	Main lobe H-plane: 49.4º	Aperture height t: 4.2
	Main lobe E-plane: 16.9º	Aperture width : 18.25
	Side lobe level: -25.6dB	Flare length : 23.7
	Directivity: 16.2dBi	Waveguide length:: 5.3
Low gain Antenna 2	Main lobe H-plane: 50º	Aperture height : 4.10
	Main lobe E-plane: 51.9º	Aperture width : 4.9
	Side lobe level: -22.8dB	Flare length : 9.83
	Directivity: 11.33dBi	Waveguide length:: 5.3

4.1.2 Numerical calculation

There are results of the optimization of the 2D sparse array according to the simulation with accumulation of 10 packs of 6 targets in random positions, as it was done in the simulation in Chapter 2. In order to get the positions for antennas with the high focusing performance for the radar, I also used the cost function from (2.7) minimizing it as follows:

$$S = \sum \frac{\left\| U(x,y,z)|_{x,y,z \notin \Omega} \right\|_{L2}}{\left\| U(x,y,z)|_{x,y,z \in \Omega} \right\|_{L0.5}} / Ntar \rightarrow min \tag{4.1}$$

The total simulated area for optimization is a 1m side cube represented by 3D matrix the size of 50x50x50 points with the target position at 2m range. Simulation was done with low gain antennas with 50º main lobe in both planes on the 75GHz frequency. For the initial parameters I took a positions of the dense linear array with 5 receiving antennas and one transmitter placed as first in a row and an antenna array aperture 0.5m - to keep it more compliable for a real application. Radiation pattern for the simulation is an approximation of using the symmetrical radiation pattern with 50 º beamwidth, to consider the arriving angles. Last important parameter of the simulation is the random target distribution with 6 targets and accumulation factor 3x. It means that for each iteration step we simulate calculate the cost function for three different distribution of the targets, sum it and divide by the numbers of the targets (3x factor was enough for the 1 dimensional array to not get stuck at the local minimum during the optimization process).

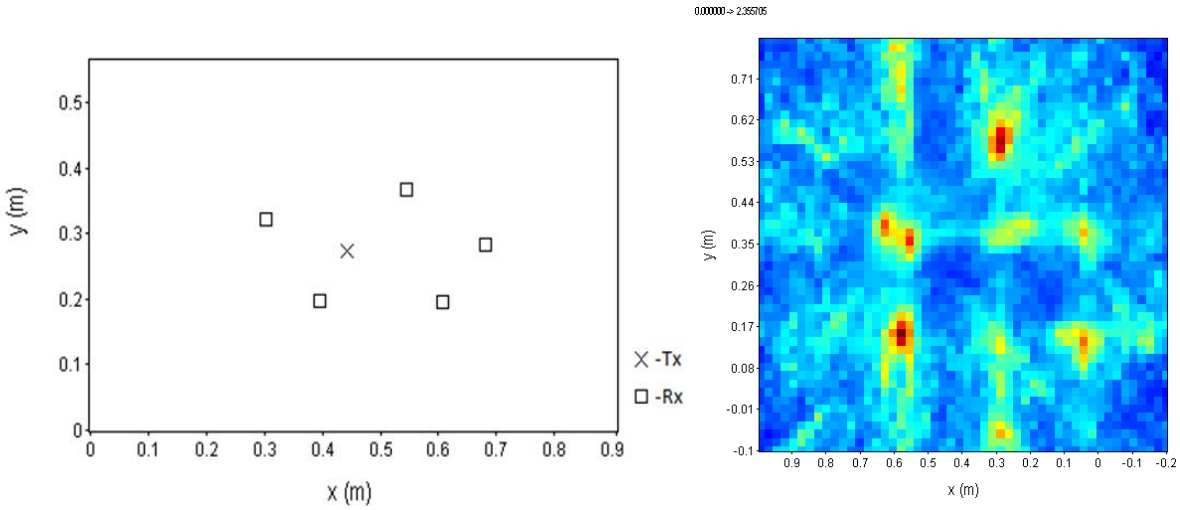

Figure 98 Antenna pattern (a) and stacked 3D PSF of 6 targets imaged by optimized antenna array with 5 receivers (b)

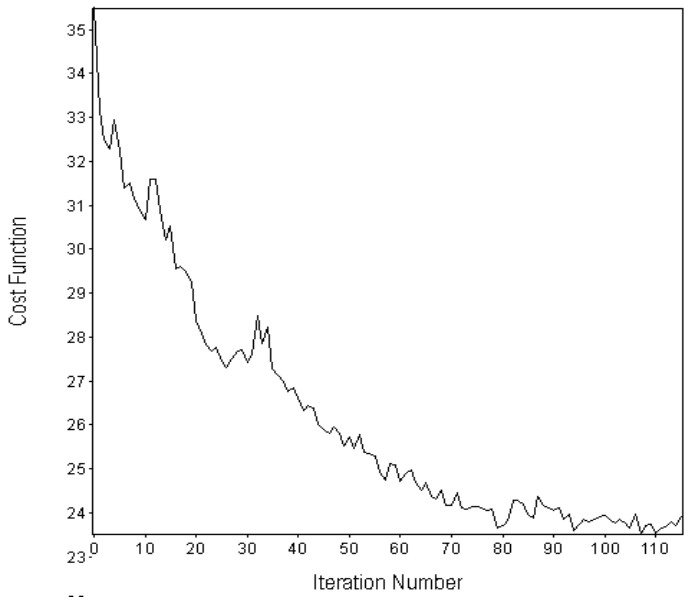

Figure 99 Cost function progress during the optimization

For the boundary values I took a rectangular 20 by 40 cm in order to have more practical compact results. During simulation as it was expected the optimized antenna positions for receivers reached the boundaries trying to reach highest sparsity of the middle points. Figs.95-96 represent one of the layout after optimization and progress of the cost function during simulation. Optimization step was chosen in a way to have small gradient of the optimization and it was still able to move transmitter on the side of the array, reducing the total resolution, but in terms of the cost function it was increasing – bright example of the wrong local minimum.

Assuming that for the linear scanning radar we already have a high azimuth resolution and to find a pattern for better vertical resolution, for the next simulation it was allowed to change the positions of antenna in only one axis. Figs.97-98 represent a results of optimization of two linear arrays with 4 and 9 receiving antennas.

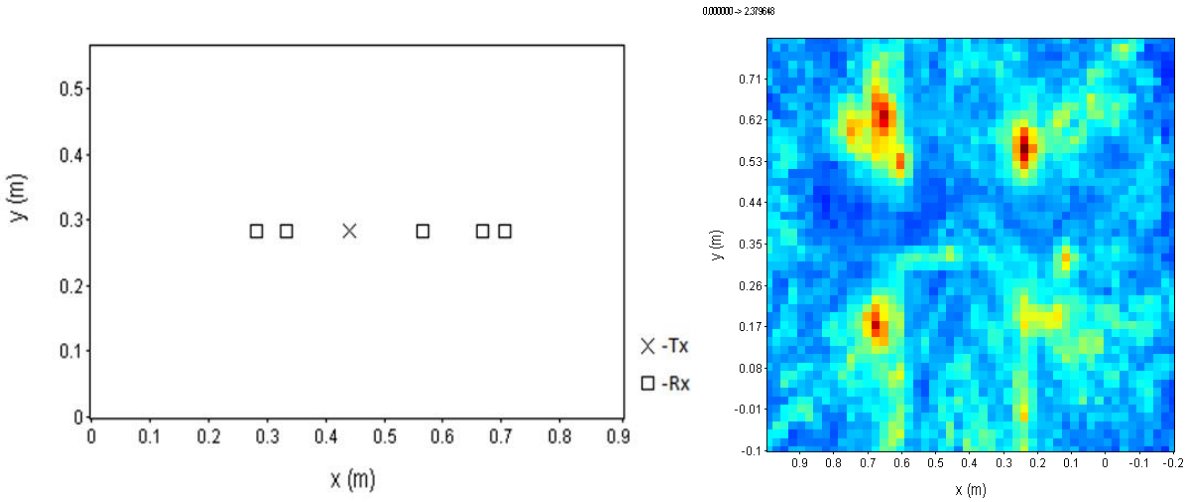

Figure 100 Antenna pattern (a) and stacked 3D PSF of 6 targets imaged by optimized linear antenna array with 5 receivers (b)

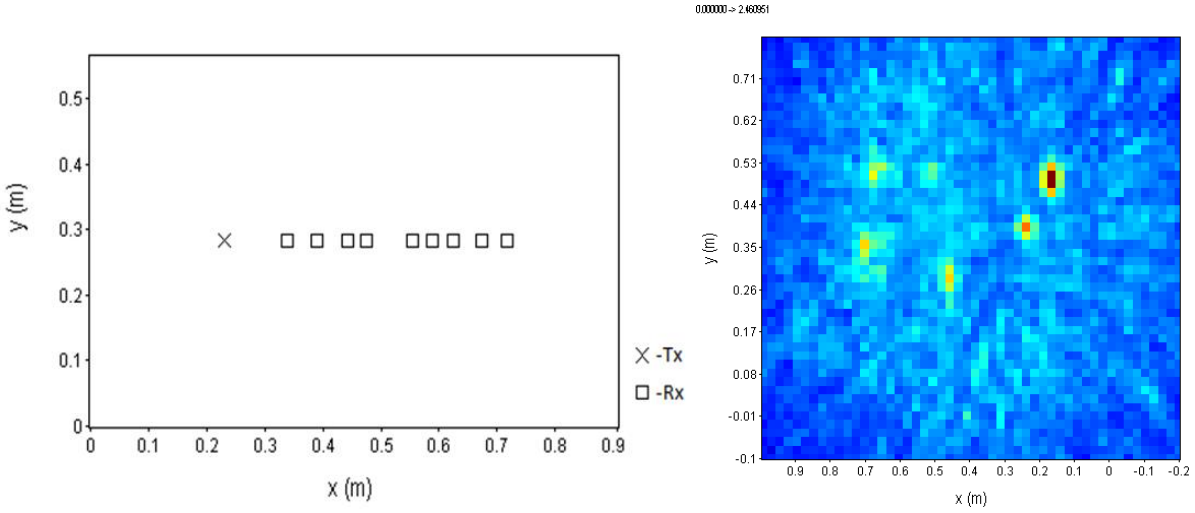

Figure 101 Antenna pattern (a) and stacked 3D PSF of 6 targets imaged by optimized linear antenna array with 9 receivers (b)

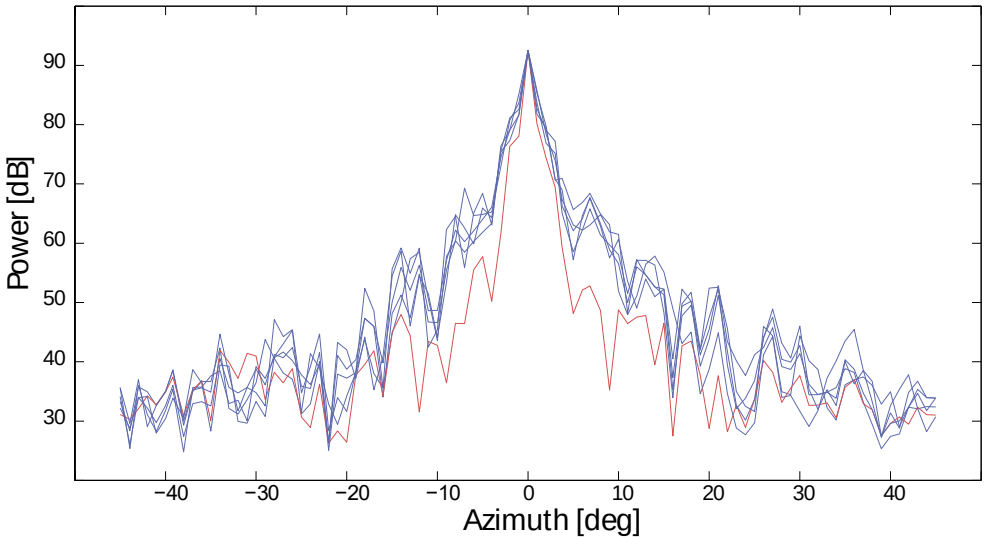

Figure 99 A comparison of the initial layout of the array (red) and 5 results of the optimization

Fig. 99 shows a comparison between resolution of the initial array (red) and 5 results of the optimization. The image represent image of the target in one profile - vertical axis which in terms of the simulation is the same axis where linear array placed along. The results of the optimization with $L_{0.5}L_2$-norm cost function and random target distribution for 10 elements linear antenna arrays showed an increasing of the side lobes. One of the reason of this is the inadaptability of the 3D PSF calculation for the 1D array: the algorithm though can be used with modified cost function. Second point is the optimization algorithm: Simulated Annealing algorithm with more traditional minimizing of the maximal weighted sidelobe showed a better results in a number of papers. However these optimizations was done with array thinning – when number of antennas in array reducing during optimization from the uniform array, and proposed optimization algorithm changes positions of the antennas.

Chapter 5 Conclusions and Perspectives

This dissertation focuses on the modeling and interpretation of the electromagnetic scattering in near range imaging radar. The main contributions and innovations, together with further perspectives are summarized as follows:

- **Antenna array optimization algorithm**

Firstly, a method of optimization was proposed. A few different relations of the L-norm of the reconstructed image were compared. A $L_{0.5}$-norm maximization for the targets and a L_2-norm minimization for the artifacts showed better results compare to others. Relation of these two norms is one of the key features of the method.

Another feature is related to making the optimized solution warranted for the different positions of the targets. It is using a random target distribution for an each iteration of the optimization algorithm. Also the accumulating of the cost function, using several combination of the targets at each step of the optimization, was used. It making the optimization process keep away from been stuck in local minimum pushing it to further minimization of the cost function.

The weak point of the method could be an optimization algorithm. A gradient descent is simple in use which made it very easy to implement for the fast calculation even with accumulation. However an algorithm suffer from been easy stuck in local minimum without any key of avoid it. More advanced Algorithm should be used in order to rid of this problem.

- **3D imaging with millimeter wave radar**

Different types of migration with the frequency modulated signal radar provide a high resolution imaging of a target, and linear and rotating scanning have been used to achieve it.

3D back projection algorithm was applied to reconstruct an image of a target and succeed in getting a precise position of it. Taking into account that the very high azimuth resolution could be achieved by synthetic aperture radar, the vertical resolution is still could be a problem. 3-channels system however performed quite good results in obtaining the high of the target position, allowed us to propose a way of tracking the radar system using rotating table. The experiment with tracking of the radar was done outside in two dimensions and in three dimensions in laboratory conditions.

Mechanical movement strongly limits this system and keep it away from more advanced applications. Ideally, the millimeter wave radar should be mounted on a free-rotating platform with high movement ability, like a human body. Then a free movement of the system could be

used for continues data acquisition, obtaining a high resolution in desirable direction. The problem of such using is the position tracking, requiring for the processing. Indoor tracking system could be using as for beginning.

References

[1] S. S. Ahmed, A. Schiessl, F. Gumbmann, M. Tiebout, S. Methfessel and L. P. Schmidt, "Advanced Microwave Imaging," in *IEEE Microwave Magazine*, vol. 13, no. 6, pp. 26-43, Sept.-Oct. 2012.

[2] Motoyuki Sato, "Near range radar and its application to near surface geophysics and disaster mitigation", Journal of Earth Science, vol. 26, pp. 858, 2015, ISSN 1674-487X.

[3] T. Vaupel and T. F. Eibert, "Comparison and application of near-field ISAR imaging techniques for far-field Radar cross section determination," in *IEEE Transactions on Antennas and Propagation*, vol. 54, no. 1, pp. 144-151, Jan. 2006.

[4] M. Grasmueck, R. Weger, H. Horstmeyer, "Full-resolution 3-D GPR imaging", Geophysics, vol. 70, no. 1, pp. K12-K19, Jan./Feb. 2005.

[5] S. Scott and J. Wawrzynek, "Compressive sensing and sparse antenna arrays for indoor 3-D microwave imaging," 2017 25th European Signal Processing Conference (EUSIPCO), Kos, 2017, pp. 1314-1318

[6] S. Holm, B. Elgetun, and G. Dahl, “Weight- and layout-optimized sparse arrays” in Proc. Int. Workshop on Sampling Theory and Applications, pp. 97–102, June 1997.

[7] H. Nyquist. Certain topics in telegraph transmission theory. Trans. Amer. Inst. of Elect. Eng., 47:617–644, Apr. 1928.

[8] Y. Iitsuka, C. N. Koyama, K. Takahashi and M. Sato, "Design of wideband small spiral antenna for SAR," 2015 IEEE 4th Asia-Pacific Conference on Antennas and Propagation (APCAP), Kuta, 2015, pp. 261-262.

[9] A. Lyulyakin, I. Chernyak, M. Sato "Antenna design for the sparse array and the array pattern optimization" IEICE Tech. Rep., vol. 116, no. 526, AP2016-196, pp. 103-107, March 2017

[10] I. Chernyak and M. Sato, "Least square image reconstruction method for sparse array radar system," 2016 International Symposium on Antennas and Propagation (ISAP), Okinawa, 2016, pp. 632-633.

[11] Gonzalez-Valdes, G. Allan, Y. Rodriguez- Vaqueiro, Y. Alvarez, S. Mantzavinos, M. Nickerson, B. Berkowitz, J. A. Martinez-Lorenzo, F. Las-Heras and C. M. Rappaport, "Sparse array optimization using simulated annealing and compressed sensing for near-field millimeter wave imaging", IEEE Trans. Ant. Prop., vol. 62, no.4, pp. 1716-1722, 2014.

[12] G. Prisco M. D’Urso "Maximally sparse arrays via sequential convex optimizations" IEEE Antennas Wireless Propag. Lett. vol. 11 pp. 192-195 2012.

[13] C. Bencivenni, M. Ivashina, R. Maaskant, and J. Wettergren, “Design of maximally sparse antenna arrays in the presence of mutual coupling,”IEEE Antennas Wireless Propag. Lett. vol. 14, pp. 159–162, 2015.

[14] Y. M. Lu and M. N. Do. A theory for sampling signals from a union of subspaces. IEEE Trans. Signal Processing, 56(6):2334–2345, 2007.

[15] A. V. Oppenheim and R. W. Schafer. Digital Signal Processing. Prentice Hall, Englewood Cliffs, NJ, 1975.

[16] Rajashree Jain and GS Mani. Solving antenna array thinning problem using genetic algorithm. Applied Computational Intelligence and Soft Computing, 2012:24, 2012.

[17] ML Skolnik, J Sherman III, and F Ogg Jr. Statistically designed density-tapered arrays. Antennas and Propagation, IEEE Transactions on, 12(4):408–417, 1964.

[18] Eyung W Kang. Radar system analysis, design, and simulation. Artech House Publishers, 2008.

[19] Nuchter, A.; Lingemann, K.; Hertzberg, J.; Surmann, H. Heuristic-Based Laser Scan Matching for Outdoor 6D SLAM. Lect. Notes Comput. Sci. 2005, 3698, 304–319.

[20] Foessel-Bunting, A.; Bares, J.; Whittaker, W. Three-dimensional Map Building with MMW RADAR. In Proceedings of the International Conference on Fienldand Service Robotics, Otaniemi, Finland, 11–13 June 2001.

[21] C. Atzeni, M. Barla, M. Pieraccini, and F. Antolini, "Early warning monitoring of natural and engineered slopes with ground-based synthetic aperture radar," Rock Mech. Rock Eng., vol. 48, no. 1, pp. 235–246, 2015.

[22] M. Pieraccini, "Monitoring of civil infrastructures by interferometric radar: A review," Sci. World J., vol. 2013, 2013, Art. no. 786961.

[23] D. Mecatti, G. Macaluso, A. Barucci, L. Noferini, M. Pieraccini, and C. Atzeni, "Monitoring open-pit quarries by interferometric radar for safety purposes," in Proc. Eur. Radar Conf. (EuRAD), vol. 30. Sep./Oct. 2010, pp. 37–40.

[24] M. Pieraccini et al., "Structural static testing by interferometric synthetic radar," NDT E Int., vol. 33, no. 8, pp. 565–570, Dec. 2000.

[25] D. Dei, M. Pieraccini, M. Fratini, C. Atzeni, and G. Bartoli, "Detection of vertical bending and torsional movements of a bridge using a coherent radar," NDT E Int., vol. 42, no. 8, pp. 741–747, Dec. 2009.

[26] D. Dei, D. Mecatti, and M. Pieraccini, "Static testing of a bridge using an interferometric radar: The case study of 'ponte degli alpini,' Belluno, Italy," Sci. World J., vol. 2013, 2013, Art. no. 504958.

[27] M. Jeon and Y. S. Kim, "Migration technique for rotor synthetic aperture radar," Electron. Lett., vol. 33, no. 7, pp. 630–631, Mar. 1997.

[28] M. Bara, L. Sagués, F. Paniagua, A. Broquetas, and X. Fàbregas, "Highspeed focusing algorithm for circular synthetic aperture radar (C-SAR)," Electron. Lett., vol. 36, no. 9, pp. 1–2, Apr. 2000.

[29] H. Lee, J.-H. Lee, K.-E. Kim, N.-H. Sung, and S.-J. Cho, "Development of a truck-mounted arc-scanning synthetic aperture radar," IEEE Trans. Geosci. Remote Sens., vol. 52, no. 5, pp. 2773–2779, May 2014.

[30] F. Ali, G. Bauer, and M. Vossiek, "A rotating synthetic aperture radar imaging concept for robot navigation," IEEE Trans. Microw. Theory Techn., vol. 62, no. 7, pp. 1545–1553, Jul. 2014.

[31] Demirci, Sevket & Cetinkaya, Harun & Yigit, Enes & Ozdemir, Caner & Vertiy, Alexey. (2012). A study on millimeter-wave imaging of concealed objects: Application using back-projection algorithm. Progress In Electromagnetics Research. 128.

[32] Huang, Zengshu & Sun, Jinping & TAN, Weixian & Huang, Pingping & Han, Kuoye. (2017). Investigation of Wavenumber Domain Imaging Algorithm for Ground-Based Arc Array SAR. Sensors. 17. 2950. 10.3390/s17122950.

[33] M. Pieraccini et al., "Remote sensing of building structural displacements using a microwave interferometer with imaging capability," NDT E Int., vol. 37, no. 7, pp. 545–550, Oct. 2004.

[34] M. Pieraccini, “Real Beam vs. Synthetic aperture radar for slope monitoring,” in Proc. Prog. Electromagn. Res. Symp. (PIERS), Stockholm, Sweden, Aug. 2013, pp. 1627–1630.

H. Klausing, “Feasibility of a synthetic aperture radar with rotating antennas (ROSAR),” in Proc. 9th Eur. Microw. Conf., Sep. 1989, pp. 287–299.

[35] C. L. Liu and P. P. Vaidyanathan, "Super Nested Arrays: Linear Sparse Arrays With Reduced Mutual Coupling—Part I: Fundamentals," in IEEE Transactions on Signal Processing, vol. 64, no. 15, pp. 3997-4012, Aug.1, 1 2016.

[36] C. L. Liu and P. P. Vaidyanathan, "Two-dimensional sparse arrays with hole-free coarray and reduced mutual coupling," 2016 50th Asilomar Conference on Signals, Systems and Computers, Pacific Grove, CA, 2016, pp. 1508-1512.

Acknowledgements

I wish to express my sincere gratitude to my supervisor, Prof. Motoyuki Sato, for his support in my doctoral program in his laboratory. His energy and enthusiasm have always impressed me, as well as his way to manage the laboratory. I greatly appreciate for providing me a help and many chances to participate in field experiments, which I hope to keep as a warm memories in my life.

I also wish to express my gratitude to Prof. Naoki Honma from Iwate University, Prof. Takatoshi Ito and Prof. Qiang Chen from Tohoku Universitry, Japan for serving as my dissertation committee and provided me many constructive suggestions and comments.

I am grateful for my previous and present colleagues and friends at Sato Laboratory of Tohoku University. I thank our previous Assistant Prof. Dr. Kazunori Takahashi who helped me much at the beginning of my study here. I would like to thank our current Assistant Prof. Kazukata Kikuta and Assistant Prof. Lilong Zou who helped me much on revising my manuscripts and dissertation and help in preparing the final defence.
I am grateful to my friends and colleagues, especially Weike Feng, who helped and inspired me on the further improvements of my work, and also sharing a good time, and Iakov Chernyak for support and discussions on the research topic. It is important to be a part of a good community, due to its great influence on yourself, so I am grateful to share such a long time with my laboratory mates and colleagues, former and new, for being so nice to me, thank you guys, Li Yi, Christian N. Koyama, Amila Thilanka Karunathilake, Bo Yang, Satoshi Yamazaki, Shinpei Nakano, Bartolini Lapo, Kazuki Fujisawa, Amarasaikhan Tsogtbaatar, Yanzenhen Wan, Delima Canny Valentine, Suyun Wan, Grigoriy Chernyak, Masafumi Kobayashi, Aderibigbe Afeez, Yasunari Mori, and further more. I also would like to thank Masashi Nakaya, who graduates the same time as me and wish him a good luck.

I need to give a special thanks to our secretary Naoko Nakai who works hard to make our study more conveniently and smoothly and to just being such a good person. The same gratitude I would also like to address to our secretary Masako Kato, who provides me a help and support in laboratory life.

I would like to kindly thank my scientific advisers from my original university, Tomsk State University, Vladimir Yakubov and Evgeny Balzovsky to share their knowledge during my undergraduate and master courses and help me to start my scientific research.

During my study I had a good and hard times and always felt a support from my very close friends, even though they have been far away. Michael Sabelev, Sasha Popov, Cherepov Anton, Evgeniy Krivobok, Gleb Strigunov, Yaroslav Zakiev, Rustam Gallimulin, Aleksandr Nikitin and Grisha Guriev, thank you, guys.

Finally, I would like to express my gratitude and love to my parents and family, Petr Ivanovich Lyulyakin, Vera Grigoryevna Lyulyakina, Olga Petrovna Lyulyakina and Lyubov Ivanovna Kredisheva, my lovely grandmother.

Lyulyakin Andrey

January 2018, Sendai

Publication List

- **Conferences**
  - A. Lyulyakin, M. Sato "75 GHz FMCW radar system for Synthetic Aperture Radar Imaging" Proceedings of the IEICE General Conference, vol.2015, B-1-51, August 2015
  - A. Lyulyakin, I. Chernyak, M. Sato "Antenna design for the sparse array and the array pattern optimization" IEICE Tech. Rep., vol. 116, no. 526, AP2016-196, pp. 103-107, March 2017